Modeling the Non-equilibrium Phenomenon of Diffusion in Closed and Open Systems at an Atomistic Level Using Steepest-Entropy-Ascent Quantum Thermodynamics

Aimen M. Younis

Dissertation submitted to the Faculty of the
Virginia Polytechnic Institute and State University
in partial fulfillment of the requirements for the degree of

Doctor of Philosophy
In
Mechanical Engineering

Michael R. von Spakovsky, Chair
Michael W. Ellis
Clinton L. Dancey
Scott T. Huxtable
Vittorio Verda

June 24, 2015
Blacksburg, Virginia

Keywords: atomistic-level diffusion, non-equilibrium, transient, and steady state diffusivities, non-equilibrium thermodynamics, steepest-entropy-ascent quantum thermodynamics.

Modeling the Non-equilibrium Phenomenon of Diffusion in Closed and Open Systems at an Atomistic Level Using Steepest-Entropy-Ascent Quantum Thermodynamics

Aimen M. Younis

Abstract

Intrinsic quantum Thermodynamics (IQT) is a theory that unifies thermodynamics and quantum mechanics into a single theory. Its mathematical framework, steepest-entropy-ascent quantum thermodynamics (SEAQT), can be used to model and describe the non-equilibrium phenomenon of diffusion based on the principle of steepest-entropy ascent. The research presented in this dissertation demonstrates the capability of this framework to model and describe diffusion at atomistic levels and is used here to develop a non-equilibrium-based model for an isolated system in which He^3 diffuses in He^4. The model developed is able to predict the non-equilibrium and equilibrium characteristics of diffusion as well as capture the differences in behavior of fermions (He^3) and bosons (He^4). The SEAQT framework is also used to develop the transient and steady-state model for an open system in which oxygen diffuses through a tin anode. The two forms of the SEAQT equation of motion are used. The first, which only involves a dissipation term, is applied to the state evolution of the isolated system as its state relaxes from some initial non-equilibrium state to stable equilibrium. The second form, the so-called extended SEAQT equation of motion, is applied to the transient state evolution of an open system undergoing a dissipative process as well mass-interactions with two mass reservoirs. In this case, the state of the system relaxes from some initial transient state to steady state. Model predictions show that the non-equilibrium thermodynamic path that the isolated system takes significantly alters the diffusion data from that of the equilibrium-based models for isolated atomistic-level systems found in literature. Nonetheless, the SEAQT equilibrium predications for He^3 and He^4 capture the same trends as those found in the literature providing a point of validation for the SEAQT framework. As to the SEAQT results for the open system, there is no data in the literature with which to compare since the results presented here are completely original to this work.

In memory of my beloved mother and to my father

To my brothers and sisters

To my wife and children

Acknowledgement

I would like to take this chance to express my deep thanks and appreciation to my advisor Dr. Michael R. von Spakovsky for his guidance, support, patience, and being a mentor for me during my PhD studies. Also, I would like to express my thanks to all my committee members: Dr. Michael W. Ellis, Dr. Clinton L. Dancey, Dr. Scott T. Huxtable, and Dr. Vittorio Verda, as well as to Dr. Eugene Brown for their support, comments, and friendship. Also, I would like to thank all my colleagues: Dr. Charles E. Smith, Dr. Omar Al-Abbasi, Dr. Sergio Cano, Alejandro Fuentes and Guanchen Li. In addition, I would like to express my thanks to both Jamie Archual and Ben Poe and to Cathy Hill for helping me, answering my questions, and providing their friendship.

I would as well like to express my thanks to Omar Al-Mukhtar University, Bayda, Libya for nominating me for a Libyan government scholarship and to the Canadian Bureau for International Education (CBIE) for scholarship management during my studies. Also, I would like to express my thanks and appreciation to the Department of Mechanical Engineering at Virginia Tech for providing me with financial support during the last year of my study.

I would like to express my extreme gratitude and deep feeling of appreciation to my late mother, Hamida, the first person to teach me how to hold a pencil and to write. Without her hope, love, and prayer, I could not have succeeded during my studies and my life. I hope to meet with her in the hereafter in paradise. Also, I would like to express my gratitude and appreciation to my father, Mofteh, and to my brothers: Ali, Tarek, Rafaa, and Arheim and to my sisters: Asma, Nesrin, and Marwa and to all my cousins, friends, and teachers for their hope, love, prayers, and kind words which supported me during my studies.

Finally, I would like to deeply thank my wife, Mona, for her patience, support, and love and for staying with me on this journey, particularly during times of hardship. To my children: Mohamed, Jenan, and Sanad as well go my heartfelt thanks.

Table of Contents

Table of Figures

List of Tables

Chapter 1 - Introduction

1.1 Diffusion at Atomistic Levels

Diffusion is the most fundamental subject in many disciplines in engineering, physics, chemistry, and biology. Scientists and researchers have made great progress toward modeling and developing diffusion as a microscopic (i.e., atomistic-scale) phenomena [1-4]. Diffusion is considered to be a kinetic process that leads to the uniform mixing of different particles (chemical components). Therefore, the basic concepts of kinetic theory are introduced here to describe diffusion at the atomistic-scales [4]. The following sections provide the fundamental concepts needed in order to understand diffusion.

1.1.1 Fick's Law

In 1855, Adolf Fick published his research regarding his study of the behavior of salt-water undergoing diffusion. Fick's law is based on the underlying fundamental assumption that the mass flux can be defined as the amount of mass diffusing perpendicularly through a surface of unit area per unit time. By direct observation, Fick found that the mass flux, $J(x,y,z)$, is proportional to the concentration gradients responsible for mass transport and defined the proportionality constant as the diffusion coefficient. The mass flux is in the opposite direction of the concentration gradient [4-6]. For a mass flux in the x direction, the flux is written as:

$$J_x = -D\frac{\partial c}{\partial x} \tag{1.1}$$

where the symbol D denotes the diffusion coefficient, and c is the concentration. Here and in the following, diffusion is only considered in one direction.

1.1.2 Derivation of Fick's Law at Atomistic Scales

It is a natural phenomenon that a particle goes from high density regions to low density regions. The travel of the particle density is called the mass flux. The principle of distribution forms high to low regions, which means that the mass flux of a particle always decreases most rapidly in the direction of the negative slope of the particle density. The variables considered are the particle density, $n(x,t)$, and the velocity distribution of the particle in the x direction, $v_x(x,t)$ [7-11]. This distribution can be represented mathematically [12] as

$$J_x = -\, n(x,t)\; v_x(x,t) \tag{1.2}$$

The particle density can be obtained by summing the distribution function, $f(x,t)$, over all energy levels (e.g., over all energy eigenlevels if quantum effects are considered), such that

$$n(x,t) = \sum_i f(x,t) \tag{1.3}$$

The mass flux of the particle as a function of the distribution function can then be expressed as

$$J_x = -\sum_i f(x,t)\; v_x(x,t) \tag{1.4}$$

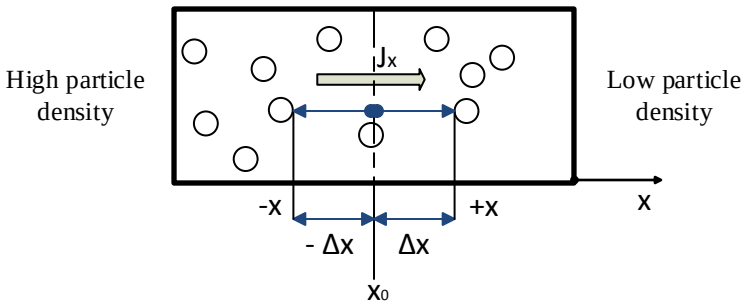

Figure 1.1. One-dimensional particle transport through a gas.

At this stage, diffusion (the mass flux) is assumed to be a process by which particles are transported by means of the random thermal motion that takes place at the microscopic length scale. This length scale requires consideration of the mean free path, for example, in a gas. In other words, diffusion occurs by particles traveling along random paths between collisions. A sequence of random motions can be described by using the concept of the random walk. The random walk considers a particle at location x_0 that takes one step of length Δx to either the left at $-x$ or the right at $+x$. It is assumed that one-half of the particles are transported to the left and the other half to the right [13] as shown in Figure 1.1. The mass flux is then expressed as

$$J_x = \frac{1}{2}\sum_i f(x,t)\; v_x(x,t)\Big|_{-x} - \frac{1}{2}\sum_i f(x,t)\; v_x(x,t)\Big|_{+x} \tag{1.5}$$

Using a first order Taylor expansion series, this can be written as

$$J_x = -\sum_i \tau\, v_x^2 \frac{\partial f_i}{\partial x} \tag{1.6}$$

where τ[1] is the relaxation time that is the average time travelled by the particle between collisions [14]. It is noteworthy that equation (1.6) provides a fundamental basis for defining and modeling the diffusion equation in the non-equilibrium and equilibrium domains and that this equation works only for non-reacting systems.

1.2 Intrinsic Quantum Thermodynamics (IQT)

In 1965, Hatsopoulos and Keenan restated the second law of thermodynamics to be a statement of the existence and uniqueness of stable equilibrium states, which later became known as the Hatsopoulos-Keenan statement of the second law [15]. Based on this statement, entropy plays a fundamental role not only in the equilibrium domain but also in the non-equilibrium domain. In other words, entropy like energy is postulated to be a physical property of matter, like energy, and can be defined for all systems, even a single particle. In 1976, Hatsopoulos and Gyftopoulos introduced the theory of intrinsic quantum thermodynamics (IQT) that unifies quantum mechanics and thermodynamics into a single theory which explains the microscopic foundations of entropy and irreversibility that drive all natural physical phenomena [16-19]. IQT provides a framework in which the evolution of state of a system undergoing a dissipative process can be predicted based on the principle of steepest entropy ascent [20].

Initially and for at least two decades, the unified theory was called quantum thermodynamics (QT) [21]. More recently its name was changed to intrinsic quantum thermodynamics (IQT) by von Spakovsky and Smith [22] since the term quantum thermodynamics (QT) had been coopted by others to refer to more conventional approaches which attempt to explain "dissipative" phenomena at atomistic scales. Moreover, the term steepest-entropy-ascent quantum thermodynamics (SEA-QT) was introduced by Beretta, von Spakovsky, and Cano to distinguish the mathematical framework of IQT from its rather startling theoretical claims in order to emphasize the application aspects of this new paradigm. It is these terms which will be used through this dissertation.

[1] $\tau = \Delta x / v$ where Δx is the mean free path for the average time travelled by the particle between collisions, and v is the velocity distribution of the particle.

1.2.1 Schrödinger Equation of Motion

In 1926, Schrödinger developed an equation that later became known as the Schrödinger wave equation and that describes the time evolution of state of a system that moves from one pure state to another. All possible pure states are represented by vertical axis of energy-entropy diagram given in Figure 1.2.

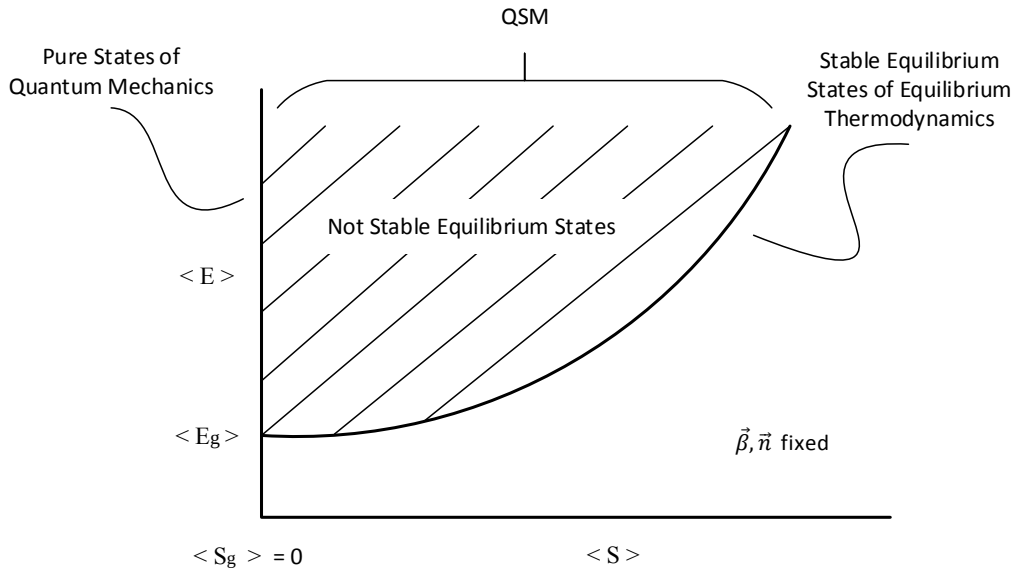

Figure 1.2. Energy versus entropy diagram where $\vec{\beta}$ and $\vec{n}$ are the set of all parameters (e.g., volume, magnetic field strength, etc.) and the set of constituent amounts, respectively, which go to define the system.

The Schrödinger equation of motion [23-30] is given by

$$\hat{H}\,\Psi(\vec{r},t) = i\,\hbar\,\frac{\partial\Psi(\vec{r},t)}{\partial t} \tag{1.7}$$

where $\Psi(\vec{r},t)$ is the wave function or state function for a system (e.g., a single particle) that is a function of time and space, $\hbar$ is the reduced Planck constant[2], and the operator $\hat{H}$ is the Hamiltonian operator that corresponds to the energy of the system and is a linear combination of

[2] $\hbar = h/2\pi$ = 1.05457172x10^{-34} kg m^2/s

kinetic energy and potential energies. The operator $\hat{H}$ for a single particle m in potential field $V(\vec{r})$ is expressed as

$$\hat{H} = -\frac{\hbar^2}{2\,m}\,\nabla^2 + V(\vec{r}) \tag{1.8}$$

When the Hamiltonian operator is independent of time[3], i.e., $\hat{H} = \hat{H}(\vec{r})$, the Schrödinger equation can be separated into time-dependent and time-independent by using the separation-of-variables method. Assuming that the wave function, $\Psi(\vec{r},t)$, can be written in the form

$$\Psi(\vec{r},t) = \phi(t)\,\psi(\vec{r}) \tag{1.9}$$

the time-dependent Schrödinger equation can be written as

$$i\,\hbar\,\frac{\partial\phi(t)}{\partial t} = E\,\phi(t) \tag{1.10}$$

While the time-independent equation is written as

$$\hat{H}\,\psi(\vec{r}) = E\,\psi(\vec{r}) \tag{1.11}$$

where t is time, and $\vec{r}$ represents the spatial coordinates, and E is a constant called energy eigenvalues and represents the energy states of the system. Solving for $\phi(t)$ leads to

$$\phi(t) = A\,e^{\left(\frac{-i\,E\,t}{\hbar}\right)} \tag{1.12}$$

where A is a constant. Furthermore, equation (1.11) can be expanded to yeild

$$-\frac{\hbar^2}{2\,m}\,\nabla^2\psi(\vec{r}) + V(\vec{r})\,\psi(\vec{r}) = E\,\psi(\vec{r}) \tag{1.13}$$

This last equation is also known as the energy eigenvalue problem with the eigenvalues, E, and eigenfunctions[4], $\psi(\vec{r})$.

In 1926, Born came up with the correct explanation[5] of wavefunction by using the square of the absolute value of the wavefunction as the probability density, $P(\vec{r},t)$, for finding a particle in

[3] In other words, the potential energy $V(\vec{r})$ is independent of time.

[4] Each paired E and $\psi(\vec{r})$ is called an eigenstate.

a certain location $\vec{r}$ at time t. If a particle moves along the x-axis and is located in the region $a \leq x \leq b$, the probability of finding the particle between a and b is given by [26, 29]

$$P(x,t) = \int_a^b |\Psi(x,t)|^2 \, dx \tag{1.14}$$

where $P(x,t)$ and $\Psi(x,t)$ are the probability density and the wavefunction[6] along the x-axis, respectively. The properties of a valid wavefunction [29] are as follow:

- single-valued
- continuous
- differentiable
- squared-integrable

It is noteworthy that the eigenfunction has the same properties as those of the wavefunctions and can be considered as the spatial part of the wavefunction [29, 31]. Moreover, the probability density can be expressed in terms of the eigenfunctions.

1.2.2 von Neumann Equation of Motion

Starting with the Schrödinger equation and its adjoint, von Neumann found an equation[7] of motion [12, 32-34] that describes the time evolution of the density matrix[8], $\rho(t)$. This equation can be expressed as

$$\frac{\partial \rho(t)}{\partial t} = -\frac{i}{\hbar}[H, \rho(t)] \tag{1.15}$$

where the brackets denote the commutator[9] and H is the Hamiltonian operator. After finding $\rho(t)$ as a function of time by solving this equation, the expectation value of an observable A can be found as follows:

---

[5] This explanation is known as the Born interpretation of the wavefunction.

[6] $|\Psi|^2 = \Psi\,\Psi^*$ where Ψ^* is the complex conjugate of the wavefunction.

[7] If the sign on the right-hand side is positive, equation (1.15) is called the Heisenberg equation of motion.

[8] The density matrix is a representation of the density operator.

[9] $[H, \rho] = H\rho - \rho H$

$$\langle A \rangle = \mathrm{Tr}(\rho(t)A) \tag{1.16}$$

where the symbol $\mathrm{Tr}(\ldots.)$ stands for the trace of matrix [32-34]. The properties of the density matrix can be summarized as follows:

- The density matrix is hermitian, i.e., $\rho = \rho^*$, where ρ^* is conjugate of the density matrix.
- The trace of any density matrix is equal to one, i.e., $\mathrm{Tr}(\rho) = 1$.
- For a pure state, $\rho^2 = \rho$ and $\mathrm{Tr}(\rho^2) = 1$.
- For a mixed state, $\rho^2 \neq \rho$ and $\mathrm{Tr}(\rho^2) < 1$.
- The eigenvalues, λ_i, of a density matrix satisfy the constraint $0 \leq \lambda_i \leq 1$.

It is noteworthy that the Schrödinger equation describes systems in pure states[10], while the von Neumann equation can describe systems in mixed states[11]. Moreover, equation (1.15) is called a reversible equation of motion that can be applied to the evolution of both pure and mixed states. It is the Schrödinger equation in matrix form for pure states [35] and is, thus, the counterpart of the reversible time-dependent part of the Schrödinger equation of motion.

The density operator, ρ, for pure states using in the von Neumann equation is that defined by quantum mechanics (QM), while the density operator for mixed states is that defined by quantum statistical mechanics (QSM) and is based on a statistical mix of an ensemble of pure state density operators [36]. QSM and the von Neumann equation of motion are, thus, used as a bridge to connect the world of zero-entropy states (pure states; the vertical axis of Figure 1.2) with that of non-zero-entropy states (mixed states; the region of not stable and stable equilibrium states of Figure 1.2) in a way analogous to how QSM and the maximum entropy principle of thermodynamics bridge the world of QM and equilibrium thermodynamics (ET) [37]. The difference is that with the latter one arrives at a full description of stable equilibrium (see the curve of stable equilibrium states in Figure 1.2) while in the former the description is very much incomplete since the von Neumann equation is unable to predict the irreversible relaxations of state which occur in the hatched area of Figure 1.2.

[10] Pure states are zero-entropy states.

[11] Mixed states are non-zero-entropy states.

1.2.3 Equation of Motion of Intrinsic Quantum Thermodynamics

Because the second law of thermodynamics is absent, the Schrödinger equation of motion, equation (1.7), is only able to predict a certain class of reversible state evolutions in the zero-entropy domain. This is also true for the von Neumann equation of motion, equation (1.15). In 1981, this lacuna was addressed when Beretta proposed an equation of motion for the theory of intrinsic quantum thermodynamics (IQT) introduced by Hatsopoulos and Gyftopoulos [16-19]. This equation is based on the principle of steepest entropy ascent (SEA) and is able to describe irreversible phenomena [20]. The resulting mathematical framework of SEAQT can be used to predict the evolution of state of a system undergoing a dissipative process using the following equation of motion [38-41]:

$$\frac{\partial \rho(t)}{\partial t} = -\frac{i}{\hbar}[H, \rho(t)] - \frac{1}{\tau_D}\mathcal{D} \tag{1.17}$$

where τ_D is a scalar time constant or functional and $\mathcal{D}$ is the dissipation operator. Details of this dissipation operator are given in subsequent chapters. It is noteworthy that when the dissipation operator $\mathcal{D}$ is zero (a pure state ($\rho^2 = \rho$)), equation (1.17) reduces to equation (1.15) and is, thus, able to predict the relaxation of state for an isolated system undergoing both reversible and irreversible processes.

1.3 Motivation to use the SEAQT Framework

The mathematical formalisms of the theories of QM and ET have been applied successfully by scientists and researchers to a wide variety of topics in science and engineering with good agreement with experimental results. ET uses a phenomenological description of system and system state evolution, while QM and QSM are based on a fundamental description, which tracks the behavior of the atoms, molecules, or particles that make up a system [42]. As a consequence, these theories arrive at different conclusions as to the nature of entropy and the second law of thermodynamics (e.g., see [37, 43, 44]). ET views entropy as a real, physical property of matter and the second law as fundamental while QM and QSM see entropy as illusion and the second law emerging from QM [43]. Furthermore, ET concerns itself with states of maximum entropy in stable equilibrium while QM deals only with states of zero entropy, namely pure states. To bridge the gap between the phenomenological, maximum-entropy world

of ET and the fundamental, zero-entropy one of QM, a number of theories have been developed to link them such as QSM, quantum information theory, QT, and IQT [16-19].

QSM [45] provides a theoretical framework that links the fundamental description of the quantum properties of atoms, molecules, or particles with the phenomenological description of the thermodynamic state of matter, particularly at equilibrium. The density or so-called state 'state' matrix or operator of QSM contains all the information of system state. In QSM, the state operator, ρ^{QSM}, of system state is based on an ambiguously prepared or heterogeneous ensemble of identical systems [19, 46] each in a different pure state $\rho_i^{QSM} = |\psi_i\rangle\langle\psi_i|$. It is expressed as the statistical average of these pure state operators such that

$$\rho^{QSM} = \sum_i w_i \rho_i^{QSM} \tag{1.18}$$

where

$$\rho^{QSM} \neq \rho_1^{QSM} \neq \rho_2^{QSM} \neq \ldots \neq \rho_N^{QSM} = \cdots \tag{1.19}$$

and the w_i are the equal a prior statistical weights which satisfy the normalization condition $\sum_i w_i = 1$. However, the state operator, ρ^{QSM}, obtained from an ambiguously prepared ensemble is inconsistent with the second law of thermodynamics since it leads to a perpetual motion machine of the second kind (PMM2) [19, 44]. In other words, if the state of the ensemble ρ^{QSM} is that of stable equilibrium its adiabatic availability is necessarily zero. However, the state of each member of the ambiguously prepared ensemble has an adiabatic availability greater than zero since it is not at stable equilibrium. This implies that energy could be extracted from each member of the ensemble but not from the ensemble as a whole which, of course, is a contradiction. Moreover, as is conclusively demonstrated by Park [47], ρ^{QSM} only represents the state of the ensemble and not the state of the system for which it is a presentation. Thus, a bedrock of physical thought is lost [44, 47]. In addition, the von Neumann equation of motion is unable to capture the evolution in time of a system initially in a state of non-equilibrium relaxing towards stable equilibrium.

In order to overcome these fundamental weakness, IQT uses an unambiguously prepared or homogeneous ensemble as the basis of its density or state operator, ρ [47, 48]. As a result, the state of the ensemble is equal to that of each member of the ensemble so

$$\rho = \rho_1 = \rho_2 = \cdots = \rho_N = \cdots \tag{1.20}$$

Thus, the concept of state of the system is recovered since the state of the ensemble coincides with that of the system. Furthermore, it consistent with the second law and avoids a PPM2. It is able to describe any state of zero or nonzero entropy. Finally, the nonlinear IQT equation of motion based on an unambiguous ensemble is able to capture not only the reversible process of QM but also the irreversible process of thermodynamics which results in a relaxation of state from that of non-equilibrium to that of stable equilibrium [38, 39, 49].

1.4 Objectives and Original Contributions

There are two overall objectives of this doctoral research. The first is to use the SEAQT framework of IQT to model the non-equilibrium behavior of a closed atomistic-level gaseous system as its non-equilibrium state evolves in time towards stable equilibrium providing a description of the diffusive non-equilibrium behavior of fermions and bosons and comparing this description with the conventional equilibrium one based on statistical thermodynamics [50-56] for diffusion found in literature. The second is to apply the SEA-QT framework to an open atomistic-level system as its state evolves from a transient one to one of steady state, providing a description of the diffusive behavior of the system. In this research, the isolated, closed system considered is that of helium-3 and helium-4 while the open system involves oxygen diffusion through a tin anode. It should be noted that both systems are non-reacting.

In order to achieve these goals, the following set of tasks was undertaken:

- Consider a closed two-particle isolated system of non-interacting He^3 (fermion) and He^4 (boson) and establish the energy eigenstructure for this system by analytically solving the eigenvalue problems for both fermions and bosons to get the energy eigenvalues and eigenfunctions for He^3 and He^4.
- Implement the SEAQT equation of motion for an isolated, closed system to predict the evolution of state of this system from an initial state far from equilibrium to one at stable equilibrium.
- Using the SEAQT framework, derive the particle density distribution for non-equilibrium behavior to provide a description for the non-equilibrium-based diffusive behavior of fermions and bosons, which can be applied to the He^3-He^4 system considered here.

- Implement this non-equilibrium-based diffusive description.
- Derive the conventional equilibrium-based diffusive description found in the literature [50-56]
- Validate the equilibrium portion of the results obtained from the SEAQT model with those obtained from the equilibrium-based description.
- Derive and implement the SEAQT non-equilibrium based description for diffusivities for fermions and bosons to predict the non-equilibrium and equilibrium behavior of the diffusivities for He^3 and He^4.
- Compare the equilibrium portion of the SEAQT diffusivity results with the equilibrium-based found in [51-56]
- Geometrically define the open system for oxygen diffusion through a tin anode, and establish the appropriate energy eigenstructure for this 3D atomistic-level system by analytically solving rotational and vibrational energy eigenvalue problems and by using a finite element approach to solve the translational energy eigenvalue problem with periodic boundary conditions for an open system at steady and unsteady state.
- Mathematically derive the appropriate non-equilibrium-based diffusive flux and diffusivity equations for an open system.
- Implement this description and validate it to extent possible.
- Study and implement the extended SEAQT equation of motion (EOM) for mass interactions found in Smith [57] to understand its transient behavior and how to establish a set of steady states.
- Apply the SEAQT EOM to the transient state evolution of the 3D atomistic-level, oxygen- tin-anode system.
- Using the SEAQT framework, predict the non-equilibrium-based diffusive fluxes and diffusivities in the axial direction through the oxygen-tin-anode system both for the transient and steady state cases.

An original contribution to the literature of the research in this dissertation is the use of the mathematical framework of SEAQT to develop a non-equilibrium-based model for atomistic-level He^3 and He^4 and the implementation of this model to capture the non-equilibrium effects on predicted diffusivities. Another original contribution is the use of the mathematical framework of

SEAQT to develop a non-equilibrium-based model of oxygen diffusion through a tin anode at atomistic scales with the purpose of describing the transient thermodynamic path that the system takes in reaching steady state. Moreover, the extended SEAQT equation of motion which accounts for mass interactions is used for the first time to model a realistic, open, atomistic-level system in contact with two mass reservoirs. Finally, also original to this work is the derivation and predication of the transient and steady state diffusive fluxes and diffusivities of oxygen diffusion at atomistic-levels.

Chapter 2 - Literature Review

2.1 Applications of the SEAQT Framework

2.1.1 Modeling Hydrogen Storage on Carbon Nanotube

The SEAQT framework is used to model the non-equilibrium process of hydrogen storage in and on a carbon nanotube [57-59]. The system considered here is an isolated 3D tank with a volume of 250 nm^3 containing four hydrogen molecules and a carbon nanotube of 900 carbon atoms with a radius of 1.017 Å and a length of 3.56 Å located at the center of the tank. The eigenstructure of the system is established by solving the translational energy eigenvalue problem and then combining this solution with that of the rotational eigenvalue problem. Interactions between $H_2 - H_2$ and $H_2 - C$ pairs are taken into account by using the Lennard-Jones potential. The SEAQT equation of motion is then solved for different initial states to obtain the non-equilibrium thermodynamic paths and density operators of system state evolution. For a given initial state, Figure 2.1a shows the 3D spatial distribution of the probability distribution function of the initial non-equilibrium state at the non-dimensional time t^*=-2.0, while Figure 2.1b gives it at an intermediate non-equilibrium state at t^*=-0.224. The evolution in state then continues with Figure 2.2a showing the probability desnity distribution functions of the intermediate non-equilibrium state at t^*=-0.484 following in Figure 2.2b by that of final state in stable equilibrium at t^*=1.198. Clearly, as can be seen in this evolution of state, the highest values of the probability distribution function and, thus, hydrogen densities (the dark red) increasingly occur in the tube and close to the outer walls of the carbon nanotube [57] as the state of the system evolves along its non-equilibrium path to a final state in stable equilibrium.

2.1.2 Comparison IQT Results with Experiment

Results are obtained from simulations of the SEAQT equation of motion applied to a closed system experiencing heat interaction with a reservoir as described in [22, 57]. These results are then compared with the experimental results found in Literature.

The thermodynamic system considered here is a Paul trap containing a single trapped Be^+ ion which is put into different quantum states. The SEAQT equation of motion used to model this system is given by

$$\frac{d\rho(t)}{dt} = -\frac{i}{\hbar}\,[H,\rho(t)] + \frac{1}{\tau_D}\{\Delta M,\rho\} + \frac{1}{\tau_G}\{\Delta G,\rho\} \tag{2.1}$$

where the first term to the right of the equals is the Schrödinger term which for this application is dropped since the density operator ρ and the Hamiltonian H commute. The second term represents the dissipation operator, while the third term is the so-called heat-interaction operator. The time relaxation constants used are $\tau_D = 20.0$ and $\tau_G = 25.0$. The operators M and G are defined as non-equilibrium Massieu operators and are given by

$$M = S - \frac{H}{\theta_H} \tag{2.2}$$

$$G = S - \frac{H}{\theta_Q} \tag{2.3}$$

where θ_H and θ_Q are the non-equilibrium temperatures associated with the Hamiltonian and the heat interaction, respectively, S is the entropy operator given by

$$S = -k_b\ \ln(\rho) \tag{2.4}$$

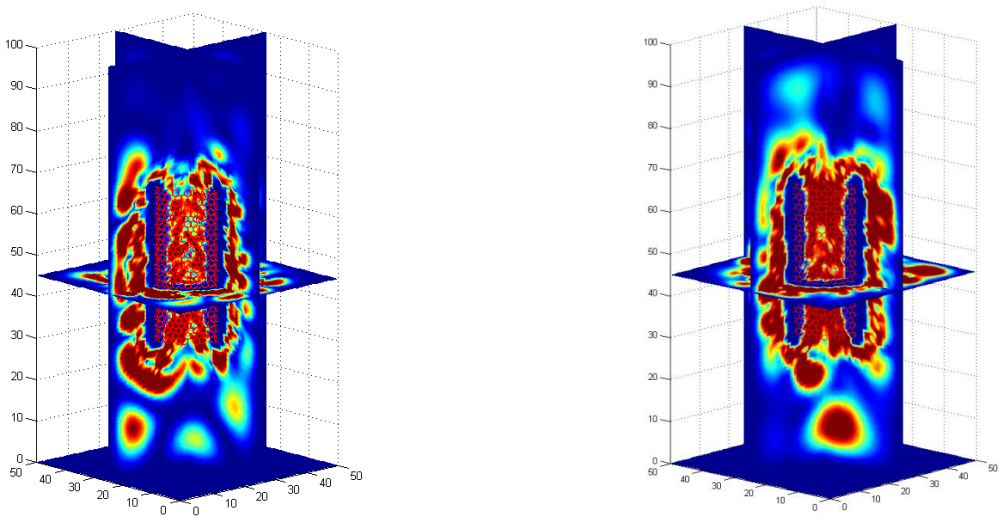

(a) (b)

Figure 2.1. Probability distribution function of particle density as a function of position for (a) the initial non-equilibrium state at t*=-2.0 and (b) the intermediate non-equilibrium state at t*=-2.0 [57].

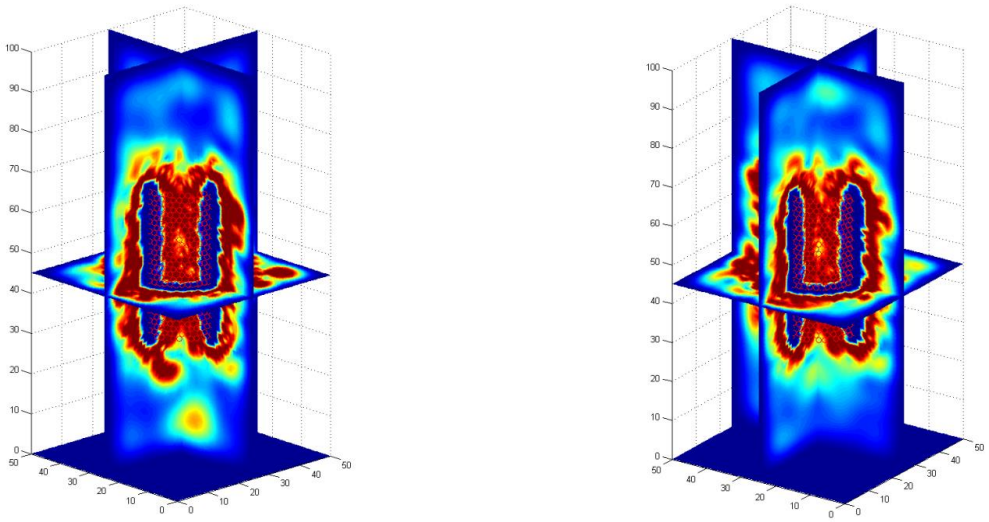

(a) (b)

Figure 2.2. Probability distribution function of particle density as a function of position for (a) the intermediate non-equilibrium state at t^*=0.849 and (b) the final sate of stable equilibrium at t^*=1. 0 [57].

The symbol Δ in equation (2.1) represents the deviation of an operator from its mean value so that ΔM and ΔG are written as

$$\Delta M = M - < M > I \tag{2.5}$$

$$\Delta G = G - < G > I \tag{2.6}$$

where I is the identity operator. The SEAQT results are presented on the energy-entropy diagram of Figure 2.3 and compared to the experimental data at the lowest 5 energy eigenlevels of the cation. An evolution of state using the SEAQT framework for 100 energy eigenlevels is also given since considering only eigenlevels results in a state evolution which is physically impossible, i.e., violates the second law of thermodynamics. The magenta curve for 5 eigenlevels as that for 100 energy eigenlevels (the red curve) represents the SEAQT results, while the dark blue line connects the experimental results. The light blue line connecting the light blue circles represents the predictions made using the theory of quantum open system (TQOS). For a discussion of this theory and its limitations, the reader is referred to von Spakovsky and Gemmer [43]. As can be seen from the figure, the SEAQT results show good agreement with the experimental data [22, 43, 57].

The experimental data is also compared in Figure 2.4 with the theoretical probabilities obtained from the SEAQT equation of motion with heat interaction, equation (2.1). The symbols stand for the experimental data while the solid lines indicate the theoretical probabilities. As is seen in this figure, the SEAQT predictions compare well with the experimental data. Unlike in the theory of quantum open systems which views the dissipations incurred during the relaxation of state as a loss of information between the system and some ubiquitous environment, the SEAQT framework views the dissipation as a loss in the quality of the energy internal to the system, i.e., it views it as intrinsic to the system itself.

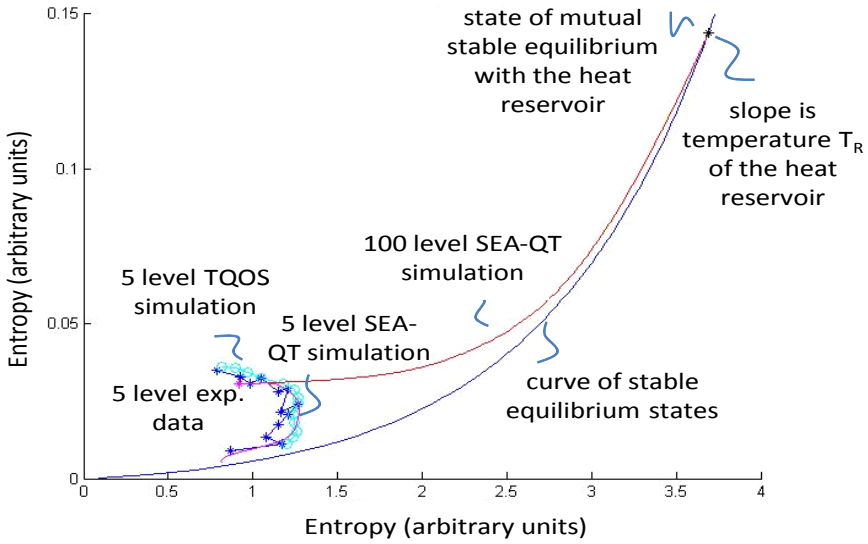

Figure 2.3. The non-equilibrium evolution in thermodynamic state on energy-entropy diagram for the lowest 5 energy levels and for 100 energy levels [22, 57].

2.1.3 Modeling a Composite Atom-Field System

The SEAQT equation of motion is used to model and study the dynamics of the state of a composite system consisting of an atom and an electromagnetic field mode as described in [60-62]. The experimental set up for the cavity quantum electrodynamic (CQED) experimental results of [63] to which the SEAQT prediction are compared is depicted in Figure 2.6.

The atom-field system considered loses coherence between its constitutes when it relaxes to stable equilibrium. In order to predict this loss of coherence, it is assumed that the system is

isolated and that the time evolution of its state is Hamiltonian as well as non-Hamiltonian. The SEAQT equation of motion used here to model the composite system [60, 61] is given by

$$\frac{d\rho(t)}{dt} = -\frac{i}{\hbar}\,[H,\rho(t)] + \left(\frac{1}{\tau_A} D_A \otimes \rho_F + \frac{1}{\tau_F}\rho_A \otimes D_F\right) \tag{2.7}$$

where the first term to the right of the equals defines the unitary Hamiltonian dynamics of the system and the second term its dissipative nonlinear dynamics. In this equation, $\rho_A = \mathrm{Tr}_F(\rho)$ and $\rho_F = \mathrm{Tr}_A(\rho)$ are the reduced state operators, while τ_A and τ_F are time functional or constants.

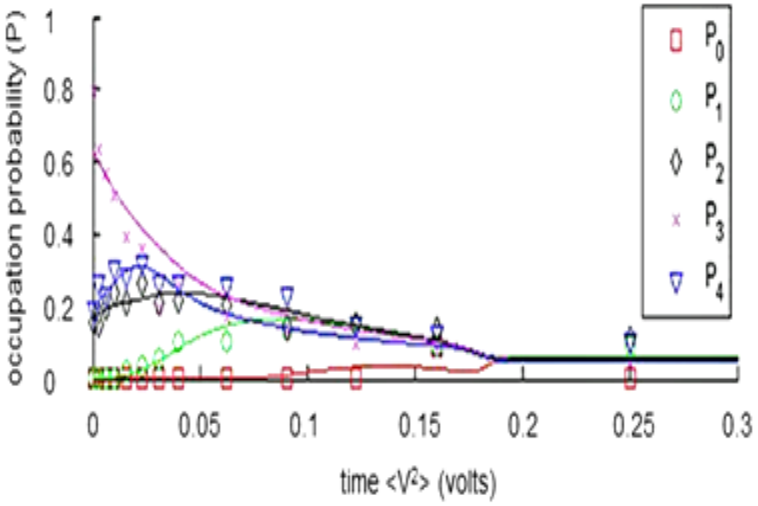

Figure 2.4. Comparison of the experimental decay of cat (i.e., excited) state $|3\rangle$ with the theoretical predictions obtained from the SEAQT equation of state for the lowest 5 energy eigenlevels [22, 43, 57].

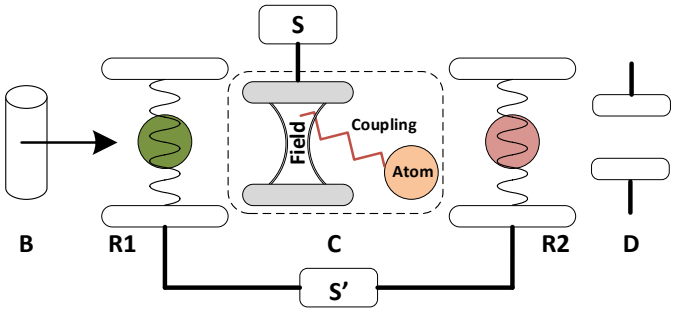

Figure 2.5. Schematic representation of the atom-field CQED experiment [60-62].

The measure of system coherence and correlation used by the SEAQT framework is the trace norm of the commutator operator expressed as

$$\|C\| = Tr(CC^{+}) \tag{2.8}$$

where the commutation operator is defined as

$$C = H\rho - \rho H \tag{2.9}$$

The results obtained from the SEAQT model are compared with the experimental data in Figure 2.6. As can be seen, the SEAQT framework does a very good job of predicting the experiment data. Predictions are also made by using the correlation functions of conventional quantum theory. However, even though it does a good job of predicting the decoherence data at the beginning of the state relaxation, it begins to deviate towards the middle of the relaxation and fails to adequately predict the experimental data towards the end of the relaxation. in fact, it produces a result which is not physical, i.e., it generates coherence [60].

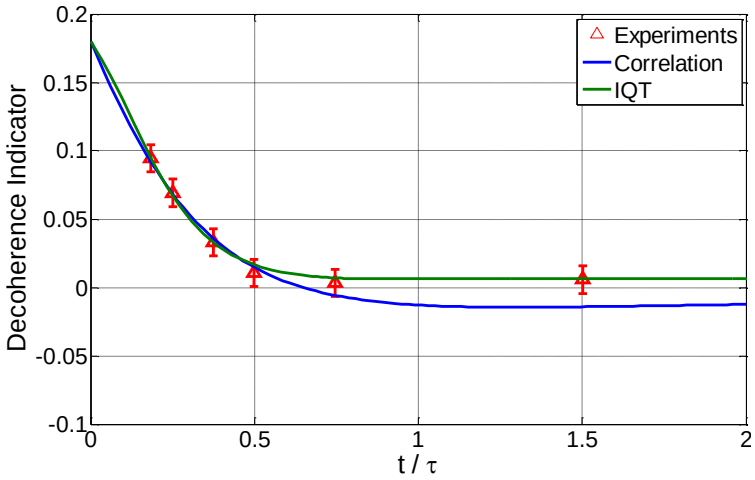

Figure 2.6. Comparison of the experimental data of [63] with the prediction obtained from the SEAQT framework and the correlation function of conventional quantum theory [60-62].

2.1.4 Modeling a Composite Two Interacting Spin-½ Particles

The SEAQT equation of motion is used to model the decoherence phenomenon between two distinguishable and indivisible elementary constituents of type spin-1/2 [62, 64]. The composite

system considered here is shown in Figure 2.7 and consists of these two spin-1/2 particles which interact. The system is modeled using the SEAQT framework to study entangled or coherent states.

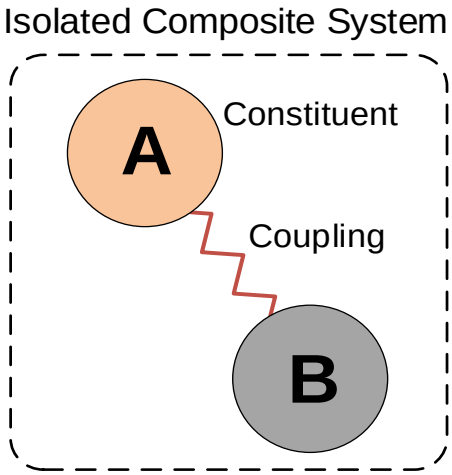

Figure 2.7. Schematic representation of a composite system in which the constituents interact with each other [64].

The SEAQT equation of motion used to model this system is written as

$$\frac{d\rho(t)}{dt} = -\frac{i}{\hbar}\,[H,\rho(t)] + \left(\frac{1}{\tau_A} D_A \otimes \rho_B + \frac{1}{\tau_B}\rho_A \otimes D_B\right) \tag{2.10}$$

where the subscripts "A" and "B" refer to the two constituents and the first term to the right of the equals represents the unitary Hamiltonian dynamics of the system and the second term defines the non-Hamiltonian dissipation dynamics. τ_A and τ_B are the internal-relaxation times for constituents A and B, respectively and are set arbitrarily equal to one. Since the focus here is the kinetics of the state evolution and not its dynamics. To include the latter would require comparison with experiment as is done, for example, in Cano, Beretta, and von Spakovsky [62] or the development of a physical theory to predict τ. The latter is an active area of research. Thus, the results produced here are in terms of dimensionless time.

Both the trace norm of the commutation operator (equation (2.10)) and the rate of the entropy correlation function given by

$$\frac{d\sigma_{AB}(\rho)}{dt} = \dot{\sigma_{AB}}|_H - \dot{\sigma_{AB}}|_D \tag{2.11}$$

where

$$\sigma_{AB}(\rho) = \mathrm{Tr}(\rho\, ln\rho) - \mathrm{Tr}_A(\rho_A \ln\rho_A) - \mathrm{Tr}_B(\rho_B \ln\rho_B) \tag{2.12}$$

are used to study the process of decoherence and decorrelation of system state for a set of 5000 randomly generated initial states. The reason for this large random set of states is to heuristically prove the assertion that the dissipation operator of the SEAQT equation for motion only destroys correlations. As can be seen in Figure 2.8, this assertion appears to indeed be true, which, thus, provides a heuristic proof and confirmation of what the general behavior of the dissipation operator is and should be. Figure 2.9 shows the decoherence which takes places.

2.1.5 Modeling Chemically Reactive System

The SEAQT framework for chemically reaction systems developed by Beretta and von Spakovsky [65] is applied by Al-Abbasi [66] and Al-Abbassi, Beretta, and von Spakovsky [67] at a nanoscale system with a single active reaction mechanism of fluorine reacting with hydrogen, i.e.,

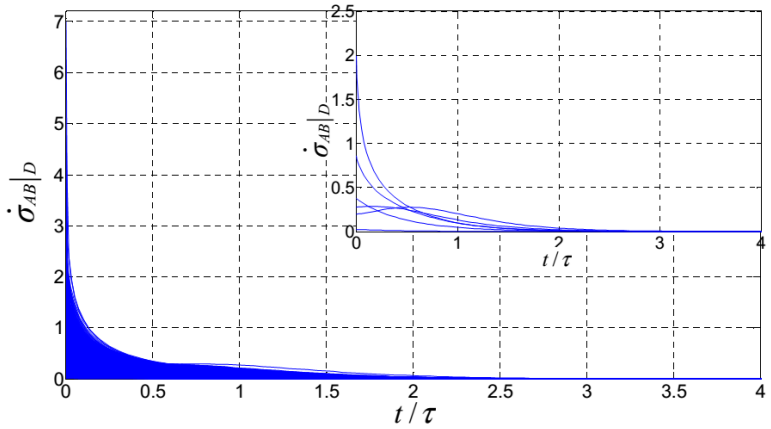

Figure 2.8. Rate of change of the contribution of the dissipative term to the rate of change of the entropy correlation functional for the different 5,000 random initial non-equilibrium states tested. In the inset, the evolution of six particular initial non-equilibrium states (i.e., with degrees of purity of 0.59, 0.58, 0.43, 0.68, 0.86, and 0.28) is depicted in order to show a more detailed evolution of $\dot{\sigma}_{AB}|_D$.

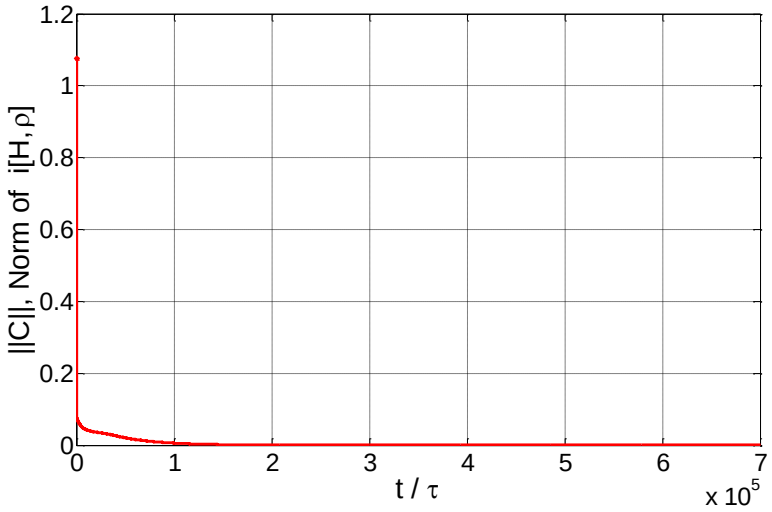

Figure 2.9. Evolution of the norm ||C|| of the commutator term.

$$F + H_2 \rightleftharpoons FH + H \tag{2.13}$$

In order to model this system, both the system-level energy and particle number eigenvalue problems are solved to establish the energy and particle eigenstructure of the system. the SEAQT equation of motion is then solved to obtain the unique non-equilibrium thermodynamic path that describes the relaxation of the state of the system towards stable equilibriu. The vibrational, rotational, and translational energy eigenvalues as well as conservation of system energy and the number of atoms of each species are taken into account during the modeling [66, 67]. All other expectation values such as those of the entropy, entropy generation rate, particle number of each species, the reaction coordinates, etc., are determined at every instant of time by this model. The SEAQT equation of motion considered here is given by

$$\frac{\partial \rho(t)}{\partial t} = -\frac{i}{\hbar}\,[H,\rho] - \frac{1}{2\,k_b \tau}\,\{\Delta M,\rho\} \tag{2.14}$$

where k_b is Boltzmann's constant and the first term to the right of the equals governs the linear Hamiltonian dynamics of the state evolution and the second term the nonlinear, non-Hamiltonian, steepest-entropy-ascent dynamics. This dissipation operator is defined in terms of the deviation operator $\Delta M = M - < M > I$ of the non-equilibrium Massieu operator

$$M = S - \frac{H}{\theta_H} \tag{2.15}$$

where S and H are the entropy and Hamiltonian operators, respectively and θ_H is a non-equilibrium temperature. The entropy operator is given by

$$S = -k_b \ln(\rho + P_0) = -k_b B \ln \rho \tag{2.16}$$

where B and P_0 are the projection operators onto the kernel and range of ρ, respectively [66, 67].

Figures 2.10 and 2.11 show the evolution of the expectation value of the entropy and entropy generation rate for the isolated chemically reactive system when the system relaxes from an initial non-equilibrium state to stable equilibrium. It is seen that the entropy of the system increases very rapidly in the early stage of the evolution and then slows its increase as the system state approaches stable equilibrium. In addition, the peak in the entropy generation rate occurs early in the process and then decreases as the system approaches stable equilibrium.

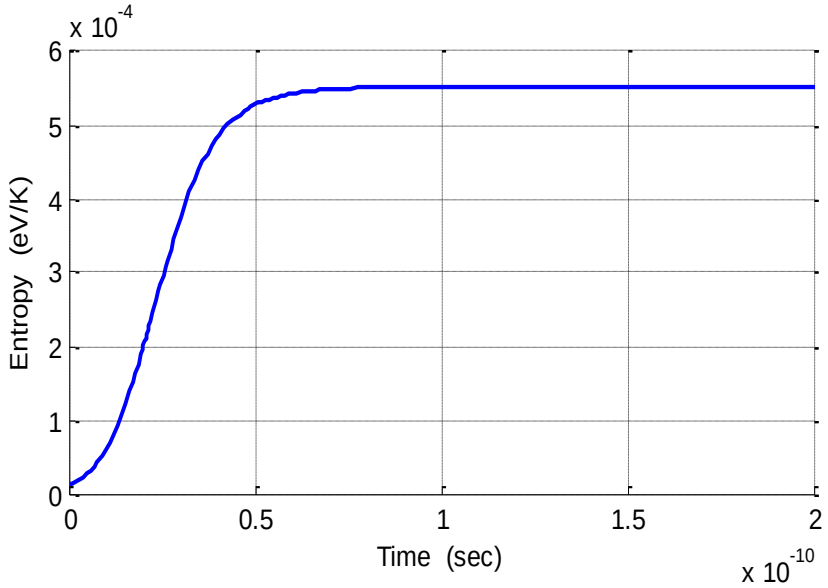

Figure 2.10. Evolution of the expectation value of the entropy for the $F+H_2$ reaction which is at an initial stable equilibrium temperature of 300 K [66, 67].

Figure 2.12 shows the time evolution of the expectation value of the particle number operator for each species. As can be observed, the concentrations of the reactants decrease in

direct proportional to the increase in concentrations of the products [66, 67]. The strength of the SEAQT approach is that it is able to predict the entire kinetic path that the system takes as is seen by the predictions for the net forward, and backward reaction rates given in Figure 2.13.

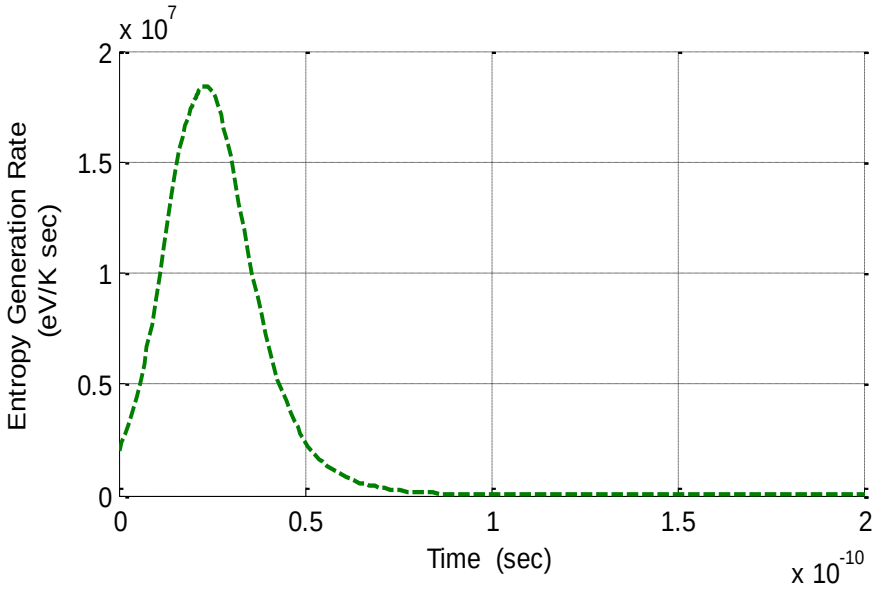

Figure 2.11. The evolution of the expectation value of the entropy generation rate [66, 67].

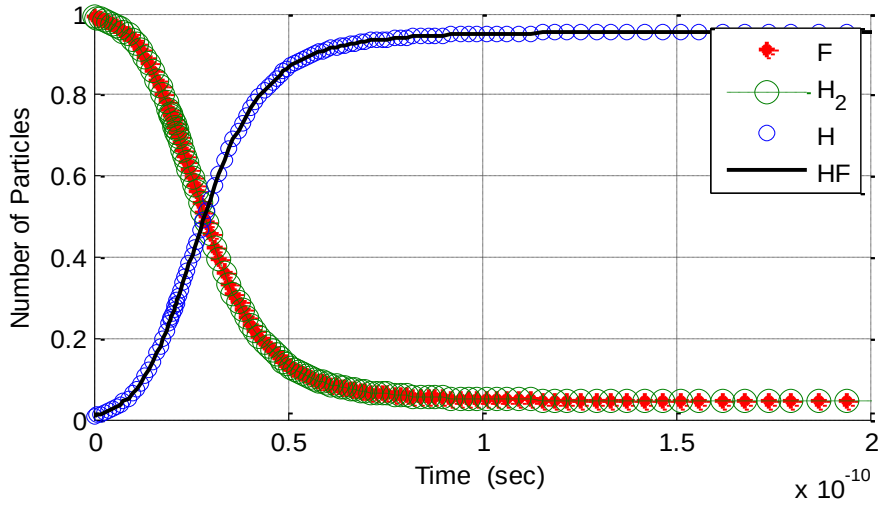

Figure 2.12. Evolution of the expectation value of the particle number operator for each species for the F+H2 reaction which is at an initial stable equilibrium temperature of 300K [66, 67].

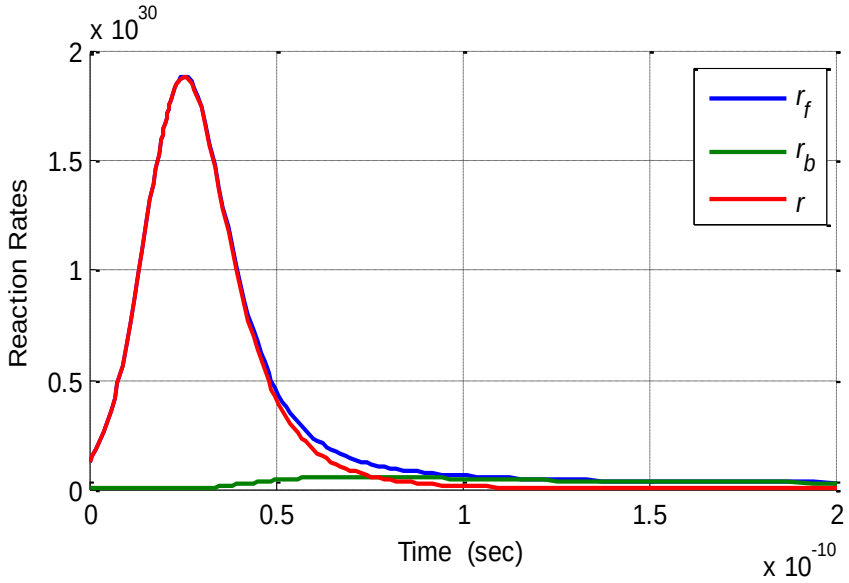

Figure 2.13. The forward, backward, and net reaction rates as a function of time for the $F+H_2$ reaction corresponding to an initial stable equilibrium temperature of 300K [66, 67].

2.2 Quantum Effects on Gas Diffusion at an Atomistic Level

2.2.1 Quantum Size and Quantum Degeneracy Effects

At the nanoscale, classical results are different from those of quantum mechanics because the latter accounts for the wave character of matter while the former only accounts for its particle character. For particles confined in a domain, the probability density is uniform based on the classical viewpoint but is inhomogeneous even at stable equilibrium based on the quantum viewpoints Thus, it is important to study and advance in knowledge of fundamental quantities such as the density distribution and the diffusion of particles at the nanoscale [52-56, 62, 68].

The diffusion coefficient for a monatomic Fermion gas (He^3) and Boson gas (He^4) confined in a rectangular domain are derived analytically in [55]. A mixture of ideal monatomic gases with different concentrations of He^3 and He^4 in a large container connected by a rectangular nano-channel is considered. The nano-channel is assumed to be much larger in direction of diffusion than the thermal de Broglie wave length and the mean free path of the gas particles [55]. The temperature and pressure inside the channel are assumed to be constant, thus, the driving force of the diffusion is only the concentration gradient. In other words, the density gradient plays a role in the diffusion processes, not the temperature or pressure. The derivation is

based on the grand canonical distribution function in order to capture the Boson and Fermion behavior of an ideal gas. In addition, the effective quantum potential is used to replace the quantum probability density by the classical probability density, and the Poisson summation formula is used to calculate the infinite sums which cannot be replaced by integrals at the nanoscale. The diffusive particle flux is given by

$$J_x = -\left(\frac{4}{3}\frac{l_g n\, k_b T}{\sqrt{2\pi\, m\, k_b T}}\right)\left(\frac{L_{i_1}}{L_{i_{1/2}}}\right)\left(\frac{1-\frac{3\sqrt{\pi}}{8}(\alpha_2+\alpha_3)\frac{L_{i_{1/2}}}{L_{i_1}}}{1-\frac{1}{\sqrt{\pi}}(\alpha_2+\alpha_3)\frac{L_{i_0}}{L_{i_{1/2}}}}\right)\frac{\partial c}{\partial x} \tag{2.17}$$

where L_i is the Polylogarithm function of an exponential argument $\pm\exp(\mu_q/k_bT)$, and $\mu_q = \mu - Q$ and μ is the chemical potential. The positive and negative signs stand for Bosons and Fermions, respectively. Q is the effective quantum potential [56] and c is the concentration given by $c = n_s/n$. n_s and n are the species and total density distributions of particles, respectively. α_2 and α_2 are the dimensionless lengths defined as $\alpha_2 = L_c/L_2$ and $\alpha_3 = L_c/L_3$ where L_c is the one half of the most probable de Broglie wavelength of the particle given by $L_c = h/\sqrt{8\, m\, k_b T}$. Here, l_g, m, k_b, and T are the geometry mean free path, mass, Boltzmann's constant, and temperature, respectively. Clearly, the terms in parentheses multiplying the gradient of the concentration c are the diffusion coefficient, which is normalized by dividing through by $(4l_g n\, k_b T)/(\sqrt{2\pi\, m\, k_b T})$ such that

$$D_n = \left(\frac{1}{\sqrt{m}}\right)\left(\frac{L_{i_1}}{L_{i_{1/2}}}\right)\left(\frac{1-\frac{3\sqrt{\pi}}{8}(\alpha_2+\alpha_3)\frac{L_{i_{1/2}}}{L_{i_1}}}{1-\frac{1}{\sqrt{\pi}}(\alpha_2+\alpha_3)\frac{L_{i_0}}{L_{i_{1/2}}}}\right) \tag{2.18}$$

Here D_n is the normalized diffusion coefficient and the terms in the second set of parentheses represent the quantum degeneracy (QD) effect, while those in the third set of parentheses represents quantum size effect (QSE). The dimensionless ratio of the diffusion coefficient $\widehat{D}$ of He^3 to He^4 is defined as

$$\widehat{D} = \frac{D_{He^3}}{D_{He^4}} = \sqrt{\frac{m_{He^4}}{m_{He^3}}}\,\frac{QD_{He^3}}{QD_{He^4}}\,\frac{QSE_{He^3}}{QSE_{He^4}} \tag{2.19}$$

The last equation can be rewritten as

$$\hat{D} = \frac{D_{He^3}}{D_{He^4}} = \hat{D}_{cl}\,\hat{D}_{QD}\,\hat{D}_{QSE} \tag{2.20}$$

where $\hat{D}_{cl} = \sqrt{m_{He^4}/m_{He^3}}$, $\hat{D}_{QD} = QD_{He^3}/QD_{He^4}$, and $\hat{D}_{QSE} = QSE_{He^3}/QSE_{He^4}$. Thus, $\hat{D}_{cl}$, $\hat{D}_{QD}$, and $\hat{D}_{QSE}$ represent the influence of mass, degeneracy, and size effects on diffusion, respectively [55]. $\hat{D}_{QD}$, and $\hat{D}_{QSE}$ are plotted in Figures 2.14 and 2.15 as a function of concentration of He^3 for different n. As can be seen, at high density ($n = 2$), the influence of quantum size effect on the diffusion coefficient ratio is much greater than that at low density ($n = 0.1$). The diffusion coefficient ratio goes to unity as the concentration of He^3 increases. Also, it is seen that the influence of the quantum degeneracy effect on the diffusion coefficient ratio is weak at low density ($n = 0.1$). It seems that the diffusion coefficient of He^3 increases more than that of He^4 with increasing concentration of He^3. On the other hand, the quantum degeneracy effect leads to a decrease in the diffusion coefficient of He^3 with increasing concentration of He^3 at high density ($n = 2$) [55].

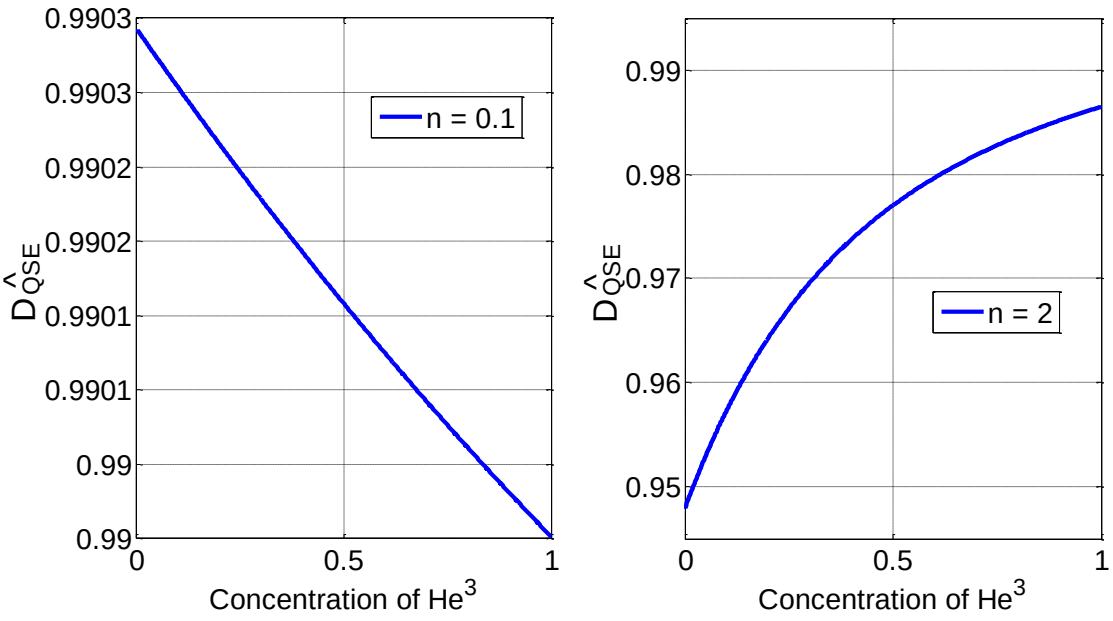

Figure 2.14. Variation of the diffusion coefficient with concentration showing the quantum size effect [55].

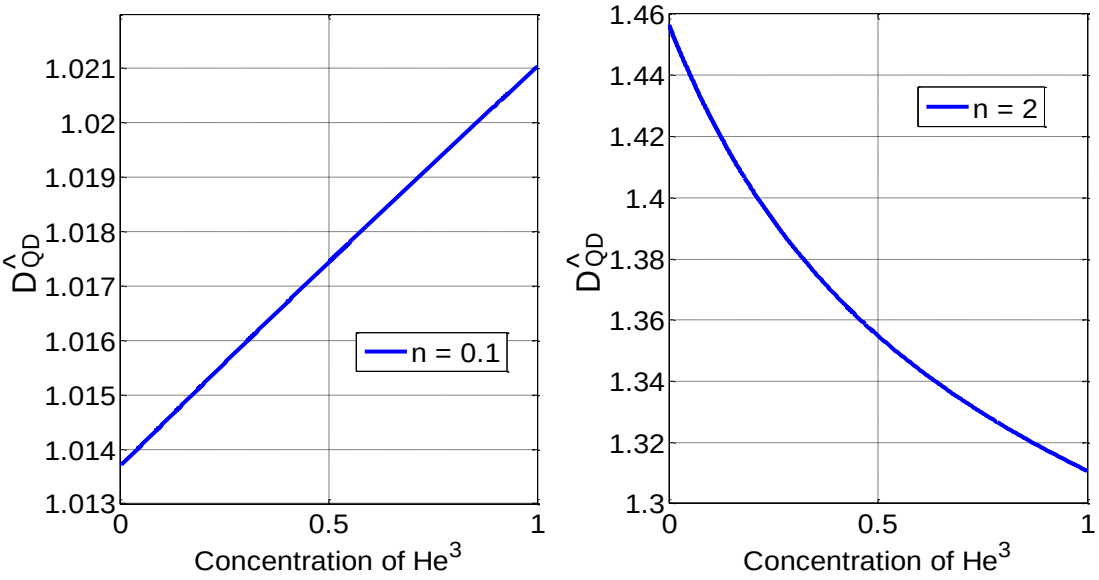

Figure 2.15. Variation of diffusion coefficient with concentration showing the degeneracy effect [55].

2.2.2 Steady State Distribution Function and Density Distribution

The equilibrium-based steady state distribution function for ideal Fermion and Boson gases confined in a rectangular nano-channel is developed [56]. It is given by

$$f = f_0 - \tau v_{w,r} \frac{\partial f_0}{\partial x_r} \tag{2.21}$$

$$f = f_0 - \frac{\tau v_{w,r}}{k_b T} \frac{1}{V} \frac{\exp(B_w)}{(\exp(B_w) \pm 1)^2} \left(F_r^{\mu_q} + F_r^{\varphi} + B_w F_r^T\right) \tag{2.22}$$

where τ is the relaxation time and $v_{w,r}$ is the velocity component in the direction r of a particle in quantum state w. $B_w = (\varepsilon_w - \mu_q)/k_b T$, and $F_r^{\mu_q}, F_r^{\varphi}$, and F_r^T are the generalized orces defined by the gradient of the quantum chemical potential, external potential and temperature, respectively. ε_w is the energy eigenvalues of quantum state w. This distribution function is used to derive the particle and energy fluxes for steady state expressed as

$$J_1^N = \frac{l_g}{k_b T\, V} \left(\frac{2\, k_b T}{m}\right)^{1/2} \left(g_0 F_1^{\phi T} + g_2 F_1^T\right) \tag{2.23}$$

$$J_1^E = \frac{l_g}{V}\left(\frac{2\,k_b T}{m}\right)^{1/2}\left(g_2 F_1^{\phi T} + g_4 F_1^{T}\right) \tag{2.24}$$

where the dimensionless quantity g_a is defined as

$$g_a = \sum_w \frac{m v_{w,1}^2 / 2\,k_b T}{(\varepsilon_w / k_b T)^{\frac{1-a}{2}}} \frac{\exp(B_w)}{(\exp(B_w) \pm 1)^2} \tag{2.25}$$

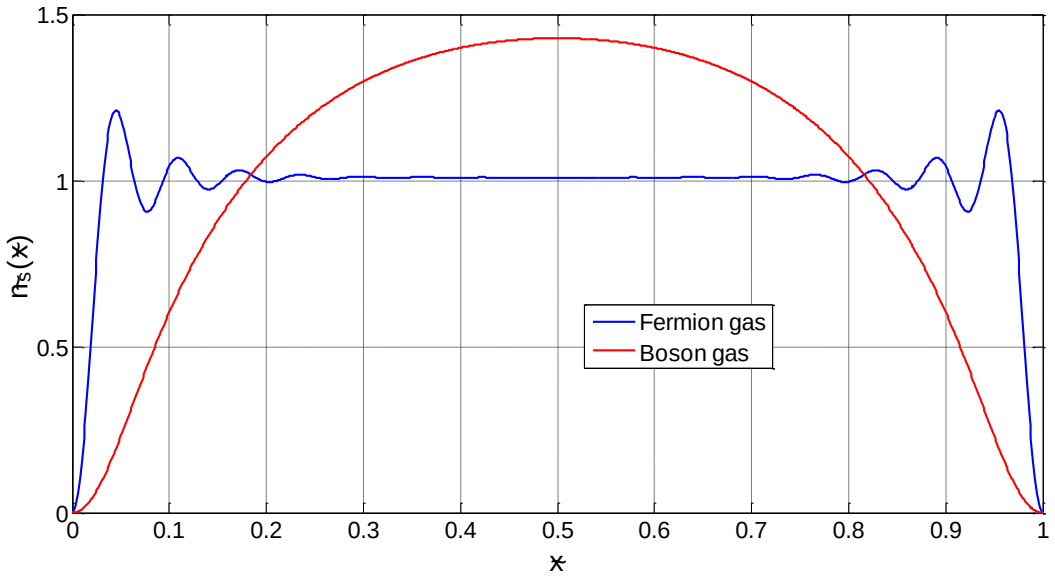

Figure 2.16. Dimensionless density distribution of ideal monatomic Bose and Fermi gases [56].

Note that the distribution function equation (2.22) is unable to capture actual non-equilibrium effects since it is based on the grand canonical distribution and partition function of stable equilibrium. Likewise the density distribution of particles at the nanoscale is developed that for Fermion and Boson gases in [51-53, 56] using the same equilibrium basis so

$$n(x) = \sum_w \frac{|\varphi_w(x)|^2}{\exp(\frac{-\Lambda + \varepsilon_w}{k_b T}) \pm 1} \tag{2.26}$$

where $\Lambda = \mu/k_b T$ is the dimensionless chemical potential. $\varphi_w(x)$ and ε_w are the energy eigenfunction and eigenvalue of the system in quantum state w. It is both this density distribution and the distribution function of equation (2.22) that are developed in the present doctoral research on a non-equilibrium instead of equilibrium basis not only for steady state but transient diffusion as well.

Finally, Figure 2.16 shows the spatial variation of the dimensionless density distribution (i.e., $\hat{n} = n_s/n_q$ where $n_q = 1/\lambda_{th}$ and $\lambda_{th} = 2L_c/\sqrt{\pi}$, for Boson ($He^4$) and Fermion ($He^3$) gases confined in rectangular domain with $\alpha = 0.2$, and $\Lambda = 10$ for the Fermion gas and $\Lambda = -0.05$ for the Boson gas. As seen in the figure, the density distribution at the boundary goes to zero, and as expected Friedel oscillations are observed in the region close to the boundary for the Fermi gas [53, 54, 56].

Chapter 3 - EAQT Modeling of the Diffusivities of He^3 in He^4

3.1 Mathematical Model

This chapter introduces the fundamental concepts of diffusion occurring in an isolated closed system in which He^3 diffuses in He^4, and focuses on understanding the non-equilibrium behavior predicted by the SEAQT framework of diffusion at the nanoscale (i.e., at the atomistic level). For the case when the equilibrium boson and fermion distribution functions are used, the system is viewed as a boson (i.e., when He^3 diffuses on He^4) or fermion (i.e., when He^4 diffuses on He^3) ensemble of a single particle. For the case when the boson and fermion distribution functions are based on the density operator of SEAQT description, the system is considered to be an ensemble of two particles (i.e., two He^3 or two He^4). The reason is that in the first case, the equilibrium-based distribution function for bosons and fermions, which is analytically derived via the maximum entropy principle, consists of a single expression that captures both boson and fermion behavior but that depends only on the quantum probability of eigenfunction of a single particle. In contrast, in the second case, the non-equilibrium-based distribution function derived from SEAQT is unable to distinguish between boson and fermion behavior unless the quantum probability in the expression for this distribution function depends on the eigenfunction of at least two identical particles, i.e., two bosons or two fermions. In other words, two different approaches are used in order to model and study the diffusion of He^3 and He^4. The first is equilibrium-based and depends on a single-particle ensemble while the second is non-equilibrium-based and depends on a two-particle ensemble.

Note that in physics the fundamental difference between bosons and fermions is simply the spin. Bosons have integer spin while fermions have half-integer spin. As a consequence, bosons can occupy the same energy eigenstate at the same time while fermions cannot occupy the same energy eigenstate at the same time. In the case of He^4 and He^3, the nucleus of He^4 consists of two protons and two neutrons, while that for He^3 has two protons and one neutron. Each proton and neutron has a half-integer spin. When adding the number of spins for protons and neutrons for each nucleus, the spin for He^4 results in an integer spin, which makes it a boson, and the spin for He^3 results in a half-integer spin, which makes it a fermion.

For the case of the single-particle ensemble, the translational energy eigenvalue problem for a single particle is solved analytically after which the equilibrium distribution functions for He^3 and He^4 are determined using the quantum probabilities of the single-particle eigenfunctions found from the eigenvalue problem. The boson and fermion density distributions are then used in modeling and evaluating the diffusivities of both bosons and fermions. For a two-particle system, the translational energy eigenvalues problem for two identical particles is solved analytically. However, an equilibrium distribution function for the two-particle case is not constructed since it is replaced with one that not only depends on the quantum probabilities of the two-particle eigenfunctions but as well on the time-dependent density operator of the IQT/SEAQT equation of motion, thus, capturing both non-equilibrium and equilibrium behavior of He^3 and He^4. At stable equilibrium, the diffusivities obtained from the IQT/SEAQT approach capture the same trends of those obtained from equilibrium-based approach. Clearly, the non-equilibrium predictions are completely original with no counterpart in the literature. Thus, the principle goal here is to demonstrate the ability of the SEAQT framework to capture the non-equilibrium and equilibrium behavior of bosons and fermions and to validate at least the equilibrium results of the SEAQT framework with what is found in the literature.

3.1.1 System Description

The thermodynamic system under consideration is that of the isolated system shown in Figure 3.1. It consists of He^3 and He^4 confined to a box of length L. The He^3 and He^4 are assumed to behave as an ideal Fermi-Dirac gas (fermions) and an ideal Bose-Einstein gas (bosons), respectively. In order to simplify the model of the diffusion at non-equilibrium, it is assumed that the system contains two He^3 particles and two He^4 particles in a box of length L (i.e., in x direction) and is studied at very low temperature and pressure. These particles are spin-less and non-interacting.

3.1.2 Translational Energy Eigenvalue Problem

3.1.2.1 Single-particle System

Since only monatomic non-interacting particles are considered here, only the translational energy eigenmode with zero potential energy inside the system is relevant. Thus, the energy

eigenvalue problem (i.e., the time-independent Schrödinger equation) for a free particle in a box is required. In one dimension it is written as follows [10, 23, 29, 50]:

$$-\frac{\hbar^2}{2\,m}\frac{\partial^2\,\psi(x)}{\partial x^2}=e_{tr}\,\psi(x) \tag{3.1}$$

Only one dimension is considered here since a prediction of diffusion in the x direction only is desired. Here, the eigenfunction ψ is a function of position, e_{tr} is the translational energy eigenvalue, $\hbar$ is the reduced Planck's constant, and m is the mass of the particle. It is noteworthy that the walls of the box have infinite potential energy to ensure that the probability of finding the particle at the walls or outside the box is zero. That leads to all eigenfunctions at the walls being zero, i.e., Dirichlet boundary conditions [23, 28, 29, 50, 69], i.e.,

$$\text{at } x=0\ \Rightarrow\psi(0)=0\quad\text{ and }\quad\text{at } x=L\ \Rightarrow\psi(L)=0 \tag{3.2}$$

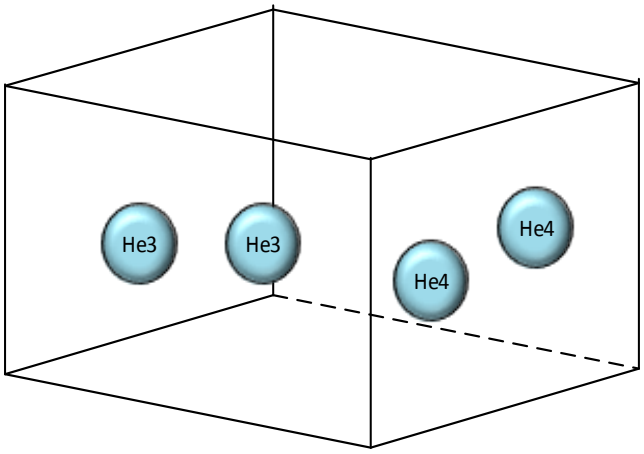

Figure 3.1. An isolated system of He^3 and He^4.

Applying the boundary conditions and using the normalization condition [35], the eigenvalue problem is solved analytically. The energy eigenvalues are given by

$$e_{tr}=\frac{\hbar^2\,\pi^2\,k^2}{2\,m\,L^2},\quad k=1,2,\ldots \tag{3.3}$$

while the eigenfunctions take the form

$$\psi(x) = \sqrt{\frac{2}{L}} \sin\left(\frac{k\,\pi\,x}{L}\right) \tag{3.4}$$

Here, the integers k are the translational quantum numbers for the system, and run from one to infinity. The dimensionless form of the energy eigenvalue [51, 52, 55] is written as follows:

$$\frac{e_{tr}}{T\,k_b} = (\alpha\,k)^2 \tag{3.5}$$

where

$$\alpha = \frac{L_c(T)}{L} \tag{3.6}$$

and the length $L_c(T)$ is one half of the most probable de Broglie wavelength of particles [53, 54, 56], and is obtained from

$$L_c(T) = \frac{h}{\sqrt{(8\,m\,k_b\,T)}} \tag{3.7}$$

where h is Planck's constant, k_b is Boltzmann's constant, and T is the temperature of the system in degree Kelvin. The α is, thus, a dimensionless scale factor related to $L_c(T)$, which is the length below which quantum size effects become appreciable [56].

3.1.2.2 Two-particle System

For the case of two identical particles of mass m in a one-dimensional box of length L, the energy eigenvalue problem [28, 29] is given by

$$\frac{-\hbar^2}{2\,m}\left(\frac{\partial^2\psi}{\partial {x_1}^2}\right) + \frac{-\hbar^2}{2\,m}\left(\frac{\partial^2\psi}{\partial {x_2}^2}\right) + V_{12}\;\psi(x_1,x_2) = e_{tr}\;\psi(x_1,x_2) \tag{3.8}$$

Here, ψ is the eigenfunction which is a function of the spatial coordinates of both particles. As in the one-particle case, the potential energy V_{12} describing the two-particle system is equal to zero because the particles are non-interacting. As before, the potential energy is infinite at the walls or outside the box in order to maintain the assumption that the probability of finding a particle at the walls or outside the box is equal to zero. Note that the energy eigenvalue problem for two identical particles in one dimension is equivalent to the energy eigenvalue problem of a single

particle in two dimensions. In other words, the system obeys the Dirichlet boundary conditions [25, 29] such that

$$\psi(0, x_2) = 0, \quad \psi(L, x_2) = 0$$
$$\psi(x_1, 0) = 0, \quad \psi(x_1, L) = 0 \tag{3.9}$$

Solution of this eigenvalue problem yields a translational eigenenergy which is the sum of the independent translational eigenenergy of each particles such that

$$e_{tr} = d_0 \, (k_1^2 + k_2^2) \tag{3.10}$$

where

$$d_0 = \frac{\hbar^2 \, \pi^2}{2 \, m \, L^2} \tag{3.11}$$

For the case of two identical particles, the eigenfunctions are not simply the product of the eigenfunctions of each particle because of the indistinguishability of particles[12] in the quantum systems. Now, if the two identical particles are bosons as is the case of He^4, the eigenfunctions are given by [25, 28, 29]

$$\psi_{k_1 k_2}(x_1, x_2) = \frac{1}{\sqrt{2}} \left[\psi_{k_1}(x_1)\psi_{k_2}(x_2) + \psi_{k_1}(x_2)\psi_{k_2}(x_1)\right] \tag{3.12}$$

For Fermions, .i.e., He^3, the eigenfunctions [25, 28, 29] take the form

$$\psi_{k_1 k_2}(x_1, x_2) = \frac{1}{\sqrt{2}} \left[\psi_{k_1}(x_1)\psi_{k_2}(x_2) - \psi_{k_1}(x_2)\psi_{k_2}(x_1)\right] \tag{3.13}$$

The eigenfunctions for bosons are symmetric while those for fermions are anti-symmetric. By using the solutions of the energy eigenvalue problem for a single particle, the eigenfunction for both bosons and fermions for the two-particle case can be rewritten as follows:

$$\psi_{k_1 k_2}(x_1, x_2) = \frac{\sqrt{2}}{L_x}\left[\sin\left(\frac{k_1 \, \pi \, x_1}{L_x}\right) \sin\left(\frac{k_2 \, \pi \, x_2}{L_x}\right) \pm \sin\left(\frac{k_1 \, \pi \, x_2}{L_x}\right) \sin\left(\frac{k_2 \, \pi \, x_1}{L_x}\right)\right] \tag{3.14}$$

[12] In classical system, it is possible to know which particle is at which position, but in quantum system, it is impossible to distinguish between two identical particles or to know which particle is in which state in the quantum system.

where the positive sign $(+)$ and the negative sign $(-)$ are operative for bosons and fermions, respectively. In this expression, k_1 and k_2 are the quantum numbers for the two-particle energy eigenlevels, which x_1 and x_2 are the positions of two particles. Note that the ground state[13] for bosons has quantum numbers $k_1 = k_2 = 1$ and the translational eigenenergy is $e_t = 2\ d_0$. The first excited state has $k_1 = 1,\ k_2 = 2$ for which $e_t = 5\ d_0$. Here the first excited state is not degenerate because $k_1 = 1,\ k_2 = 2$ and $k_1 = 2,\ k_2 = 1$ give the same eigenfunction. Thus, the $5\ d_0$ energy state has a degeneracy of one. In case of fermions, the state $k_1 = k_2 = 1$ does not exist in this system because the eignfunctions vanish at these quantum numbers. Therefore, the ground state for fermions has quantum numbers $k_1 = 1,\ k_2 = 2$ with energy $e_t = 5\ d_0$. The first excited state has $k_1 = 1,\ k_2 = 3$ with energy $e_t = 10\ d_0$. Also, the first excited state for fermions is not degenerate. In other words, it is possible to have two or more particles in the same state in the case of bosons, while there exists only one particle in each state for fermions. Fermions obey the Pauli Exclusion Principle[14]. Table 3.1 shows the set of quantum numbers of the first fifth energy eigenlevels for bosons and of the first third energy eigenlevels for fermions.

Table 3.1. Quantum numbers for the two-particle, non-interacting Boson (He^4) and Fermions (He^3).

		He^4	**He^3**
$\boldsymbol{k_1}$	$\boldsymbol{k_2}$	$\boldsymbol{k_1^2 + k_2^2}$	$\boldsymbol{k_1^2 + k_2^2}$
1	1	2	-
1	2	5	5
2	2	8	-
1	3	10	10
2	3	13	13

[13] The ground state is the state that has the lowest eigenenergy.

[14] The Pauli Exclusion Principle states that two particles cannot have the same quantum number.

3.1.3 SEAQT Equation of Motion for an Isolated System

In general, the SEAQT mathematical framework provides a full descriptions of the kinetics and dynamics [64, 70] of a system at any scale (ranging from the microscopic to the macroscopic) undergoing any process (either reversible or irreversible) in any state (either stable equilibrium or not stable equilibrium) [44]. Equation (1.17) is used here to model the evolution in the state of the isolated system [38, 39] in time. Under the assumptions that the density operator ρ is diagonal in the Hamiltonian representation H and ρ commute [57], equation (1.17) reduces to

$$\frac{\partial \rho(t)}{\partial t} = -\frac{1}{\tau_D}\,\mathcal{D} \tag{3.15}$$

where τ_D is the relaxation time. The term $-\mathcal{D}/\tau_D$, the so-called dissipation term, moves the density operator ρ along the path of steepest entropy ascent while maintaining the energy of the system constant and gives rise to an increase in the entropy of the system due to the irreversibilities which occur for all non-equilibrium states not belonging to a limit cycle [44, 71] that relax to stable equilibrium. The dissipation operator $\mathcal{D}$ depends on the state operator ρ , $\ln \rho$, and the Hamiltonian operator and captures the nonlinear dynamics of the irreversible relaxation.

It is noteworthy that the density operator ρ is not always diagonal in the Hamiltonian representation (e.g., see [62, 64]). In such a case, the Hamiltonian operator H and the density operator ρ do not commute. In terms of eigenvalues ρ_i, equation (3.15) can be expressed in terms of a ratio of Gram determinants [38, 39] so that

$$\frac{\partial \rho_j}{\partial t} = -\frac{1}{\tau_D}\frac{\begin{vmatrix} \rho_j \ln \rho_j & \rho_j & e\rho_j \\ \sum_i \rho_i \ln \rho_i & 1 & \sum_i e_i \rho_i \\ \sum_i e\rho_i \ln \rho_i & \sum_i e_i \rho_i & \sum_i e_i^2 \rho_i \end{vmatrix}}{\begin{vmatrix} 1 & \sum_i e_i \rho_i \\ \sum_i e_i \rho_i & \sum_i e_i^2 \rho_i \end{vmatrix}} \tag{3.16}$$

for $i, j = 1,2, \ldots \ldots, \mathcal{M}$, where $\mathcal{M}$ is the number of energy eigenlevels. e is the energy eigenvalue of the system. Using the von Neumann expression for entropy in terms of the density operator from equation (3.16) can be rewritten to yield the rate of entropy generation for an isolated system, namely, [38, 39]

$$\frac{\partial S}{\partial t} = \frac{k_B}{\tau_D} \frac{\begin{vmatrix} \sum_i \rho_i \ (\ln \rho_i)^2 & \sum_i \rho_i \ln \rho_i & \sum_i e_i \rho_i \ln \rho_i \\ \sum_i \rho_i \ln \rho_i & 1 & \sum_i e_i \rho_i \\ \sum_i e_i \rho_i \ln \rho_i & \sum_i e_i \rho_i & \sum_i e_i^2 \rho_i \end{vmatrix}}{\begin{vmatrix} 1 & \sum_i e_i \rho_i \\ \sum_i e_i \rho_i & \sum_i e_i^2 \rho_i \end{vmatrix}} \tag{3.17}$$

Here k_b is the Boltzmann constant[15]. Note that the ratio of Gram determinants is always nonnegative. In other words, the rate of entropy generation is nonnegative at all times.

3.1.4 Density Distribution of Particles

3.1.4.1 Derivation of the Equilibrium-based Density Distribution

For ideal quantum gases, the equilibrium distribution function, $f_{eq}(x,y,z)$, that depends on the canonical or grand canonical distributions and partition functions found at stable equilibrium and that uses the quantum probability [33, 51, 53, 55, 56, 72] is given by

$$f_{eq_r}(x,y,z) = \frac{|\psi_r(x,y,z)|^2}{\exp\left[\frac{e_r - \mu}{k_b T}\right] \pm 1} \tag{3.18}$$

where the subscript "eq" stands for equilibrium e_r and ψ_r are the energy eigenvalue and the eigenfunction of a particle in quantum state r, respectively, μ, and T are the chemical potential and temperature of the system, respectively. The negative sign $(-)$ and positive sign $(+)$ are for bosons and fermions, respectively. The numerator of this expression represents the quantum probability, while the denominator is the Bose-Einstein or Fermi-Dirac factor for bosons or fermions [35]. The density distribution of particles, $n_{eq}(x,y,z)$, can then be obtained by summing the distribution function over all quantum states r such that

$$n_{eq}(x,y,z) = \sum_r \frac{|\psi_r(x,y,z)|^2}{\exp\left[\frac{e_r - \mu}{k_b T}\right] \pm 1} \tag{3.19}$$

Note that the density distribution $n_{eq}(x,y,z)$ depends only upon position because the eigenfunction $\psi_r(x,y,z)$ is only a function of position and does not depend on time. For one dimension, this density distribution of particles [51, 56] reduces to

[15] $k_B = 1.2806 \ X \ 10^{-23} \ J/K$

$$n_{eq}(\tilde{x}) = \sum_{r} \frac{|\psi_r(\tilde{x})|^2}{\exp[\tilde{e} - \Lambda] \pm 1} \tag{3.20}$$

where, $\tilde{e}$ and $\psi_r(\tilde{x})$ are the dimensionless energy eigenvalue and the eigenfunction, respectively. Λ is the dimensionless chemical potential and is independent of position, i.e., it is global constant, while $\tilde{x}$ is the dimensionless position. These dimensionless variables used are given as

$$\begin{aligned} \Lambda &= \frac{\mu}{k_b T} \\ \tilde{e} &= \frac{e}{\mathrm{k_b T}} = (\alpha_x k_x)^2 \\ \psi_{k_x}(\tilde{x}) &= \sqrt{\frac{2}{L}} \sin(k_x \pi \tilde{x}) \\ \tilde{x} &= \frac{x}{L} \end{aligned} \tag{3.21}$$

The classical density distribution of particles, n_{cl} , is obtained by dividing the total number of particles, N, into the volume of the system; and N is obtained by integrating the density distribution of particles over the domain. Thus, the classical density of particles, n_{cl} , is given as

$$n_{cl} = \frac{N}{L} = \frac{1}{\tilde{L}} \int_0^{\tilde{L}} n_{eq}(\tilde{x})\, d\tilde{x} \tag{3.22}$$

$$n_{cl} = \frac{1}{\tilde{L}} \sum_{k_x} \int_0^{\tilde{L}} \frac{\left| \sqrt{\frac{2}{L}} \sin(k_x \pi \tilde{x}) \right|^2}{\exp[(\alpha_x k_x)^2 - \Lambda] \pm 1}\, d\tilde{x} \tag{3.23}$$

Here, $\tilde{L} = 1$. Note that the integral of the squared of the modulus of the eigenfunction is equal to one such that

$$\int_0^{\tilde{L}} \left| \sqrt{\frac{2}{L}} \sin(k_x \pi \tilde{x}) \right|^2 d\tilde{x} = 1 \tag{3.24}$$

This is the so-called normalization condition. The classical density distribution of particles then reduces to the form

$$n_{cl} = \frac{1}{\tilde{L}} \sum_{k_x} \frac{1}{\exp[(\alpha_x k_x)^2 - \Lambda] \pm 1} \tag{3.25}$$

Finally, the dimensionless form of the equilibrium density distribution [51, 56] is obtained by dividing the equilibrium density distribution of particles by the classical density distribution of particles, i.e.,

$$\tilde{n}_{eq}(\tilde{x}) = \frac{n_{eq}(\tilde{x})}{n_{cl}} \tag{3.26}$$

Substituting, equation (3.20), (3.21), and (3.25), the dimensionless form of the equilibrium density distribution of particles in one dimension can be written as

$$\tilde{n}_{eq}(\tilde{x}) = \frac{\sum_{k_x} \frac{\left|\sqrt{\frac{2}{L}} \sin(k_x\, \pi\, \tilde{x})\right|^2}{\exp[(\alpha_x k_x)^2 - \Lambda] \pm 1}}{\frac{1}{\tilde{L}} \sum_{k_x} \frac{1}{\exp[(\alpha_x k_x)^2 - \Lambda] \pm 1}} \tag{3.27}$$

where k_x is the quantum number (integer number) running from one to infinity.

3.1.4.2 Derivation of the Non-equilibrium-based Density Distribution

In general, the non-equilibrium distribution function, $f_{neq_r}(x, y, z, t)$, is constructed by combining the density operator $\rho_r(t)$ obtained from solving the SEAQT equation of motion for the system undergoing the dissipative process and the quantum probability obtaining from the square of the modulus the eigenfunction $\psi_r(x, y, z)$. It is given by

$$f_{neq_r}(x, y, z, t) = \rho_r(t)\, |\psi_r(x, y, z)|^2 \tag{3.28}$$

The subscript "neq" stands for non-equilibrium, and r again is the quantum state. In order to capture the non-equilibrium behaviour of Fermi-Dirac and Bose-Einstein ideal gases, the eigenfunctions of two identical particles are used instead of the eigenfunction of a single particle. Thus, the non-equilibrium distribution function for two identical particles in three dimensions is written as

$$f_{neq_r}(x_1, y_1, z_1, x_2, y_2, z_2, t) = \rho_r(t)\, |\psi_r(x_1, y_1, z_1, x_2, y_2, z_2)|^2 \tag{3.29}$$

For a single dimension, this reduces to

$$f_{neq_r}(x_1, x_2, t) = \rho_{k_1 k_2}(t) \left|\psi_{k_1 k_2}(x_1, x_2)\right|^2 \tag{3.30}$$

where the subscript 'r' has been replaced with the quantum number of each particle. The non-equilibrium density distribution for two identical particles in one dimension is then constructed form the non-equilibrium distribution function as follows:

$$n_{neq}(x_1, x_2, t) = \sum_{k_1 k_2} \rho_{k_1 k_2}(t) \left|\psi_{k_1 k_2}(x_1, x_2)\right|^2 \tag{3.31}$$

Substituting equation (3.14) into equation (3.31) and using the dimensionless position, the non-equilibrium density distribution of two identical particles is rewritten as follows:

$$\begin{aligned} n_{neq}(\tilde{x}_1, \tilde{x}_2, t) = \frac{\sqrt{2}}{L} \sum_{k_1 k_2} \rho_{k_1 k_2}(t) \, |\sin(k_1 \pi \tilde{x}_1) \, \sin(k_2 \pi \tilde{x}_2) \\ \pm \sin(k_1 \pi \tilde{x}_2) \, \sin(k_2 \pi \tilde{x}_1)|^2 \end{aligned} \tag{3.32}$$

Again the positive and negative $(\pm)$ signs stand for bosons and fermions, respectively. $\tilde{x}_1$ and $\tilde{x}_2$ are the dimensionless positions of the two particles expressed as

$$\tilde{x}_1 = \frac{x_1}{L}, \quad \tilde{x}_2 = \frac{x_2}{L} \tag{3.33}$$

For the two-particle system, the classical density [51] is obtained from the non-equilibrium distribution function such that

$$n_{cl_{neq}}(t) = \frac{N}{L} = \frac{1}{L} \iint_0^L n_{neq}(\tilde{x}_1, \tilde{x}_2, t) \, d\tilde{x}_1 d\tilde{x}_2 \tag{3.34}$$

$$n_{cl_{neq}}(t) = \frac{1}{L} \sum_{k_1 k} \rho_{k_1 k_2}(t) \iint_0^L \left|\psi_{k_1 k_2}(x_1, x_2)\right|^2 d\tilde{x}_1 d\tilde{x}_2 \tag{3.35}$$

The double integral of the square of the modulus of the eigenfunction is the normalization condition given by

$$\iint_0^L \left|\psi_{k_1 k_2}(x_1, x_2)\right|^2 d\tilde{x}_1 d\tilde{x}_2 = 1 \tag{3.36}$$

Equation (3.35) can, thus, be rewritten in the form

$$n_{cl_{neq}}(t) = \frac{1}{L}\sum_{k_1 k_2} \rho_{k_1 k_2}(t) \tag{3.37}$$

The dimensionless form of the non-equilibrium distribution for two identical particles then becomes

$$\tilde{n}_{neq}(\tilde{x}_1, \tilde{x}_2, t) = \frac{\sum_{k_1 k} \rho_{k_1 k_2}(t)\ |\sin(k_1\,\pi\,\tilde{x}_1)\ \sin(k_2\,\pi\,\tilde{x}_2) \pm \sin(k_1\,\pi\,\tilde{x}_2)\ \sin(k_2\,\pi\,\tilde{x}_1)|^2}{\sum_{k_1 k_2} \rho_{k_1 k_2}(t)} \tag{3.38}$$

The latter equation can be rewritten as follows

$$\tilde{n}_{neq}(\tilde{x}_1, \tilde{x}_2, t) = \frac{\sum_{k_1 k_2} \rho_{k_1 k_2}(t)\ \left|g_{k_1 k_2}(\tilde{x}_1, \tilde{x}_2)\right|^2}{\sum_{k_1 k_2} \rho_{k_1 k_2}(t)} \tag{3.39}$$

where the function $g_{k_1 k_2}(\tilde{x}_1, \tilde{x}_2)$ is used for convenience and is expressed as

$$g_{k_1 k_2}(\tilde{x}_1, \tilde{x}_2) = \sin(k_1\,\pi\,\tilde{x}_1)\ \sin(k_2\,\pi\,\tilde{x}_2) \pm \sin(k_1\,\pi\,\tilde{x}_2)\ \sin(k_2\,\pi\,\tilde{x}_1) \tag{3.40}$$

As before, density operator $\rho_{k_1 k_2}(t)$ is obtained by solving the SEAQT equation of motion and is a function of time only. The dimensionless form for the non-equilibrium density distribution of one particle is obtained from integrating the dimensionless form for the non-equilibrium density distribution of two particles with respect to the position of the second particle so that

$$\tilde{n}_{neq}(\tilde{x}_1, t) = \int_0^L \tilde{n}_{neq}(\tilde{x}_1, \tilde{x}_2, t)\ d\tilde{x}_2 \tag{3.41}$$

3.1.5 Diffusivities of Ideal Quantum Gases

In order to derive expression for the diffusivity, the numerator and denominator of equation (1.6) is multiplied by the derivative with respect to x of the density distribution of the particle dn/dx such that

$$J_x = -\frac{\sum_r \tau\ v_{x_r}^2 \frac{df_r}{dx}}{\frac{dn}{dx}} \frac{dn}{dx} \tag{3.42}$$

This equation for the mass flux in the x direction matches the diffusion equation [9, 12], which can be written as follows:

$$J_x = -D\frac{dn}{dx} \tag{3.43}$$

where the term D stands for diffusivity (diffusion coefficient). Substituting for n in terms of the distribution function f_r the diffusivity as a function of x can be written as

$$D(x) = \frac{\sum_i \tau\, v_{x_i}^2 \frac{df_i}{dx}}{\sum_i \frac{df_i}{dx}} \tag{3.44}$$

This last equation is the basis for the derivation of the expression for the non-equilibrium and equilibrium based diffusivities.

3.1.5.1 Derivation of the Equilibrium-based Diffusivity

Using the equilibrium distribution function, the diffusivity in one dimension can be written as follows:

$$D_{eq}(x) = \frac{\sum_r \tau\, v_{x_r}^2 \frac{d}{dx} f_{eq_r}(x)}{\sum_r \frac{d}{dx} f_{eq_r}(x)} \tag{3.45}$$

As mentioned in *Chapter* 1, τ and v_x are the relaxation time and velocity of the particle in the x direction, respectively. The relaxation time is the mean free path divided by the particle velocity. This velocity is calculated by equating the kinetic energy with the energy eigenvalue such that

$$e_{tot} = \frac{1}{2}mv^2 \Longrightarrow v = \left(\frac{2}{m}\, e_{tot}\right)^{\frac{1}{2}} \Rightarrow v = \left(\frac{2}{m}\, \frac{\hbar^2\, \pi^2\, {k_x}^2}{2\, m\, L^2}\right)^{\frac{1}{2}} \Longrightarrow v = v_x \tag{3.46}$$

Using τ, v_x, and $f_{eq_r}(x)$, equation (3.45) becomes

$$D_{eq}(x) = \frac{\sum_{k_x} \frac{l_g\, \hbar\, \pi}{m\, L} k_x \frac{\frac{d}{dx}\left|\sqrt{\frac{2}{L}} \sin\left(\frac{k_x\, \pi\, x}{L}\right)\right|^2}{\exp[(\alpha_x k_x)^2 - \Lambda] \pm 1}}{\sum_{k_x} \frac{\frac{d}{dx}\left|\sqrt{\frac{2}{L}} \sin\left(\frac{k_x\, \pi\, x}{L}\right)\right|^2}{\exp[(\alpha_x k_x)^2 - \Lambda] \pm 1}} \tag{3.47}$$

The derivative of the square of the modulus of the sine function is given by

$$\frac{d}{dx}\left|\sqrt{\frac{2}{L}}\sin\left(\frac{k_x\,\pi\,x}{L}\right)\right|^2 = \frac{4\,k_x\,\pi}{L^2}\cos\left(\frac{k_x\,\pi\,x}{L}\right)\sin\left(\frac{k_x\,\pi\,x}{L}\right) = \frac{2\,n_x\,\pi}{L^2}\sin\left(\frac{2\,k_x\,\pi\,x}{L}\right) \tag{3.48}$$

The equilibrium-based diffusivity can then be written in the form

$$D_{eq}(\tilde{x}) = \left(\frac{l_g\,\hbar\,\pi}{m\,L}\right)\left(\frac{\sum_{k_x}\frac{{k_x}^2\sin(2\,k_x\,\pi\,\tilde{x})}{\exp[(\alpha_x k_x)^2-\Lambda]\pm 1}}{\sum_{k_x}\frac{k_x\sin(2\,k_x\,\pi\,\tilde{x})}{\exp[(\alpha_x k_x)^2-\Lambda]\pm 1}}\right) \tag{3.49}$$

In this equation and equation (3.47), l_g is the mean free path and m the mass of the particle. As before, the positive and negative $(\pm)$ signs stand for Fermi-Dirac and Bose-Einstein gases, respectively. Note that the term in the first set of parentheses has units of length squared per unit time which are the unit of diffusivity.

The dimensionless form of the equilibrium-based diffusivity is obtained by dividing through by the first term, to the right of the equals so that

$$\tilde{D}_{eq}(\tilde{x}) = \left(\frac{\sum_{k_x}\frac{{k_x}^2\sin(2\,k_x\,\pi\,\tilde{x})}{\exp[(\alpha_x k_x)^2-\Lambda]\pm 1}}{\sum_{k_x}\frac{k_x\sin(2\,k_x\,\pi\,\tilde{x})}{\exp[(\alpha_x k_x)^2-\Lambda]\pm 1}}\right) \tag{3.50}$$

The ratio of the diffusivities for He^3 to He^4 is then obtained [55] as follows:

$$\tilde{D}_{ratio_{eq}} = \frac{\tilde{D}_{He3_{eq}}}{\tilde{D}_{He4_{eq}}} \tag{3.51}$$

where

$$\tilde{D}_{He3_{eq}} = \left(\frac{\sum_{k_x}\frac{{k_x}^2\sin(2\,k_x\,\pi\,\tilde{x})}{\exp[(\alpha_3 k_x)^2-\Lambda_3]+1}}{\sum_{k_x}\frac{k_x\sin(2\,k_x\,\pi\,\tilde{x})}{\exp[(\alpha_3 k_x)^2-\Lambda_3]+1}}\right) \tag{3.52}$$

$$\widetilde{D}_{He4_{eq}} = \left(\frac{\sum_{k_x} \frac{{k_x}^2 \sin(2\, k_x\, \pi\, \tilde{x})}{\exp[(\alpha_4 k_x)^2 - \Lambda_4] - 1}}{\sum_{k_x} \frac{k_x \sin(2\, k_x\, \pi\, \tilde{x})}{\exp[(\alpha_4 k_x)^2 - \Lambda_4] - 1}} \right)$$

$\widetilde{D}_{He3_{eq}}$ and $\widetilde{D}_{He4_{eq}}$ are the dimensionless diffusivities for He^3 and He^4, respectively, Λ_3 and Λ_4 are their dimensionless chemical potentials, and α_3 and α_4 are the dimensionless length given by equation (3.6).

3.1.5.2 Derivation of the Non-equilibrium-based Diffusivity

Derivation of the non-equilibrium-based diffusivity begins with the two-particle non-equilibrium distribution function $f_{neq_r}(x_1, x_2, t)$ and an equation similar to that for the equilibrium-based diffusivity, i.e.,

$$D_{neq}(x_1, x_2, t) = \frac{\sum_r \tau\, v_{x_{1r}}^2 \frac{d}{dx_1} f_{neq_r}(x_1, x_2, t)}{\sum_r \frac{d}{dx_1} f_{neq_r}(x_1, x_2, t)} \tag{3.53}$$

In equation (3.53), x_1 and x_2 are the position of particle 1 and particle 2, respectively. Also, in this equation, the non-equilibrium distribution function depends upon both the density operator $\rho(t)$ and the eigenfunctions of two identical particles $\psi_{k_1,k_2}(x_1, x_2)$, capturing the non-equilibrium behavior of bosons and fermions. The relaxation time is obtained from the mean free path l_g and the total velocity v as is done in the previous section. The total velocity of the two particles in one dimension is obtained by equating the kinetic energy with the eigenvalue of the two particles such that

$$e_{tot} = \frac{1}{2} m v^2 \Longrightarrow\ v = \left(\frac{2}{m}\, e_{tot} \right)^{1/2} \Rightarrow\ v = \left(\frac{2}{m}\, \frac{\hbar^2\, \pi^2}{2\, m\, L^2}\, (k_1^2 + k_2^2) \right)^{1/2} \tag{3.54}$$

Then the velocity of one particle in the x_1 direction is given by

$$e_{x_1} = \frac{1}{2} m v^2 \Longrightarrow\ v_{x_1} = \left(\frac{2}{m}\, e_{x_1} \right)^{1/2} \Rightarrow\ v_{x_1} = \left(\frac{2}{m}\, \frac{\hbar^2\, \pi^2}{2\, m\, L^2}\, (k_1^2) \right)^{1/2} \tag{3.55}$$

Substituting $\rho(t)$, $\psi_{k_1,k_2}(x_1, x_2)$, τ, v, and v_{x_1} into equation (3.53) results in the following expression for the non-equilibrium-based diffusivity:

$$D_{neq}(x_1,x_2,t) = \frac{\sum_{k_1k_2} \frac{l_g \hbar \pi}{m L} \frac{k_1^2}{\sqrt{k_1^2+k_2^2}} \rho_{k_1k_2}(t) \ \frac{d}{dx_1} \left|\psi_{k_1k_2}(x_1,x_2)\right|^2}{\sum_{k_1k_2} \rho_{k_1k_2}(t) \ \frac{d}{dx_1} \left|\psi_{k_1k_2}(x_1,x_2)\right|^2} \tag{3.56}$$

The derivative with respect to x_1 of the square of the modulus of the eigenfunction is then written as

$$\frac{d}{dx_1} \left|\psi_{n_1n_2}(x_1,x_2)\right|^2 = \frac{4\pi}{L^3}\left(Q_1(x_1,x_2) \pm Q_2(x_1,x_2)\right) \tag{3.57}$$

where the positive and negative ($\pm$) signs apply for bosons and fermions, respectively, and $Q_1(x_1,x_2)$ and $Q_2(x_1,x_2)$ are used for convenience and defined by

$$\begin{aligned} Q_1(x_1,x_2) &= q_1(x_1,x_2) + q_2(x_1,x_2) \\ Q_2(x_1,x_2) &= q_3(x_1,x_2) + q_4(x_1,x_2) \end{aligned} \tag{3.58}$$

With q_1, q_2, q_3, and q_4 derived from the eigenfunctions for the two-particle translational eigenvalue problem, i.e.,

$$\begin{aligned} q_1(x_1,x_2) &= \frac{k_1}{2}\left[\sin\left(\frac{2\,k_1\,\pi\,x_1}{L}\right) \sin^2\left(\frac{k_2\,\pi\,x_2}{L}\right)\right] \\ q_2(x_1,x_2) &= \frac{k_2}{2}\left[\sin\left(\frac{2\,k_2\,\pi\,x_1}{L}\right) \sin^2\left(\frac{k_1\,\pi\,x_2}{L}\right)\right] \\ q_3(x_1,x_2) &= k_1\left[\cos\left(\frac{k_1\,\pi\,x_1}{L}\right) \sin\left(\frac{k_2\,\pi\,x_1}{L}\right)\sin\left(\frac{k_1\,\pi\,x_2}{L}\right)\sin\left(\frac{k_2\,\pi\,x_2}{L}\right)\right] \\ q_4(x_1,x_2) &= k_2\left[\cos\left(\frac{k_2\,\pi\,x_1}{L}\right)\sin\left(\frac{k_1\,\pi\,x_1}{L}\right) \sin\left(\frac{k_1\,\pi\,x_2}{L}\right)\sin\left(\frac{k_2\,\pi\,x_2}{L}\right)\right] \end{aligned} \tag{3.59}$$

Now, substituting the derivative evaluation of equations (3.57) to (3.59) into equation (3.56) transfroms the non-equilibrium-based diffusivity to the following:

$$\begin{aligned} &D_{neq}(x_1,x_2,t) \\ &= \left(\frac{l_g \hbar \pi}{m L}\right)\left(\frac{\sum_{k_1k_2} \frac{k_1^2}{\sqrt{k_1^2+k_2^2}} \rho_{k_1k_2}(t) \ \left(Q_1(x_1,x_2) \pm Q_2(x_1,x_2)\right)}{\sum_{k_1k_2} \rho_{k_1k_2}(t) \ \left(Q_1(x_1,x_2) \pm Q_2(x_1,x_2)\right)}\right) \end{aligned} \tag{3.60}$$

Note that again the units of the non-equilibrium-based diffusivity are given by the term in the first set of the parentheses to the right of the equals and are length squared per unit time. The dimensionless form of the non-equilibrium-based diffusivity is obtained by dividing equation (3.60) through by the term of $l_g \hbar \pi / m L$ so that

$$\tilde{D}_{neq}(\tilde{x}_1, \tilde{x}_2, t) = \left(\frac{\sum_{k_1 k_2} \frac{k_1^2}{\sqrt{k_1^2 + k_2^2}} \rho_{k_1 k_2}(t) \left(Q_1(\tilde{x}_1, \tilde{x}_2) \pm Q_2(\tilde{x}_1, \tilde{x}_2) \right)}{\sum_{k_1 k_2} \rho_{k_1 k_2}(t) \left(Q_1(\tilde{x}_1, \tilde{x}_2) \pm Q_2(\tilde{x}_1, \tilde{x}_2) \right)} \right) \tag{3.61}$$

Where $\tilde{x}_1$ and $\tilde{x}_2$ are the dimensionless positions as defined above. The ratio of the two-particle non-equilibrium-based diffusivities for He^3 to He^4 is then expressed as

$$\tilde{D}_{ratio_{neq}}(\tilde{x}_1, \tilde{x}_2, t) = \frac{\tilde{D}_{neq_{He3}}(\tilde{x}_1, \tilde{x}_2, t)}{\tilde{D}_{neq_{He4}}(\tilde{x}_1, \tilde{x}_2, t)} \tag{3.62}$$

where

$$\tilde{D}_{neq_{He3}}(\tilde{x}_1, \tilde{x}_2, t) = \left(\frac{\sum_{k_1 k_2} \frac{k_1^2}{\sqrt{k_1^2 + k_2^2}} \rho_{k_1 k_2}(t) \left(Q_1(\tilde{x}_1, \tilde{x}_2) - Q_2(\tilde{x}_1, \tilde{x}_2) \right)}{\sum_{k_1 k_2} \rho_{k_1 k_2}(t) \left(Q_1(\tilde{x}_1, \tilde{x}_2) - Q_2(\tilde{x}_1, \tilde{x}_2) \right)} \right) \tag{3.63}$$

$$\tilde{D}_{neq_{He4}}(\tilde{x}_1, \tilde{x}_2, t) = \left(\frac{\sum_{k_1 k_2} \frac{k_1^2}{\sqrt{k_1^2 + k_2^2}} \rho_{k_1 k_2}(t) \left(Q_1(\tilde{x}_1, \tilde{x}_2) + Q_2(\tilde{x}_1, \tilde{x}_2) \right)}{\sum_{k_1 k_2} \rho_{k_1 k_2}(t) \left(Q_1(\tilde{x}_1, \tilde{x}_2) + Q_2(\tilde{x}_1, \tilde{x}_2) \right)} \right) \tag{3.64}$$

In order to get the diffusivities for a single particle, the two-particle non-equilibrium-based diffusivity, equation (3.61), is integrated with the respect to the position of the other particle, namely,

$$\tilde{D}_{neq}(\tilde{x}_1, t) = \int_0^{\tilde{L}} \tilde{D}_{neq}(\tilde{x}_1, \tilde{x}_2, t) \, d\tilde{x}_2 \tag{3.65}$$

In addition, the ratio of the single-particle non-equilibrium-based diffusivities of He^3 to He^4 is obtained by integrating equation (3.62) with respect to the position of the other particle and is given by

$$\tilde{D}_{ratio_{neq}}(\tilde{x}_1, t) = \int_0^{\tilde{L}} \tilde{D}_{ratio_{neq}}(\tilde{x}_1, \tilde{x}_2, t)\, d\tilde{x}_2 \tag{3.66}$$

3.2 Numerical Approach

3.2.1 Solving IQT equation of motion

The SEAQT equation of motion, equation (3.16), is an evolution equation that describes how the thermodynamic state of system evolves in time given an initial condition, i.e., it represents an initial value problem (IVP). To obtain initial condition for this equation, the scheme on the outlined in [38, 39] can be used. It utilizes both a canonical and partially canonical distribution. The first of these is that for stable equilibrium for a given value of the system energy E and expressed as

$$\rho_j^{se}(E) = \frac{\exp(-\beta^{se}(E)\, e)}{\sum_{i=1}^{\mathcal{N}} \exp(-\beta^{se}(E)\, e_i)} \tag{3.67}$$

where ρ_j^{se} is the paobability distribution at stable equilibrium, e_j and e_i are energy eigenvalues of the system, and $\beta^{se}(E)$ is a parameter inversely proportional to the temperature, i.e.,

$$\beta^{se}(E) = \frac{1}{k_b\, T(E)} \tag{3.68}$$

The partially canonical equilibrium distribution for the same given value of the energy E and is given by

$$\rho_j^{pe}(E, \delta) = \frac{\boldsymbol{\delta}_j \exp\left(-\beta^{pe}(E, \boldsymbol{\delta})\, e_j\right)}{\sum_{i=1}^{\mathcal{N}} \exp(-\beta^{pe}(E, \boldsymbol{\delta})\, e_i)} \tag{3.69}$$

Here $\boldsymbol{\delta}$ is a time-invariant vector of length N with values of either 0 or 1 such that

$$\begin{aligned} \boldsymbol{\delta}_j = 0 &\implies \rho_j = 0 \\ \boldsymbol{\delta}_j = 1 &\implies \rho_j \neq 0 \end{aligned} \tag{3.70}$$

where $\mathcal{N}$ is the number of energy eigenlevels and ρ_j^{pe} the partially canonical probability distributions. The value of β^{pe} is obtained from the constraint on the system energy, i.e.,

$$\sum_{i=1}^{\mathcal{N}} \rho_j^{pe}(E, \boldsymbol{\delta})\, \varepsilon_i = E = E(\rho^{pe}(t_0)) \tag{3.71}$$

For a given $\boldsymbol{\delta}$, i.e., combination of 0's and 1's, equations (3.68) and (3.70) form a system of $N+1$ equations which must be solved to determine the associated partially canonical distributions and β^{pe} for a given system energy E. Once known, this distribution is used to determine the initial non-equilibrium density operator $\rho(t_0)$. This is done by perturbing the canonical and partially canonical distributions ρ_j^{se} and ρ_j^{pe} by a perturbation factor f_j and by normalizing such that

$$\rho_j = \frac{f_j\, \rho_j^{se}(E)}{\sum_{i=1}^{\mathcal{N}} f_i\, \rho_i^{se}(E)} \tag{3.72}$$

This last equation is the initial non-equilibrium distribution, which provides the initial non-equilibrium density operator $\rho(t_0)$ required by the SEAQT equation of motion. The perturbation factor f_j is given by

$$f_j = 1 - \lambda + \lambda\, \frac{\rho_j^{pe}(E, \boldsymbol{\delta})}{\rho_j^{se}(E)} \tag{3.73}$$

Where the perturbation parameter λ has values as $0 < \lambda < 1$. Once the initial non-equilibrium density operator is found, the SEAQT equation of motion of the isolated system is solved numerically to predict the state evolution in time of the system. It is noteworthy that the initial density operator is diagonal, and that holds true for the density operators obtained at each time, including that at stable equilibrium.

3.2.2 Chebyshev Nodes, Numerical Integration, and Singularity Treatment

The integrals of the functions of the density distributions and diffusivities found in equation (3.41), (3.64), and (3.65) must be evaluated numerically. To do so, the adaptive Simpson method based on Simpson's rule is used. The adaptive Simpson quadrature is done by executing the built-in function of MATLAB® called "quad" [73]. However, two problems occur when the numerical integrations are performed. The first is that singularities appear, in which infinite values at certain points are in an interval created by the dominators of the functions. These singularities are treated by using polynomial interpolations executed by using the built-in

functions of MATLAB® called "polyfit" and "polyval". The second is Runge's phenomenon [74-76] which is an oscillation at the edge of an interval when using polynomials of higher degree with equispaced interpolation points. This phenomenon is eliminated by using Chebyshev nodes [76, 77]. These nodes in the interval $[a, b]$ are givrn by

$$x_k = \left(\frac{a+b}{2} + \frac{b-a}{2}\cos\left(\frac{2k-1}{2\ \mathcal{M}}\pi\right)\right), \qquad k = 1,2,\dots,M \tag{3.74}$$

where $\mathcal{M}$ is the number of the nodes in the interval $[a, b]$. In order to execute the numerical integrations, the following steps are executed:

- Use the Chebyshev nodes in the interval $[a, b]$.
- Execute the adaptive Simpson quadrature using the built-in function of MATLAB® called "quad".
- Execute the polynomial interpolations using the built-in functions of MATLAB® called "polyfit" and "polyval".

Chapter 4 - Diffusion of Oxygen in a Tin Anode

4.1 Mathematical Model

The main goal of this chapter is to apply the SEAQT framework to an open system at the nanoscale in the region of not stable equilibrium states to demonstrate the effectiveness of this non-equilibrium approach for modeling and describing diffusion. The open system defined here is the diffusion of oxygen through a tin anode, and its energy eigenstructure is constructed based on the translational, vibrational, and rotational energy eigenvalues of an oxygen molecule which is a diatomic gas. Also, the extended form of the SEAQT equation of motion which includes the two-mass interactions is applied to model the transient and steady state evolution of this system. The models of the transient and steady state diffusivities are derived based on the density operator obtained from solving the SEAQT equation of motion, and eigenfunctions determined from solving the appropriate energy eigenvalue problems, which include those for rotation, vibration, and translation. Of these the first two are solved analytically while the third is solved numerically using finite element method. The latter is implemented with PETSc® and SLEPc® software libraries [78-81]. This method is also used to obtain numerical solutions for the diffusivities. The grid mesh that describes the nodes and elements of the system is generated using the Gmsh® software. The interactions between the oxygen molecule and the tin atoms are described by using the Lennard-Jones-Devonshire Potential [82]. Periodic boundary conditions are applied to ensure that the oxygen moves in one direction. A parallel MATLAB® code has been written based on SPMD (single program multiple date) to obtain the stiffness and mass matrices for the finite element method, and a parallel c-code is developed and used to solve for the energy eigenvalues and eigenfunctions by means of the PETSc® and SLEPc® softwares. PETSc® is used to read the matrcies, and SLEPc® is used to solve large-scale problems for eigenvalues and eigenfunctions. All the calculations are done by using the built-in functions of MATLAB® 2014b, and all large scale problems are solved on the Ithaca and BlueRidge supercomputers which are the large-scale research computing systems at the Virginia Tech.

4.1.1 System Description

The system of interest modeled here is an open system oxygen (O_2) diffusion through a tin (S_n) anode as shown in Figure 4.1. This system can be defined as a three-dimensional box of size

of 10 nm x 3 nm x 3 nm in the $x, y,$ and z directions, respectively. Note that it is assumed that the diffusion occurs only in the longitudinal direction, i.e., in the x direction, between 0 and L_x. In other words, the oxygen molecule O_2 enters the system at $x = 0$ and leaves at $x = L_x$. Motion in the transverse directions, i.e., y and z directions is not considered. Note that the oxygen molecule interacts with the tin atoms. Also, the energy modes considered for the oxygen molecule are translational, vibrational, and rotational.

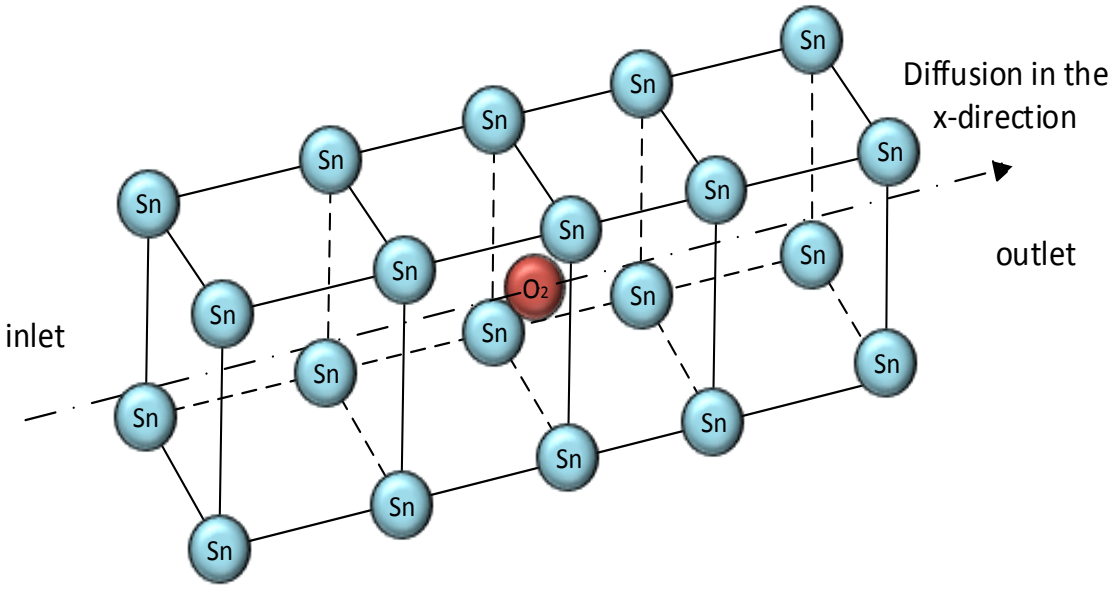

Figure 4.1. Schematic of an open system of oxygen diffusion through a tin anode.

4.1.2 Energy Eigenstructure of a Single Particle

The set of energy eigenvalues for a diatomic molecule such as O_2 is a combination of the separable translational, vibrational, and rotational energy modes. The translational eigenvalues are considered as an external mode, while the vibrational and rotational eigenvalues are treated as internal modes. The total energy eigenvalue for a diatomic molecule is, this, written as

$$e_{tot} = e_{tr} + e_{vib} + e_{rot} \tag{4.1}$$

where e_{tr}, e_{vib}, and e_{rot} stand for the translational, vibrational, and rotational energy eigenvalues, respectively.

4.1.2.1 Translational Energy Eigenvalue Problem

The translational energy eigenvalue appropriate to the system at hand is given by

$$\frac{-\hbar^2}{2\,m_{o_2}}\left(\frac{\partial^2\psi(\vec{r})}{\partial x^2}+\frac{\partial^2\psi(\vec{r})}{\partial y^2}+\frac{\partial^2\psi(\vec{r})}{\partial z^2}\right)+\ V(\vec{r})\ \psi(\vec{r})\ =\ e_{tr}\ \psi(\vec{r}) \tag{4.2}$$

Here, $\psi(\vec{r})$ is the eigenfunction, $\vec{r}$ is the position vector as a function of $x, y,$ and z, m_{o_2} is the mass of the oxygen molecule[16] O_2, and $V(\vec{r})$ is the potential energy that describes the interactions between the oxygen molecule and the tin atoms, i.e., the $O_2 - S_n$ interactions. These interactions are captured by the Lennard-Jones-Devonshire Potential [82-85]. Equation (4.2) is solved numerically by using finite element analysis with a structured grid.

4.1.2.2 Rotational and Vibrational Energy Eigenvalue Problems

Modeling the rotational energy mode of the oxygen molecule as a rigid rotor [10, 50, 86] as shown in Figure 4.2, the rotational energy eigenvalues are expressed as

$$e_{rot}=\frac{\hbar^2}{2\,m_r\,d^2}\,k_J\left(k_J+1\right),\quad n_J=0,1,2,\ldots \tag{4.3}$$

where k_J is the rotational quantum number, d is the distance between the centers of the two oxygen atoms in the oxygen molecule ($d = 1.208x10^{-8}$ cm), and m_r is the reduced mass which is for oxygen molecule is written as

$$m_r=\frac{1}{2}\,m_{o_2} \tag{4.4}$$

If the vibrational energy mode of the oxygen molecule is modeled as a harmonic oscillator [10, 50, 86] as shown in Figure 4.3, the vibrational energy eigenvalues are

$$e_{vib}=h\,c\,\omega_e\,\left(k_v+\frac{1}{2}\right),\quad n_v=0,1,2,\ldots \tag{4.5}$$

Here k_v is the vibrational quantum number, ω_e is the vibrational wave number ($\omega_e = 1580.19$ cm^{-1}), h is the Planck's constant, and c is the speed of the light ($c = 3x10^{10}$ cm/s).

[16] $m_{o_2} = 2.65676X10^{-26}\ kg$

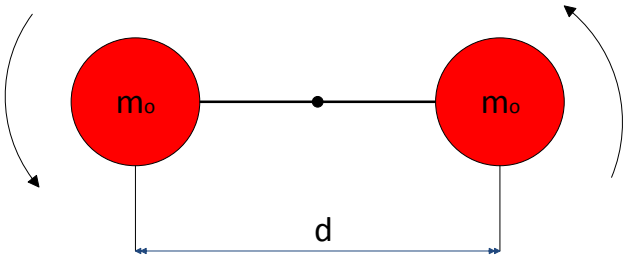

Figure 4.2. The oxygen molecule as rigid rotator.

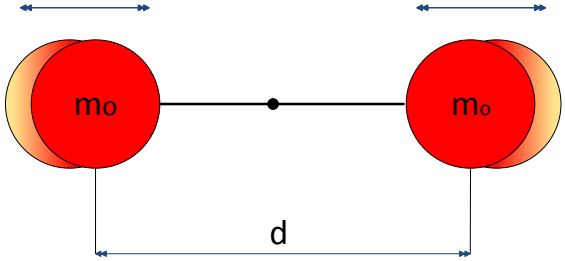

Figure 4.3. The oxygen molecule as harmonic oscillator.

4.1.3 SEAQT Equation of Motion with Two Mass Interactions

In terms of an open system, i.e., oxygen diffusion through a tin anode, the SEAQT equation of motion, equation (3.15), is extended to capture not only the dissipation process going on inside the system but also the mass interactions with the mass reservoirs at the inlet and outlet of the system. This extended equation is developed based on the rotated phenomenological mass interaction (RPMI) developed and described in [57], and is given by

$$\frac{d\rho}{dt} = \frac{-i}{\hbar}[H,\rho] + \frac{1}{2k_b\,\tau_D}\{\Delta M,\rho\} + \frac{1}{2k_b\,\tau_{G_1}}\{\Delta G_1,\rho\} - \frac{1}{2k_b\,\tau_{G_2}}\{\Delta G_2,\rho\} \qquad (4.6)$$

The first term to the right of the equals is the time-independent Schrödinger term that vanishes when H and ρ commute which they do for the case considered here. The second term is the dissipation operator of the system written in the operator notation used in [57]. The third and

fourth terms are the RPMI operators that model the mass interactions between the system and mass reservoirs at the inlet and outlet, respectively. τ_D, τ_{G_1}, and τ_{G_2} are the relaxation times that play an important role in scaling and adjusting the relative strengths of each of the operators, i.e., the dissipation and the mass interactions. Subscripts 1 and 2 stand for the inlet and outlet, respectively. The anti-commutator operators $\{\,.\,\}$ in equation (4.6) are defined as

$$\{\Delta M, \rho\} = \Delta M\, \rho + \rho\, \Delta M \tag{4.7}$$

$$\{\Delta G_i, \rho\} = \Delta G_i\, \rho + \rho\, \Delta G_i\,, i = 1,2 \tag{4.8}$$

where M is the non-equilibrium Massieu dissipation operator [49, 57] expressed as

$$M = S - \frac{h_H}{(h_H - h_N)}\left(\frac{1}{\theta_H} - \frac{S_N}{h_H}\right) H + \frac{h_H}{(h_H - h_N)}\left(\frac{h_N}{\theta_H} - S_N\right) N \tag{4.9}$$

Here H, S and N are the Hamiltonian, entropy and particle number operators, respectively. The deviation operator of M, i.e., ΔM, is

$$\Delta M = \Delta S - \frac{h_H}{(h_H - h_N)}\left(\frac{1}{\theta_H} - \frac{S_N}{h_H}\right) \Delta H + \frac{h_H}{(h_H - h_N)}\left(\frac{h_N}{\theta_H} - S_N\right) \Delta N \tag{4.10}$$

The non-equilibrium enthalpies h_H and h_N are defined by

$$h_H = \frac{\langle \Delta H \Delta H \rangle}{\langle \Delta H \Delta N \rangle} \tag{4.11}$$

$$h_N = \frac{\langle \Delta H \Delta N \rangle}{\langle \Delta N \Delta N \rangle} \tag{4.12}$$

while the constant-energy non-equilibrium temperature θ_H and the non-equilibrium parameter S_N are written as a ratio of the expectation values of the products of the deviation operators of the H, S and N, i.e., the so-called covariance parameters, such that

$$\theta_H = \frac{\langle \Delta H \Delta H \rangle}{\langle \Delta H \Delta S \rangle} \tag{4.13}$$

$$S_N = \frac{\langle \Delta S \Delta N \rangle}{\langle \Delta N \Delta N \rangle} \tag{4.14}$$

The covariance parameters are then given as

$$\langle \Delta H \Delta H \rangle = \mathrm{Tr}(\rho(\Delta H)^2) = \mathrm{Tr}(\rho H^2) - \big(\mathrm{Tr}(\rho H)\big)^2 \tag{4.15}$$

$$\langle \Delta N \Delta N \rangle = \mathrm{Tr}(\rho(\Delta N)^2) = \mathrm{Tr}(\rho N^2) - \big(\mathrm{Tr}(\rho N)\big)^2 \tag{4.16}$$

$$\langle \Delta H \Delta S \rangle = \mathrm{Tr}\big(\rho\ (\Delta H \Delta S)\big) = \mathrm{Tr}(\rho HS) - \mathrm{Tr}(\rho H) Tr(\rho S) \tag{4.17}$$

$$\langle \Delta S \Delta N \rangle = \mathrm{Tr}\big(\rho\ (\Delta S \Delta N)\big) = \mathrm{Tr}(\rho SN) - \mathrm{Tr}(\rho S)\ \mathrm{Tr}(\rho N) \tag{4.18}$$

where the variance for the operators of H, S, and N are defined to be

$$\Delta H = H - \langle H \rangle\ I \tag{4.19}$$

$$\Delta S = S - \langle S \rangle\ I \tag{4.20}$$

$$\Delta N = N - \langle N \rangle\ I \tag{4.21}$$

with the expectation values expressed as

$$\langle H \rangle = \mathrm{Tr}(\rho\ H) \tag{4.22}$$

$$\langle S \rangle = -\ k_b \mathrm{Tr}(\rho\ \ln \rho) \tag{4.23}$$

$$\langle N \rangle = \mathrm{Tr}(\rho\ n_p) \tag{4.24}$$

Note that $\mathrm{Tr}(\ldots)$ stands for the trace of the matrix and is performed by summing over the diagonal. The non-equilibrium Massieu mass-interaction operators $G_i, i = 1, 2$ [49, 57] are based on the RPMI and are written as

$$\begin{aligned} G_i = \tilde{S} - \frac{h_{H_{rot}}}{\left(h_{H_{rot}} - h_{N_{rot}}\right)}\left(\frac{1}{\theta_{H_{rot}}} - \frac{S_{N_{rot}}}{h_{H_{rot}}}\right)\widetilde{H} \\ + \frac{h_{H_{rot}}}{\left(h_{H_{rot}} - h_{N_{rot}}\right)}\left(\frac{h_{N_{rot}}}{\theta_{H_{rot}}} - S_{N_{rot}}\right)\widetilde{N} \end{aligned} \tag{4.25}$$

The deviation operator of $G_i, i = 1, 2$ is then given by

$$\begin{aligned} \Delta G_i = \Delta\tilde{S} - \frac{h_{H_{rot}}}{\left(h_{H_{rot}} - h_{N_{rot}}\right)}\left(\frac{1}{\theta_{H_{rot}}} - \frac{S_{N_{rot}}}{h_{H_{rot}}}\right)\Delta\widetilde{H} \\ + \frac{h_{H_{rot}}}{\left(h_{H_{rot}} - h_{N_{rot}}\right)}\left(\frac{h_{N_{rot}}}{\theta_{H_{rot}}} - S_{N_{rot}}\right)\Delta\widetilde{N} \end{aligned} \tag{4.26}$$

where the non-equilibrium enthalpies appearing in this last expression are

$$h_{H_{rot}} = \frac{\langle \Delta H \Delta H \rangle_{rot}}{\langle \Delta H \Delta N \rangle_{rot}} \tag{4.27}$$

$$h_{N_{rot}} = \frac{\langle \Delta H \Delta N \rangle_{rot}}{\langle \Delta N \Delta N \rangle_{rot}} \tag{4.28}$$

and the constant-energy non-equilibrium temperature $\theta_{H_{rot}}$ and the non-equilibrium parameter $S_{N_{rot}}$ are given by

$$\theta_{H_{rot}} = \frac{\langle \Delta H \Delta H \rangle_{rot}}{\langle \Delta H \Delta S \rangle_{rot}} \tag{4.29}$$

$$S_{N_{rot}} = \frac{\langle \Delta S \Delta N \rangle_{rot}}{\langle \Delta N \Delta N \rangle_{rot}} \tag{4.30}$$

Here the subscript rot stands for rotated coordinates. The rotated covariances appearing in equations (4.27) to (4.30) are written as

$$\langle \Delta H \Delta H \rangle_{rot} = \mathrm{Tr}\left(\rho \widetilde{H}^2\right) - \left(\mathrm{Tr}\left(\rho \widetilde{H}\right)\right)^2 \tag{4.31}$$

$$\langle \Delta N \Delta N \rangle = \mathrm{Tr}\left(\rho \widetilde{N}^2\right) - \left(\mathrm{Tr}\left(\rho \widetilde{N}\right)\right)^2 \tag{4.32}$$

$$\langle \Delta H \Delta S \rangle = \mathrm{Tr}\left(\rho\, \widetilde{H}\tilde{S}\right) - \mathrm{Tr}\left(\rho\, \widetilde{H}\right)\mathrm{Tr}\left(\rho\, \tilde{S}\right) \tag{4.33}$$

$$\langle \Delta S \Delta N \rangle = \mathrm{Tr}\left(\rho\, \tilde{S}\widetilde{N}\right) - \mathrm{Tr}\left(\rho\, \tilde{S}\right)\mathrm{Tr}\left(\rho\, \widetilde{N}\right) \tag{4.34}$$

In these last equations, $\widetilde{H}, \tilde{S},$ and $\widetilde{N}$ operators are obtained by rotating the original H, S, and N operators twice in the $H - S - N$ space. The first is a counter-clockwise rotation of the $H - S$ plane through the angle θ about the N axis such that

$$\tilde{S} = S\ \cos(\theta) - H\ \sin(\theta) \tag{4.35}$$

$$\tilde{H} = S\ \sin(\theta) + H\ \cos(\theta) \tag{4.36}$$

$$\tilde{N} = N \tag{4.37}$$

The second is a counter-clockwise rotation of the $S - N$ plane through the angle $\emptyset$ about the $\tilde{H}$ axis with the result that

$$\tilde{\tilde{S}} = \tilde{S}\ \cos(\emptyset) - \tilde{N}\ \sin(\emptyset) \tag{4.38}$$

$$\tilde{\tilde{H}} = \tilde{H} \tag{4.39}$$

$$\tilde{\tilde{N}} = \tilde{S}\ \sin(\emptyset) + \tilde{N}\ \cos(\emptyset) \tag{4.40}$$

Here, the $\tilde{H}$, $\tilde{S}$, and $\tilde{N}$ operators are obtained by rotating the original H, S, and N operators, and the $\tilde{\tilde{H}}$, $\tilde{\tilde{S}}$, and $\tilde{\tilde{N}}$ operators are obtained by rotating the rotated $\tilde{H}$, $\tilde{S}$, and $\tilde{N}$ operators. The sin and cos of the angles θ and $\emptyset$ are given by

$$\cos(\theta) = \frac{\langle S_{eq}\rangle - \langle S\rangle}{\sqrt{\left(\langle S_{eq}\rangle - \langle S\rangle\right)^2 + \left(\langle H_{eq}\rangle - \langle H\rangle\right)^2}} \tag{4.41}$$

$$\sin(\theta) = \frac{\langle H_{eq}\rangle - \langle H\rangle}{\sqrt{\left(\langle S_{eq}\rangle - \langle S\rangle\right)^2 + \left(\langle H_{eq}\rangle - \langle H\rangle\right)^2}} \tag{4.42}$$

$$\cos(\emptyset) = \frac{\sqrt{\left(\langle S_{eq}\rangle - \langle S\rangle\right)^2 + \left(\langle H_{eq}\rangle - \langle H\rangle\right)^2}}{\sqrt{\left(\langle S_{eq}\rangle - \langle S\rangle\right)^2 + \left(\langle H_{eq}\rangle - \langle H\rangle\right)^2\left(\langle N_{eq}\rangle - \langle N\rangle\right)^2}} \tag{4.43}$$

$$\sin(\emptyset) = \frac{\langle N_{eq}\rangle - \langle N\rangle}{\sqrt{\left(\langle S_{eq}\rangle - \langle S\rangle\right)^2 + \left(\langle H_{eq}\rangle - \langle H\rangle\right)^2\left(\langle N_{eq}\rangle - \langle N\rangle\right)^2}} \tag{4.44}$$

Note that H_{eq}, S_{eq}, and N_{eq} are determined at stable equilibrium. The numerical solution of the SEAQT equation of motion is described in the *Section* 4.2.1.

4.1.4 Non-equilibrium-based Density Distribution

The non-equilibrium-based density distribution of particles is obtained from combining the density operator and the eigenfunctions of the system as mentioned in *Section* 3.1.4. In case of an open system, the density operator is obtained from solving the SEAQT equation of motion with two mass interactions, equation (4.6), and the eigenfunctions of the system are obtained from the numerical solution of the translational energy eigenvalue problem, equation (4.2). The non-equilibrium-based density distribution of particles is written as follows:

$$n_{neq}(\vec{r},t) = \sum_i \rho_i(t)\ |\psi_i(\vec{r})|^2 \tag{4.45}$$

where $i = 1,2,\dots,\mathcal{N}$ and $\mathcal{N}$ is the number of energy eigenlevels for the system. Note that it is assumed here to good approximation that the internal mode eigenfunctions for rotation and vibration contribute little to this density distribution of particles.

4.1.5 Diffusivity of the Open System

In order to derive the steady state and transient diffusivities of an open system, the mass flux, equation (1.4), is modified by using a first order Taylor series expansion of the distribution function $\bar{f}(x,t)$, such that

$$\bar{f}(x,t) = f(x,t) + \frac{\partial f(x,t)}{\partial x}\,\Delta x + \frac{\partial f(x,t)}{\partial t}\Delta t \tag{4.46}$$

where Δx and Δt are given by

$$\Delta x = \Delta t\, v_x \text{ and } \Delta t = \tau \tag{4.47}$$

Substituting the equations (4.46) and (4.47) into equation (1.4), the mass flux is rewritten as follows:

$$J_x = -\sum_i \left(\tau\, v_{x_i}^2 \frac{\partial f_i(x,t)}{\partial x} + \tau\, v_{x_i} \frac{\partial f_i(x,t)}{\partial t}\right) \tag{4.48}$$

Here v_{x_i} is the particle velocity in the x direction, and is not a function of position or time. Note that the advection term, $v_x f(x,t)$, is dropped in order to capture only the diffusive effects. Multiplying and dividing the last expression by the derivative with respect to x of the density distribution of particles, dn/dx, yields

$$J_x = -\left(\frac{\sum_i \left(\tau\, v_{x_i}^2 \frac{\partial f_i(x,t)}{\partial x}\right)}{\frac{dn}{dx}} + \frac{\sum_i \left(\tau\, v_{x_i} \frac{\partial f_i(x,t)}{\partial t}\right)}{\frac{dn}{dx}}\right)\frac{dn}{dx} \tag{4.49}$$

The latter equation reduces to

$$J_x = -D\,\frac{dn}{dx} \tag{4.50}$$

D is the diffusivity and consists of D_{ss} and D_{tr} which are the steady state and transient diffusivities, respectively. D_{ss} and D_{tr} are given by

$$D_{ss} = \frac{\sum_i \left(\tau \, v_{x_i}^2 \frac{\partial f_i(x,t_{ss})}{\partial x}\right)}{\sum_i \left(\frac{\partial f_i(x,t)}{\partial x}\right)} \tag{4.51}$$

$$D_{tr} = \frac{\sum_i \left(\tau \, v_{x_i}^2 \frac{\partial f_i(x,t)}{\partial x}\right)}{\sum_i \left(\frac{\partial f_i(x,t)}{\partial x}\right)} + \frac{\sum_i \left(\tau \, v_{x_i} \frac{\partial f_i(x,t)}{\partial t}\right)}{\sum_i \left(\frac{\partial f_i(x,t)}{\partial x}\right)} \tag{4.52}$$

Here τ is the relaxation time and is equal to (l_g/v). l_g is the mean free path, and v is the total velocity. v_x and v are obtained from the kinetic energy as follows

$$e_{tot} = \frac{1}{2} m_{o_2} v^2 \Longrightarrow v = \left(\frac{2}{m_{o_2}} \, e_{tot}\right)^{\frac{1}{2}} \tag{4.53}$$

$$e_x = \frac{1}{2} m_{o_2} v_x^2 \Longrightarrow v_x^2 = \frac{2}{m_{o_2}} \, e_x \tag{4.54}$$

Here e_{tot} and e_x stand for the total energy eigenvalue, and the energy eigenvalue in x direction, respectively. Note that e_{tot} and e_x have numerical values obtained from solving the eigenvalue problem numerically. Substituting $\rho(t)$, $\psi(\vec{r})$, τ, v, and v_x into equations (4.51) and (4.52), the steady state diffusivity D_{ss} and the transient diffusivity D_{tr} are given by

$$D_{ss} = l_g \left(\sqrt{\frac{2}{m_{o_2}}}\right) \left(\frac{\sum_i \left(\frac{e_{x_i}}{\sqrt{e_{tot_i}}} \rho_i(t_{ss}) \psi_i(\vec{r}) \, \frac{\partial}{\partial x} \psi_i(\vec{r}) \right)}{\sum_i \left(\rho_i(t_{ss}) \psi_i(\vec{r}) \, \frac{\partial}{\partial x} \psi_i(\vec{r}) \right)} \right) \tag{4.55}$$

$$D_{tr} = l_g \left(\sqrt{\frac{2}{m_{o_2}}}\right) D_1 + \frac{l_g}{2} D_2 \tag{4.56}$$

Where

$$D_1 = \left(\frac{\sum_i \left(\frac{e_{x_i}}{\sqrt{e_{tot_i}}} \rho_i(t)\, \psi_i(\vec{r})\, \frac{\partial}{\partial x} \psi_i(\vec{r}) \right)}{\sum_i \left(\rho_i(t)\, \psi_i(\vec{r})\, \frac{\partial}{\partial x} \psi_i(\vec{r}) \right)} \right) \tag{4.57}$$

$$D_2 = \left(\frac{\sum_i \left(\sqrt{\frac{e_{x_i}}{e_{tot_i}}}\, |\psi_i(\vec{r})|^2 \frac{\partial}{\partial t} \rho_i(t) \right)}{\sum_i \left(\rho_i(t)\, \psi_i(\vec{r})\, \frac{\partial}{\partial x} \psi_i(\vec{r}) \right)} \right) \tag{4.58}$$

Here $\rho(t)$ and $\psi(\vec{r})$ are the density operator and eigenfunctions of the system. Note that the unit of the steady state and transient diffusivities is length squared per time.

4.2 Numerical Approach

4.2.1 Solving SEAQT Equation of Motion with Two Mass Interactions

For the case of an open system, the number of particles in the system is no longer a constant but instead an expectation values. That leads to the use of the grand canonical instead of the canonical distribution in the generation of an initial state for the SEAQT equation of motion. In fact two types are required, one at stable equilibrium and a set of partial equilibrium. The former, $\rho_g^{se}(E)$ [35, 42, 87], for a given value of the system energy E is given by

$$\rho_{g_j}^{se}(E) = \frac{\exp\left(\alpha^{se}(E)\, n_{p_j} - \beta^{se}(E)\, e_j\right)}{\sum_{i=1}^{\mathcal{N}} \exp\left(\alpha^{se}(E)\, n_{p_i} - \beta^{se}(E)\, e_i\right)} \tag{4.59}$$

where e_i is the i^{th} energy eigenvalue of the system, and n_{p_i} is the eigenvalue of the number of particles that have energy eigenvalue e_i. α^{se} and β^{se} are parameters defined by temperature, T, and chemical potential, μ, at stable equilibrium, i.e.,

$$\alpha^{se}(E) = \frac{\mu}{k_b\, T(E)}, \quad \beta^{se}(E) = \frac{1}{k_b\, T(E)} \tag{4.60}$$

As to the partially grand canonical equilibrium distribution $\rho_g^{pe}(E,\boldsymbol{\delta})$ for the same given value of the system energy E, it is expressed as

$$\rho_{g_j}^{pe}(E,\boldsymbol{\delta}) = \frac{\exp\left(\alpha^{pe}(E,\boldsymbol{\delta})\, n_{p_j} - \beta^{pe}(E,\boldsymbol{\delta})\, e_j\right)}{\sum_{i=1}^{\mathcal{N}} \exp\left(\alpha^{pe}(E,\boldsymbol{\delta})\, n_{p_i} - \beta^{pe}(E,\boldsymbol{\delta})\, e_i\right)} \tag{4.61}$$

As before $\boldsymbol{\delta}$ is a time-invariant vector as described in equation (3.70). The superscripts "se" and "pe" stand for stable equilibrium state and partial (unstable) equilibrium state, respectively.

The values for $\alpha^{pe}(E,\boldsymbol{\delta})$, $\beta^{pe}(E,\boldsymbol{\delta})$ and a given set of ρ_g^{pe} for a fixed $\boldsymbol{\delta}$ are computed by solving the system of equations formed by equation (4.61) and the following two equations:

$$\sum_{i=1}^{\mathcal{N}} \rho_{g_i}^{pe}(E,\boldsymbol{\delta})\, e = \langle E \rangle \tag{4.62}$$

$$\sum_{i=1}^{\mathcal{N}} \rho_{g_i}^{pe}(E,\boldsymbol{\delta})\, n_{p_i} = \langle N \rangle \tag{4.63}$$

$\langle E \rangle$ and $\langle N \rangle$ are the initial expectation values of the energy and the number of particles in the system, respectively. To obtain the initial non-equilibrium density operator, the thermodynamic-equilibrium grand canonical distribution $\rho_g^{se}(E)$ is perturbed as described in *Section* 3.2.1 of *Chapter* 3.

4.2.2 Solving the Large-Scale Non-symmetric Translational Energy Eigenvalue Problem

The translational energy eigenvalue problem, in equation (4.2), is solved numerically using Finite Element Analysis (FEA) to obtain the energy eigenvalues e_{tr} and eigenfunctions $\psi(\vec{r})$ [88-92]. The finite element approximate solution for $\psi(\vec{r})$ is given in the form

$$\psi(\vec{r}) = \sum_{i=1}^{n_d} u_i\ \Phi_i(\vec{r}) \tag{4.64}$$

The u_i are the numerical solutions of $\psi(\vec{r})$, and the $\Phi_i(\vec{r})$ are the approximation functions (shape functions), and n_d is the number of nodes per element. The numerical solution u_i is based on the weak form derived directly by multiplying equation (4.2) by a weight function $w(\vec{r})$, and integrating over the domain Ω such that

$$\int_\Omega \left(\frac{\hbar^2}{2\, m_{o_2}} \left(\frac{\partial w}{\partial x}\frac{\partial \psi}{\partial x} + \frac{\partial w}{\partial y}\frac{\partial \psi}{\partial y} + \frac{\partial w}{\partial z}\frac{\partial \psi}{\partial z} \right) + V w\, \psi \right) d\Omega = \int_\Omega e_{tr} w\, \psi\, d\Omega \tag{4.65}$$

Using the Galerkin method, $w(\vec{r}) = \Phi_i(\vec{r})$, and substituting the approximate solution into equation (4.65) leads to

$$\sum_{i,j}\left(\int_{\Omega}\left(\frac{\hbar^2}{2\,m_{o_2}}\left(\frac{\partial\Phi_j}{\partial x}\frac{\partial\Phi_i}{\partial x}+\frac{\partial\Phi_j}{\partial y}\frac{\partial\Phi_i}{\partial y}+\frac{\partial\Phi_j}{\partial z}\frac{\partial\Phi_i}{\partial z}\right)+\ V\,\Phi_j\Phi_i\ \right)d\Omega\right)u_i = e_{tr}\sum_{i,j}\left(\int_{\Omega}\Phi_j\,\Phi_i\,d\Omega\right)u_i \tag{4.66}$$

In equation (4.65) and (4.66), V is the potential function obtained via the Lennard-Jones-Devonshire potential. The finite element model of the eigenvalue problem is then written in matrix form as

$$[K]\{u_i\} = e_{tr}[M]\{u_i\} \tag{4.67}$$

In this equation, K is the stiffness matrix, and M is the mass matrix. The entries of these matrices are given by

$$K_{ij} = \int_{\Omega}\left(\frac{\hbar^2}{2\,m_{o_2}}\left(\frac{\partial\Phi_i}{\partial x}\frac{\partial\Phi_j}{\partial x}+\frac{\partial\Phi_i}{\partial y}\frac{\partial\Phi_j}{\partial y}+\frac{\partial\Phi_i}{\partial z}\frac{\partial\Phi_j}{\partial z}\right)+\ V\,\Phi_i\,\Phi_j\ \right)d\Omega \tag{4.68}$$

$$M_{ij} = \int_{\Omega}\Phi_i\,\Phi_j\ d\Omega \tag{4.69}$$

These integrals are solved numerically using Gauss-Legendre quadrature [88, 90].

4.2.2.1 The Tin Structure and the Lennard-Jones-Devonshire Potential

It is assumed that the tin has structure of white tin ($\beta - S_n$) which is a body-centered tetrahedral structure (bct) [93-98]. The unit cell of tin is shown in Figure 4.4, and the lattice parameters are $a = 5.831$ Å and $c = 3.182$ Å [98, 99]. The structure of the tin becomes closely packed [93, 98], and the atoms come closer to each other. In this case the tin is considered to be a dense gas. For the system structure here, and oxygen molecule is allowed to move within a unit cell whose boundaries are described by the positions of the nearest neighbors, and interacts with all the nearest tin neighbors as shown in Figures 4.6 to 4.8. Note that the repeated cell tin lattice structure in the system is not symmetric as seen in Figure 4.5 in the $x - z$ plane. In this figure, the white balls represent tin atoms that are outside the box and do not interact with oxygen

molecule. That leads to that the lowest concertation of tin atoms is at $x = 10\ nm$ and at $z = 3\ nm$.

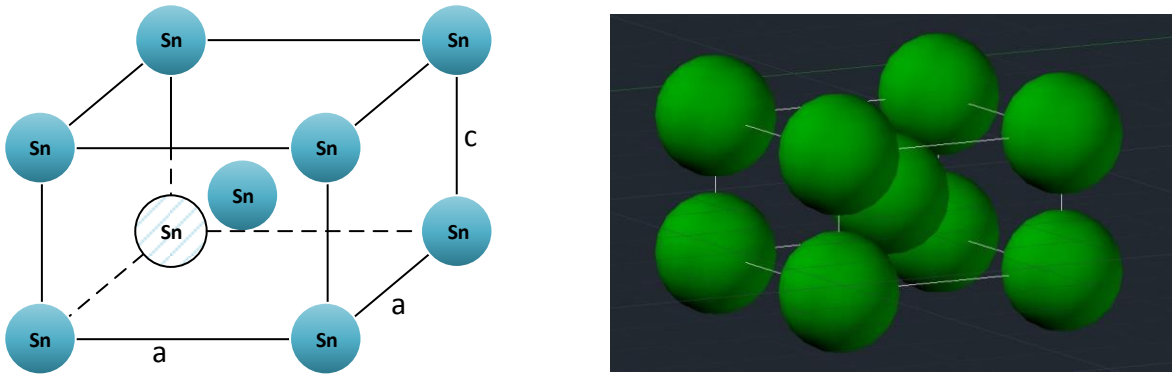

(a) (b)

Figure 4.4. Schematic for (a) the tin unit cell and (b) Tin cell lattice structure (tin atoms are pictured as green balls). AutoCAD® 2014 drawing.

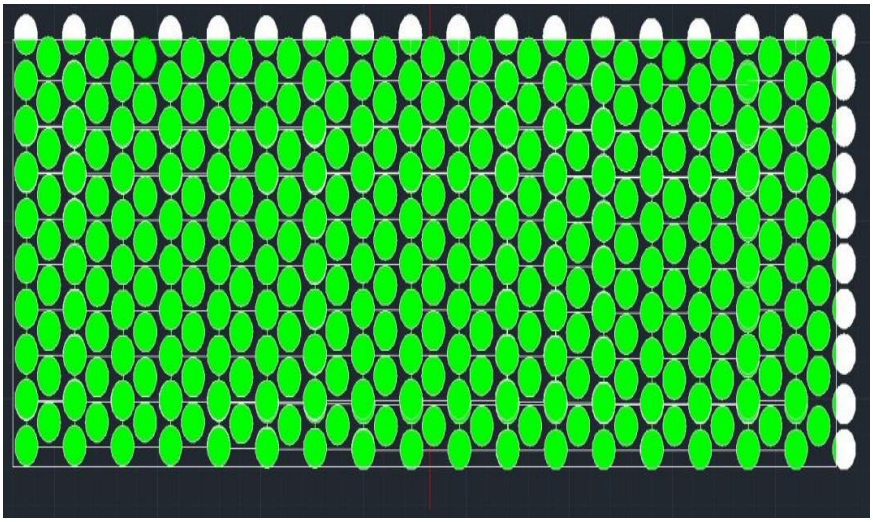

Figure 4.5. Schematic diagram of repeated cell tin lattice in the $x - z$ plane (tin atoms pictured green balls).

In order to calculate the potential of interaction between the oxygen molecule and the nearest neighbor tin atoms, the Lennard-Jones-Devonshire theory [82-85, 100-104] is used. In this theory, it is assumed that the central particle, which is for the case considered here oxygen molecule, interacts with a number of atoms, which in this case are tin atoms, uniformly

distributed over a surface of a sphere whose radius is r from the center of the sphere as depicted in Figure 4.9. This center coincides with the center of a unit cell.

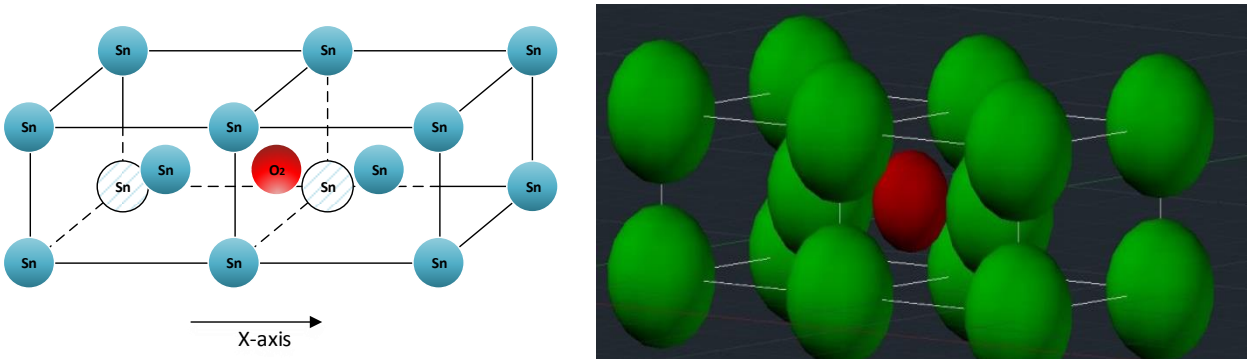

(a) (b)

Figure 4.6. Schematic description for (a) an oxygen molecule moving through unit cells of tin atoms and (b) location of oxygen molecule (pictured as red ball) inside tin cell lattice (tin atoms are pictured as green balls). AutoCAD® 2014 drawing.

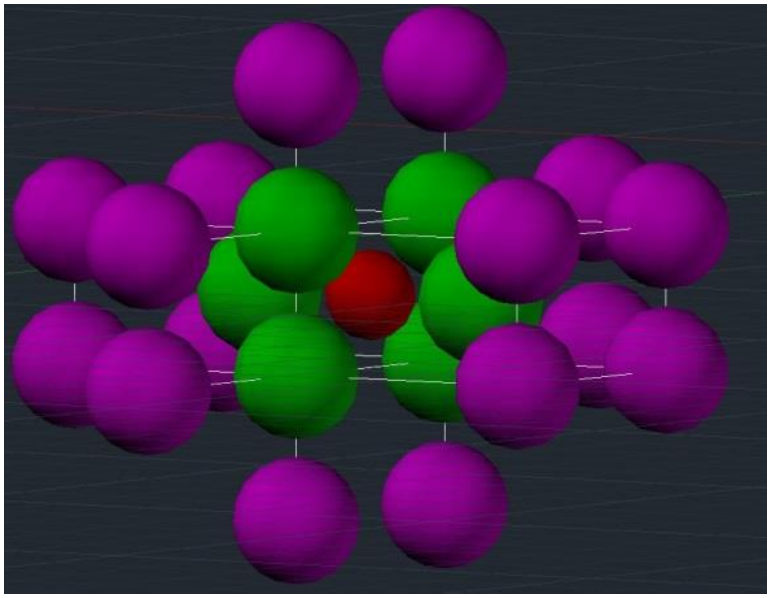

Figure 4.7. Schematic description of oxygen molecule (pictured as red ball) interacts with the first (pictured as green balls) and second (pictured as magenta balls) tier nearest neighbors. AutoCAD® 2014 drawing.

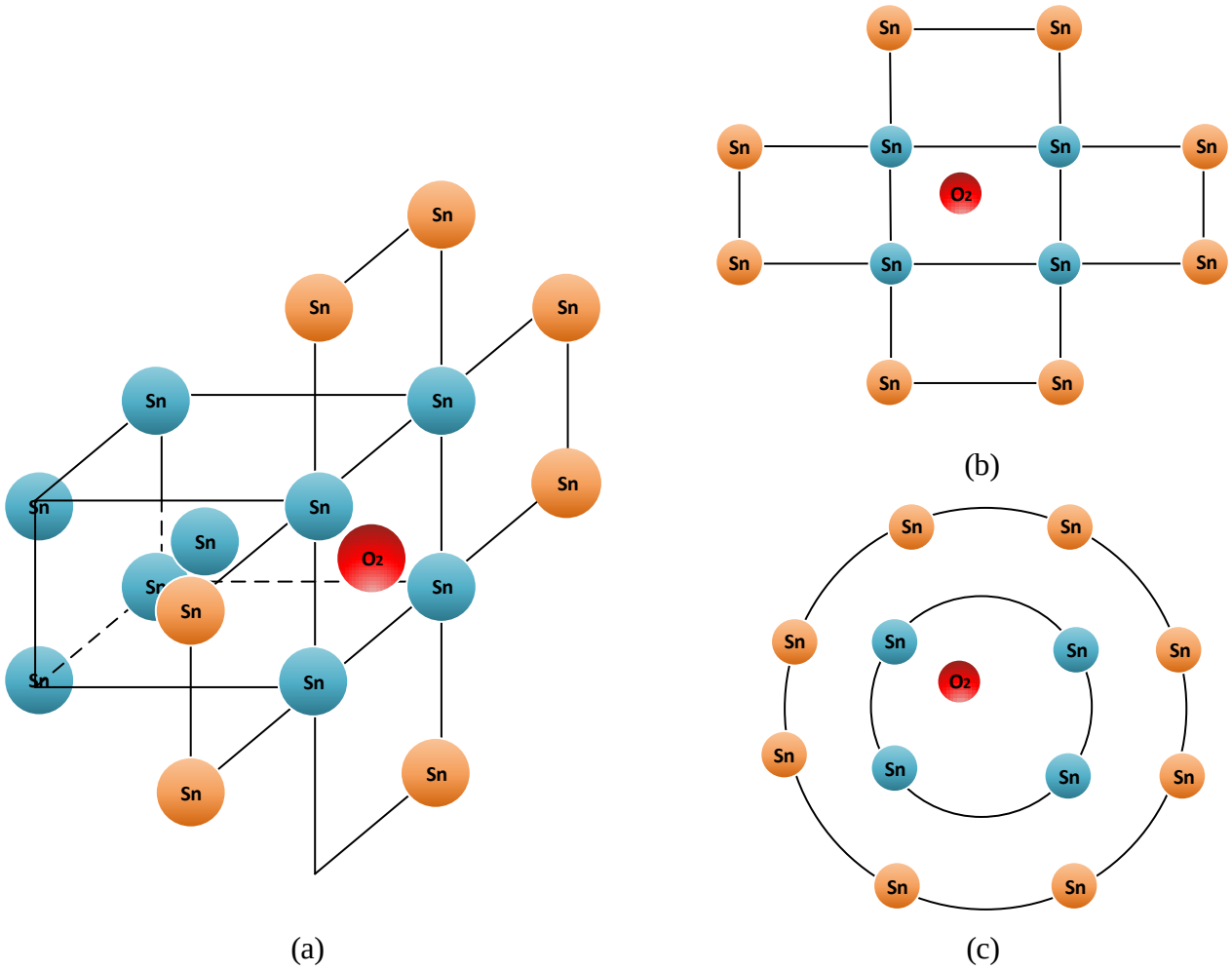

Figure 4.8. (a) Schematic description of oxygen molecule (red ball) interacts with the first (blue balls) and second (orange balls) tier nearest neighbors; (b) two-dimensional representation of oxygen molecule (red ball) surrounded by the first tier nearest neighbors (blue balls) and the second tier nearest neighbors (orange balls); and (c) two-dimensional cut of the Leonard-Jones-Devonshire sphere of influence to demonstrate the distribution of tin atoms over and above the surface of the sphere of the first and second tier nearest neighbors.

In the first figure, the oxygen molecule is at position P a distance a from the center of the cell (or sphere) which is the origin o. In Figure 4.9, the area of the ring on the surface is [85, 105]

$$A_{arc} = 2\pi r^2 \sin(\theta)\ d\theta \tag{4.70}$$

The number of the nearest neighbor particles that distribute in this area is given by dividing equation (4.70) by the area of the sphere and multiplying by the number of the nearest neighbors, $\mathcal{C}$, such that

$$\frac{\mathcal{C}\ A_{arc}}{A_{sphere}} = \mathcal{C}\frac{2\pi r^2 \sin(\theta)\ d\theta}{4\pi r^2} = \frac{\mathcal{C}}{2}\sin(\theta)\ d\theta \tag{4.71}$$

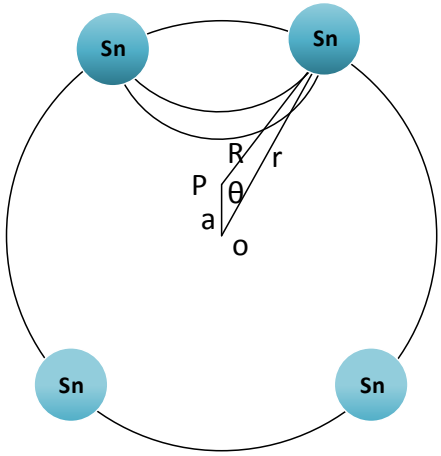

Figure 4.9. Two-dimensional description of the distribution of the first nearest neighbors of a unit cell of tin over a sphere of influence of radius r [85, 105].

The potential energy of the interaction between oxygen at position P and the nearest neighbor particles in the ring is given by multiply equation (4.71) by the pairwise potential energy of interaction between the oxygen molecule and one tin atom $U(R)$, .i.e.,

$$V(r) = U(R)\ \frac{\mathcal{C}}{2}\sin(\theta)\ d\theta \tag{4.72}$$

Finally, the potential energy $V(r)$ that describes the interaction between the oxygen molecule and tin atoms on the surface of the sphere reduces to the following single integral

$$V(r) = \frac{\mathcal{C}}{2}\int_0^{\pi} (U(R)\sin(\theta))\, d\theta \tag{4.73}$$

In this equation $\mathcal{C}$ is the number of the nearest neighbors, and $U(R)$ is the pairwise potential energy of interaction between the oxygen molecule and one tin atom. It is defined by the Lennard-Jones potential [9, 106-108] such that

$$U(R) = 4\epsilon\left(\left(\frac{\sigma}{R}\right)^{12} - \left(\frac{\sigma}{R}\right)^{6}\right) \tag{4.74}$$

where R is the distance between the oxygen molecule and the tin atom on the surface of the sphere and is obtained from the law of cosines expressed as

$$R = r^2 + a^2 - 2\,a\,r\cos(\theta) \tag{4.75}$$

The ϵ and σ are Lennard-Jones parameters [108, 109], which for two different species interacting particles 1 and 2, are given by

$$\epsilon_{12} = \sqrt{\epsilon_1 \epsilon_2} \quad \sigma_{12} = \frac{\sigma_1 + \sigma_2}{2} \tag{4.76}$$

Substituting the equations (4.74) and (4.75) into (4.73) and integrating form 0 to π, the potential energy $V(r)$ becomes

$$V(r) = \frac{\mathcal{C}\,\epsilon\,\sigma^{12}}{5\,a\,r}[(a-r)^{-10} - (a+r)^{-10}] - \frac{\mathcal{C}\,\epsilon\,\sigma^{6}}{2\,a\,r}[(a-r)^{-4} - (a+r)^{-4}] \tag{4.77}$$

4.2.2.2 Boundary Conditions

To ensure that diffusion occurs only in the x direction, two sets of boundary conditions must be applied. The first are Dirichlet boundary conditions [110] which are applied at the $x-y$ and $x-z$ surfaces to ensure no particle moves in the y or z directions. The second are periodic boundary conditions [111-113] which are applied at the $y-z$ surfaces (inlet and outlet) to ensure there is a particle moving in the x directions. The location of the boundary conditions is shown in Figure 4.10. The Dirichlet boundary conditions are defined as follows

$$\psi(x,0,z) = \psi\big(x, L_y, z\big) = 0 \tag{4.78}$$

$$\psi(x,y,0) = \psi(x,y,L_z) = 0 \tag{4.79}$$

while the periodic boundary conditions are

$$\psi(0,y,z) = \psi(L_x,y,z) \tag{4.80}$$

$$\psi(L_x,y,z) = \psi(0,y,z) \tag{4.81}$$

4.2.2.3 Mesh Generation

The finite element mesh grid is generated by using the Gmsh® software [114] and is a three-dimensional structured mesh of 903,317 nodes (651,264 elements) as shown in Figure 4.11.

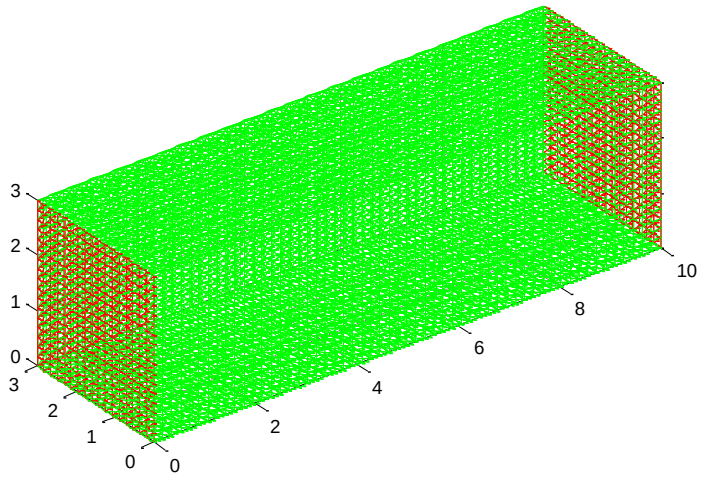

Figure 4.10. Depiction of where the Dirichlet boundary conditions (pictured as green surfaces) and the periodic boundary condition (pictured as red surfaces) are applied.

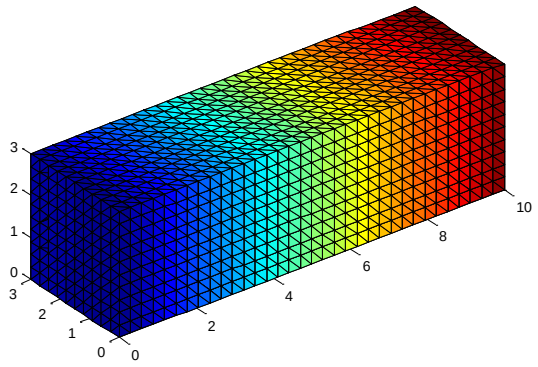

Figure 4.11. The finite element grid mesh (903,317 nodes).

The element is a quadratic (10-node) tetrahedron as depicted in Figure 4.12. It is estimated that grid convergence for this problem is actually reached with about 1,075,033 nodes as shown in Figure 4.13 where an extrapolation from the number of node actually used, i.e., 903,317 nodes, has been made. The reason for not using the larger number of nodes is due to the memory

limitations which were encountered on the supercomputer, Ithaca, where the structured mesh was built. Attempts to build a mesh of 1,075,033 nodes were made but without success.

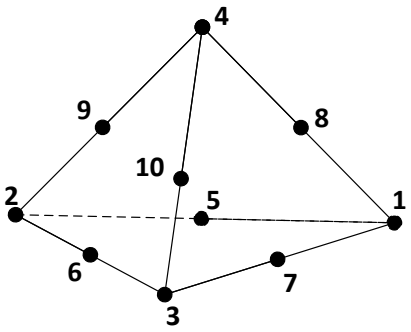

Figure 4.12. The quadratic (10-node) tetrahedral element.

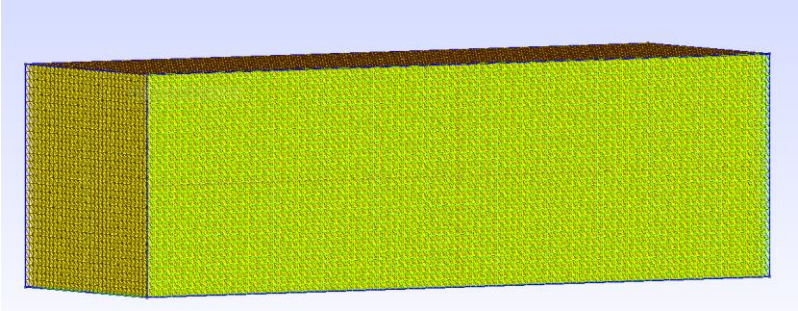

Figure 4.13. The finite element grid mesh (1,075,033 nodes).

Nonetheless, the mesh size used is close enough to the convergent size and, thus, gives some confidence in the eigenfunctions and eigenvalues used to generate the results given in *Chapter* 5 for the open system. The shape or interpolation functions of quadratic tetrahedral element used are the following

$$\begin{array}{ll} \Phi_1 = \lambda(2\lambda - 1) & \Phi_2 = \xi(2\xi - 1) \\ \Phi_3 = \eta(2\eta - 1) & \Phi_4 = \zeta(2\zeta - 1) \\ \Phi_5 = 4\xi\lambda & \Phi_6 = 4\xi\eta \\ \Phi_7 = 4\eta\lambda & \Phi_8 = 4\zeta\lambda \\ \Phi_9 = 4\xi\zeta & \Phi_{10} = 4\zeta\eta \end{array} \tag{4.82}$$

Here $\lambda = 1 - \xi - \eta - \zeta$, and ξ, η, and ζ are the local coordinates of each finite element.

4.2.2.4 Solving the Eigenvalues Problem using the PETSc/SLEPc Software Library

SLEPc® stands for Scalable Library for Eigenvalue Problem Computations [79-81], and is a software library used to solve large-scale spare symmetrical or unsymmetrical eigenvalue problems by using parallel computing. It is an extension of PETSc® that stands for Portable Extensible Toolkit for Scientific Computations [78], and is used to solve either standard or generalized eigenvalue problems for real or complex matrices. In order to download SLEPc®, it is necessary to first download and compile PETSc®. SLEPc® can then be downloaded, complied, and linked to PETSc® because the structure of SLEPc® is based on that of PETSc®. Also, SLEPc® uses the MPI standard for message-passing communication.

In order to solve the eigenvalue problem mentioned above numerically, two main steps are performed in this research. The first is to build the eigenvalue system of equations (the stiffness and mass matrices obtained from the Finite Element Analysis) by using single program multiple date (SPMD) [115] and distributed arrays. A parallel MATLAB® code was written to submit jobs to Ithaca which is an IBM iDatPlex System that provides a parallel MATLAB® cluster on the system-X (i.e., the Virginia Tech supercomputers system). After obtaining the stiffness and mass matrices, the second step is to solve for the eigenvalues and eigenfunctions by using the SLEPc® software library. Parallel c code is submitted as a job to BlueRidge which is a 408-node Cray CS-300 cluster on system-X that provides more available memory than Ithaca. The addition memory is needed to solve the large-scale eigenvalue problem of this research. In case of out of memory, SLEPc® provides parallel eigenvalue solver that is based on PETSc® and MUMPS® (MUltifrontal Massively Parallel sparse direct Solver). PETSc® is used for matrix-vector multiplications while MUMPS® is used for linear system solver in parallel. Parallel eigenvalue solver is used to get more memory and provide faster computation in parallel for the large-scale eigenvalue problem. For large problem, MUMPS® is needed to install with PETSc® before installing SLEPc®. Parallel computer program is written in c-program, and then is submitted to run on BlueRidge which another system of Advanced Research Computing's Systems where all necessary libraries and packages such as SLEPc®, PETSc®, MUMPS®,…etc are installed and are available to be used.

4.2.3 Numerical Solution of the Steady State and Transient Diffusivities

4.2.3.1 Derivative of the Eigenfunctions with respect to x

In order to compute the derivative of the eigenfunctions $\psi(x,y,z)$ with respect to x, i.e., the derivative of $\psi(x,y,z)$ with respect to the global (physical) coordinate, the finite element approximate solution, equation (4.64), is used [88, 90], such that

$$\frac{\partial\psi(x,y,z)}{\partial x} = \sum_{i=1}^{n_d} u_i \frac{\partial\Phi_i(x,y,z)}{\partial x} \tag{4.83}$$

Here $\partial\Phi(x,y,z)/\partial x$ is the derivative of the shape function with respect to x. Note that the shape function, $\Phi_i(x,y,z)$ can be expressed as a function of the local coordinates, i.e., ξ, η, $and\ \zeta$ by means of equations (4.82). To do so requires a relationship between the derivative of the shape function Φ with respect to the global and local coordinates [88]. This relationship is

$$\begin{Bmatrix} \frac{\partial\Phi}{\partial x} \\ \frac{\partial\Phi}{\partial y} \\ \frac{\partial\Phi}{\partial z} \end{Bmatrix} = [J]^{-1} \begin{Bmatrix} \frac{\partial\Phi}{\partial\xi} \\ \frac{\partial\Phi}{\partial\eta} \\ \frac{\partial\Phi}{\partial\zeta} \end{Bmatrix} \tag{4.84}$$

where $[J]$ is the Jacobian matrix which must be non-singular and takes the form

$$[J]_{3x3} = \begin{bmatrix} \frac{\partial\Phi_i}{\partial\xi} \\ \frac{\partial\Phi_i}{\partial\eta} \\ \frac{\partial\Phi_i}{\partial\zeta} \end{bmatrix}_{3xn_d} \quad [x_i \quad y_i \quad z_i]_{n_d x3} \tag{4.85}$$

For $i = 1,2,\ldots,n_d$ where n_d is the number of nodes per finite element, i.e., $n_d = 10$ in terms of the quadratic (10-node) tetrahedral element shown in Figure 4.12.

4.2.3.2 Derivative of the Density Operator with respect to Time

The derivative of the density operator with respect to time, $\partial\rho(t)/\partial t$, is obtained with a finite difference approximation, i.e., using the backward Euler method [116]. The approximation is based on a first order Taylor series expansion, namely,

$$\rho(t-\Delta t)=\rho(t)-\frac{\partial\rho(t)}{\partial t}\,\Delta t \tag{4.86}$$

Solving the latter equation for time derivative leads to

$$\frac{\partial\rho(t)}{\partial t}=\frac{\rho(t)-\rho(t-\Delta t)}{\Delta t} \tag{4.87}$$

where Δt is the step time used when solving the SEAQT equation of motion numerically.

4.2.3.3 Approximate Solution of the Energy Eigenvalue Problem in the x Direction

In addition to the eigenvalues e_{tr} in equation (4.2) which are used to generate e_{tot} in the expression of the diffusivities (equations (4.55), (4.57) and (4.58)), the eigenvalues e_{x_i} in the x direction are needed as well. The eigenvalue problem for this direction is

$$\frac{-\hbar^2}{2\,m_{o_2}}\frac{\partial^2\psi(x)}{\partial x^2}+V(x)\psi(x)=e_x\,\psi(x) \tag{4.88}$$

However, this problem is either impossible or impractical to solve because the potential $V(x)$ is not available. This is circumvented by using the finite-basis approximation [25] to obtain the energy eigenvalues e_{x_i}. It is assumed a trial function in form of a linear superposition, i.e.,

$$\psi_t=\sum_{j=1}^{N}c_j\hat{\psi}(x) \tag{4.89}$$

where c_j is the coefficients, and $\hat{\psi}(x)$ is a set of known orthogonal and normalized basis function. Then, the expectation value of energy $\hat{e}_x$ is given by

$$\hat{e}_x=\sum_{i=1}^{N}\sum_{j=1}^{N}c_j{}^{*}c_j\langle\hat{\psi}_i|H|\hat{\psi}_j\rangle \tag{4.90}$$

by including the normalization condition, the expectation value of energy $\hat{e}_x$ is rewritten as

$$\hat{e}_x=\frac{\sum_{i=1}^{N}\sum_{j=1}^{N}c_j{}^{*}c_j\langle\hat{\psi}_i|H|\hat{\psi}_j\rangle}{\sum_{i=1}^{N}c_i{}^{2}} \tag{4.91}$$

Note that the coefficients c_j is possible complex, thus, $\hat{e}_x$ is defined as

$$\hat{e}_x=\frac{\sum_{i=1}^{N}\sum_{j=1}^{N}\left[\left(a_ia_j+b_ib_j\right)Re\{H_{ij}\}-\left(a_ia_j-b_ib_j\right)Im\{H_{ij}\}\right]}{\sum_{i=1}^{N}(a_i^2+b_i^2)} \tag{4.92}$$

where

$$a_i = Re\{c_i\} \tag{4.93}$$

$$b_i = Im\{c_i\} \tag{4.94}$$

$$H_{ij} = \langle \hat{\psi}_i | H | \hat{\psi}_j \rangle \tag{4.95}$$

The optimization of the trial energy $\hat{e}_x$ with respect a_k yields

$$\frac{\partial \hat{e}_x}{\partial a_k} = 2 \sum_j \left[Re\{H_{kj}\} a_j - Im\{H_{kj}\} b_j - \hat{e}_x a_k \right] = 0 \tag{4.96}$$

and with respect b_k is

$$\frac{\partial \hat{e}_x}{\partial b_k} = 2 \sum_j \left[Im\{H_{kj}\} a_j + Re\{H_{kj}\} b_j - \hat{e}_x b_k \right] = 0 \tag{4.97}$$

The last two equations are consistent with

$$\sum_j H_{kj}\, c_j - \hat{e}_x c_k = 0 \tag{4.98}$$

Equation (4.98) can be written in matrix form as

$$[H]\{c\} = \hat{e}_x\{c\} \tag{4.99}$$

This matrix eigenvalue equation can be solved analytically and $\hat{e}_x$ is the finite-basis approximation to the eigenvalues of the equation (4.88) in the x direction. Note that these approximated eigenvalues, $\hat{e}_x$, are only used in the equations (4.55), (4.57) and (4.58).

Chapter 5 - Results and Discussion

In this chapter, the closed and open thermodynamic systems are studied and modeled using the SEAQT framework to capture their non-equilibrium effects on the diffusivities. For the closed system, the non-equilibrium-based model for atomistic-scale He^3 and He^4 is developed to describe the behavior of the system from the region far from equilibrium to stable equilibrium. The results of the non-equilibrium-based model are validated with that is found in the literature using the conventional approach of classical and quantum mechanics with the probability distribution and partition function at stable equilibrium found from the maximum entropy principle. For the case of the open system, the non-equilibrium-based model for predicting the transient and steady state diffusivities are developed to provide the thermodynamic description for oxygen diffusion through tin anode at atomistic levels. The extended SEAQT equation of motion with two mass interactions [57] is used in order to describe the transient thermodynamic path which the system takes beginning in a transient state far from equilibrium and ending in a steady state in the region near to stable equilibrium.

5.1 Closed System Results

5.1.1 The He^3-He^4 System

At very small scale, He^3 behaves as a fermion, while He^4 behaves as a boson. In order to capture the non-equilibrium behavior of a Boson and Fermion gas based on the SEAQT framework of IQT, the two-particle eigenfunctions of non-interacting Bosons and Fermion gases are used. Figure 5.1 shows the symmetric eigenfuction of a Boson gas and shows the non-symmetric eigenfunction of a Fermion gas at the ground state.

Figure 5.2 shows the energy-entropy diagram of a Boson gas (He^4) and a Fermion gas (He^3) based on the approach described in *Section* 3.1.3. Also shown is the non-equilibrium thermodynamic path of the time evolution of system state from a state initially at non-equilibrium, i.e., A_0, to a final state at stable equilibrium, i.e., A_{se}. As mentioned in *Section* 3.2.1, the initial energy of the system, which is an energy eigenstructure based on 100 energy eigenvalues, is picked to be consistent with a temperature at stable equilibrium of 1K. The non-equilibrium thermodynamic path is then generated by the SEAQT equation of motion for an

isolated, closed system. The non-equilibrium thermodynamic path of the Boson gas (He^4) is shown in Figure 5.2a, while that of the Fermion gas (He^3) is given in Figure 5.2b.

As shown in Figure 5.3, the entropy of the system increases very rapidly at the beginning of the evolution and then slows its increase to reach the maximum entropy value at stable equilibrium state. At the beginning of the evolution, the entropy generation rate $\hat{S}$ has a peak value and then decreases to zero at stable equilibrium state. Note that the entropy generation rate always has positive values.

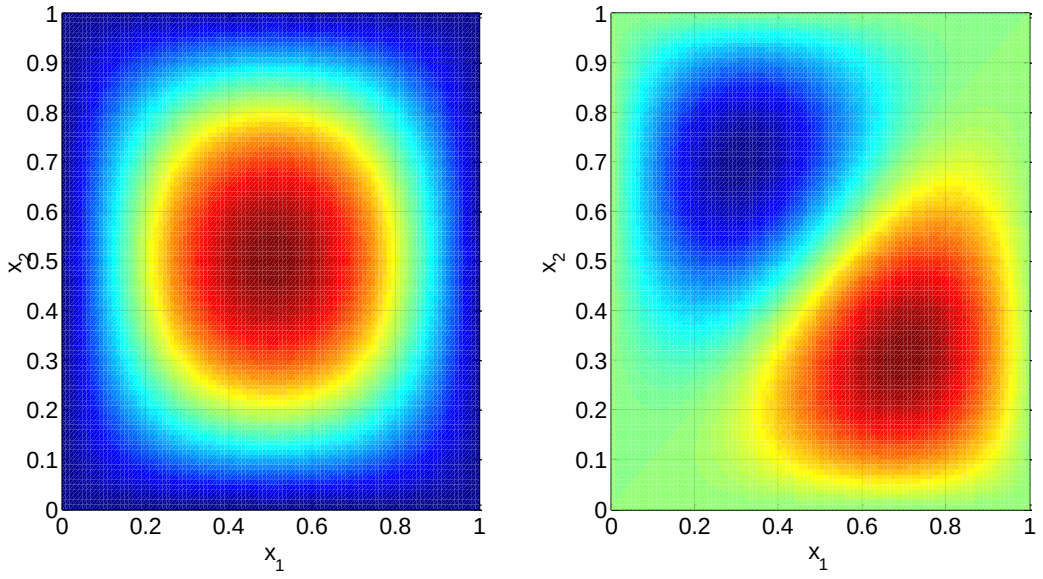

Figure 5.1. The ground-state energy eigenfunctions of (a) a Boson gas (He^4) and (b) a Fermion gas (He^3).

Figure **5.4** shows the energy eigenlevel occupation probabilities derived from the density operator $\rho(t)$ obtained from the SEAQT equation of motion plotted versus the dimensionless time. As seen in the figure, a number of the occupation probabilities have high values relatively at the initial state in the non-equilibrium region, while others are effectively zero. Those with higher values then continually decrease and those with lower increase as the system approaches stable equilibrium. This holds true for both He^4 and He^3. Note that the summation of probabilities over all the energy eigenlevels at each instant of time is conserved, i.e., always equal to one as mentioned in *Section* 1.2.2.

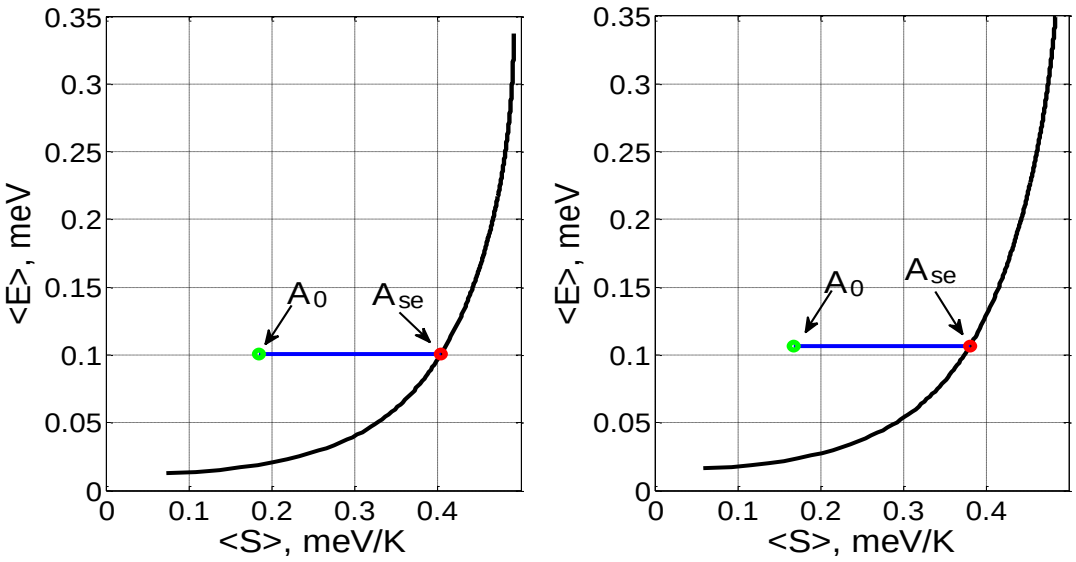

(a) (b)

Figure 5.2. Energy-Entropy diagram at $T_{se} = 1\ K$ associated with 100 energy eigenlevels for (a) a Boson gas (He^4) and for (b) a Fermion gas (He^3) where A_0 and A_{se} represent the initial and final or stable equilibrium states, respectively.

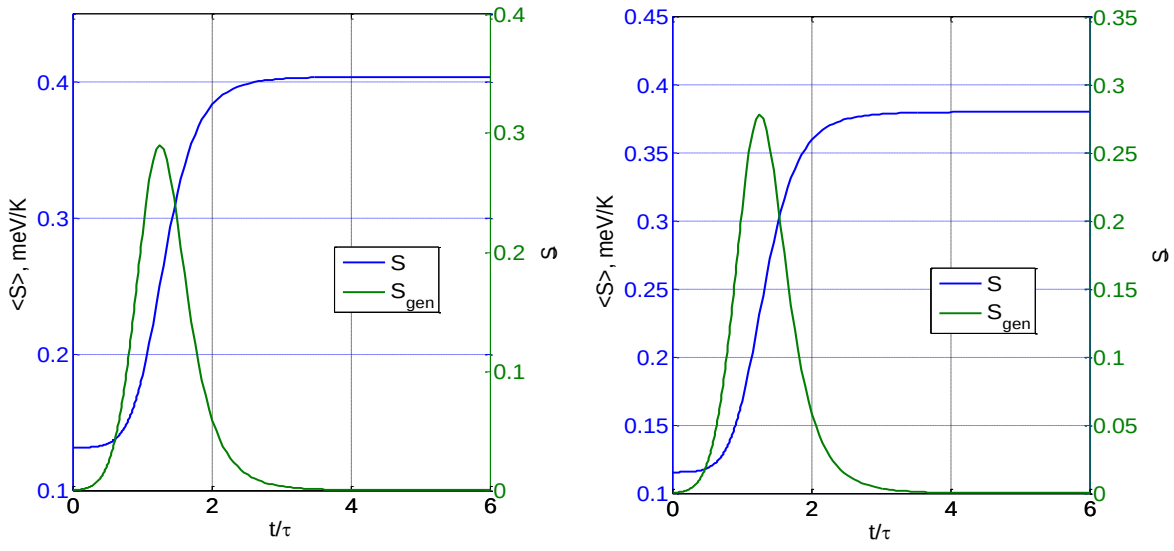

(a) (b)

Figure 5.3. Entropy and entropy generation rate as a function of dimensionless time at $T_{se} = 1\ K$ for (a) He^4 and (b) He^3.

It is seen in Figure 5.5 that an increase in energy results in an increase in the stable equilibrium temperature along the energy-entropy curve. Also, the entropy and entropy generation rate of the system increase with increasing stable equilibrium temperature as shown in Figures 5.6 and 5.7.

Moreover, Figure 5.8 shows that even though each system at constant energy takes a different non-equilibrium path in state space to reach stable equilibrium if initially prepared in different non-equilibrium states, on an energy-entropy diagram, the paths appear to be the same because each path has the same system energy, i.e., the path shown on the energy-entropy diagram is not the thermodynamic path through state space since that path details how the density operator ρ evolves in time (e.g., see Figure 5.4) . In other words, each system has and must have only one stable equilibrium state at constant energy in agreement with the Hatsopoulos-Keenan statement of the second law as mentioned in *Section* 1.2.

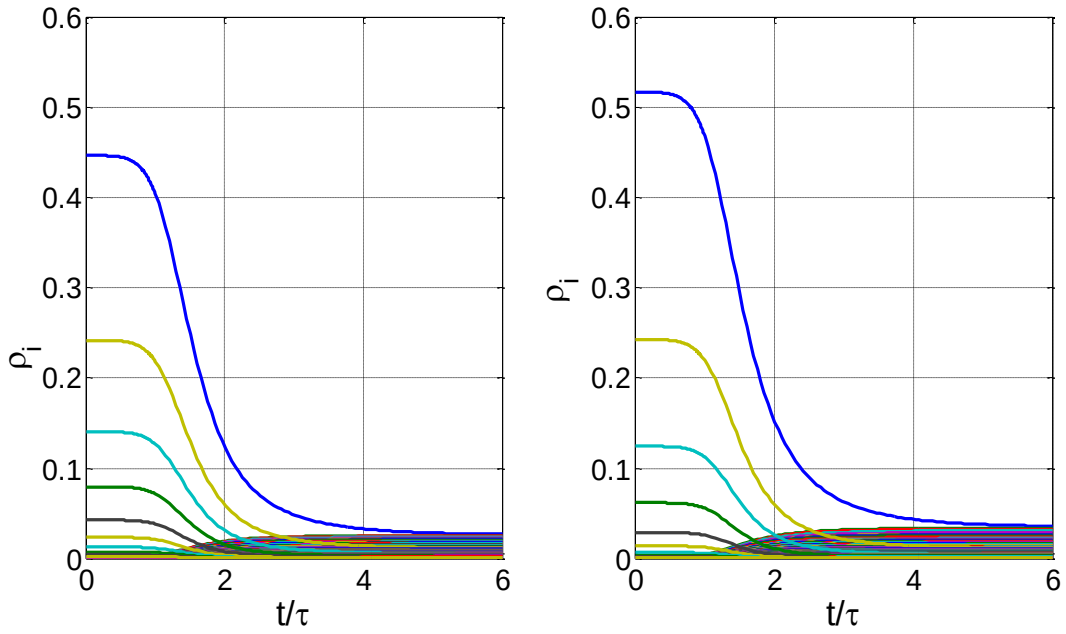

Figure 5.4. Energy eigenlevel occupation probabilities as a function of dimensionless time at $T_{se} = 1\ K$ for the (a) He^4 and (b) He^3.

In addition, Figures 5.9 and 5.10 show that the values of the entropy of the system are the lowest and the entropy generation rates the highest for the path whose initial non-equilibrium state is the farthest from stable equilibrium (i.e., A_{0_1}). In contrast, for the path associated with the initial non-equilibrium state A_{0_3} , which is the closest to stable equilibrium, the system has the highest values of the entropy and the lowest values of the entropy generation rate.

5.1.2 Non-equilibrium Behavior of the Density Distribution

Figures 5.11 and 5.12 show the dimensionless two-particle density distribution at $1\ K$ obtained from the SEAQT framework as described in *Section* 3.1.4.2. As can be seen the correct trends (symmetric and anti-symmetric as well as Maxwellian) for Bosons (He^4) and Fermions (He^3) is captured by the SEAQT framework.

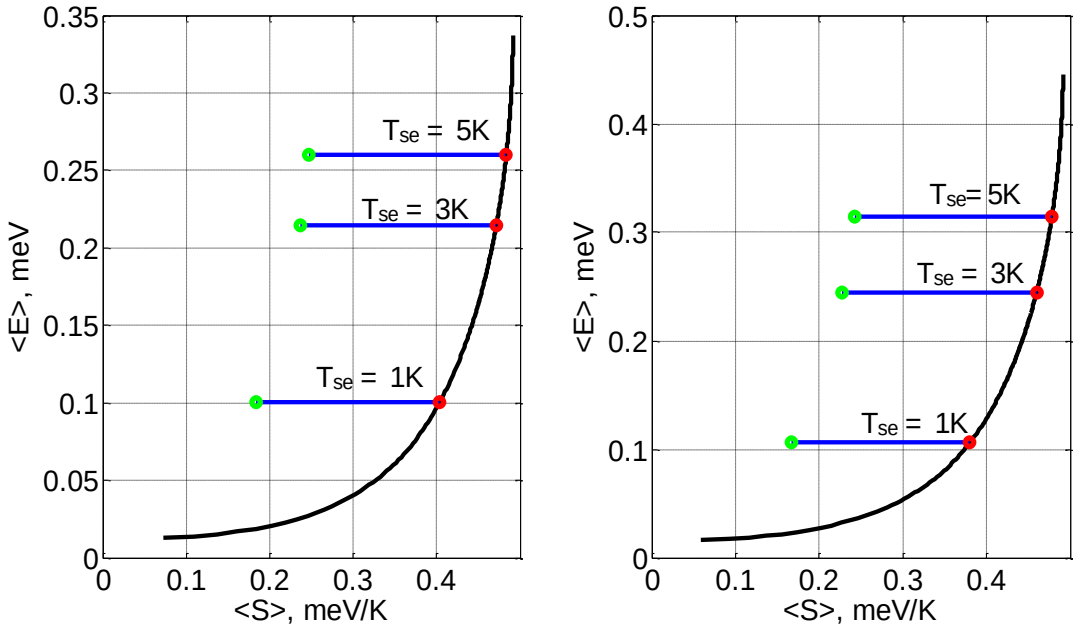

(a) (b)

Figure 5.5. Energy-entropy diagram at different stable equilibrium temperatures ($T_{se} = 1\ K$, $3\ K$, and $5\ K$) for the (a) He^4 and (b) He^3.

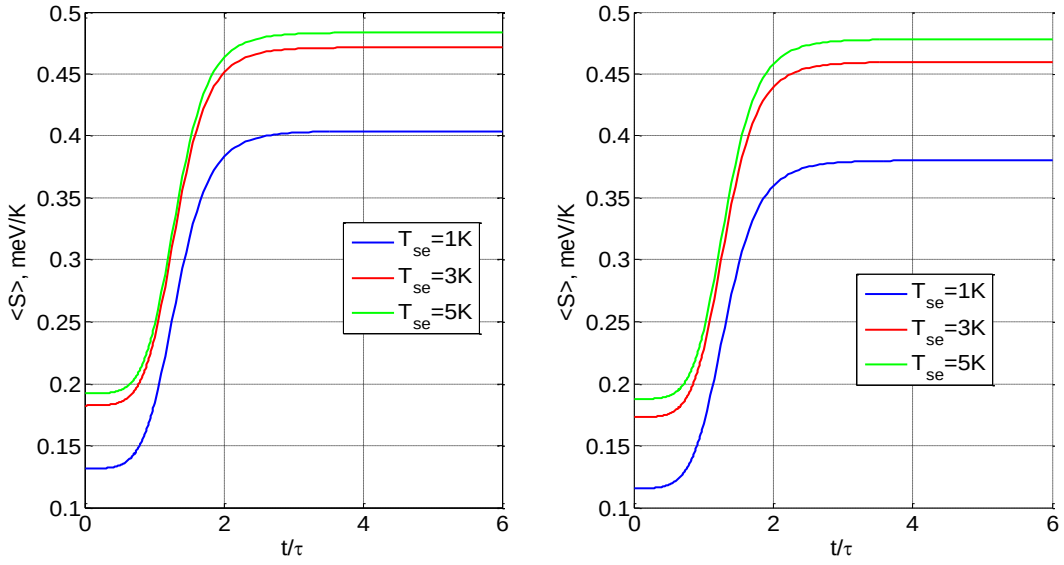

Figure 5.6. Entropy at different stable equilibrium temperatures as a function of dimensionless time for (a) He^4 and (b) He^3.

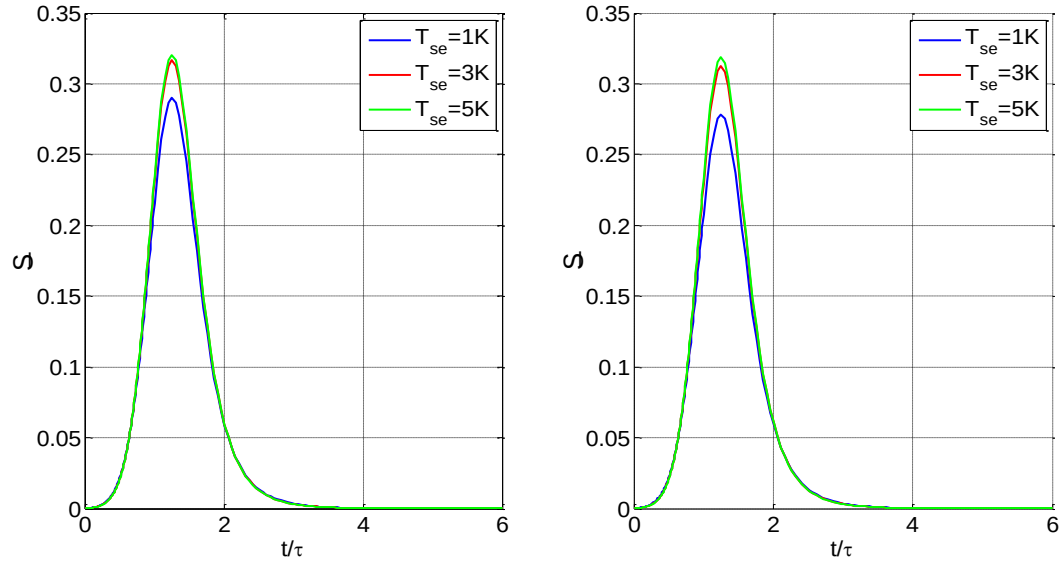

Figure 5.7. Entropy generation rate at different stable equilibrium temperatures as a function of dimensionless time for (a) He^4 and (b) He^3.

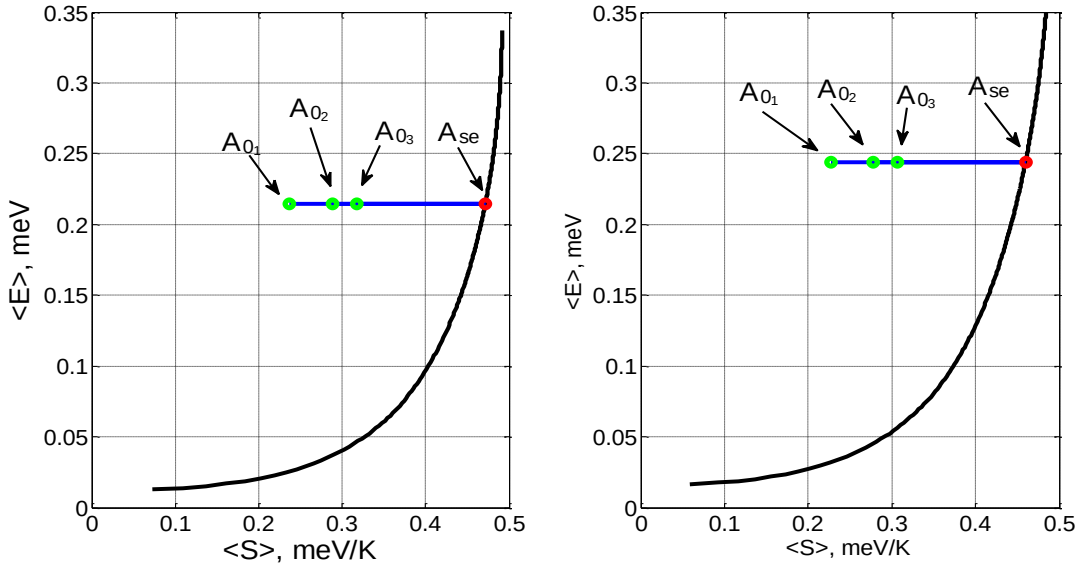

(a) (b)

Figure 5.8. Thermodynamic paths towards the stable equilibrium state A_{se} from different initial states, i.e., A_{0_1}, A_{0_2}, and A_{0_3} at $T_{se} = 3\ K$ for (a) He^4 and (b) He^3.

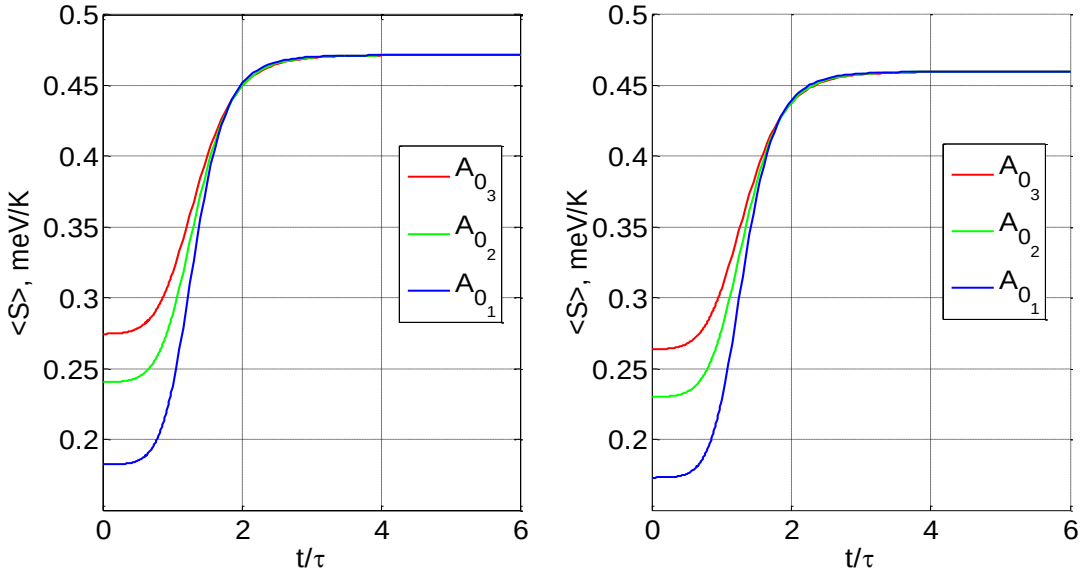

(a) (b)

Figure 5.9. Entropy at different initial states, i.e., A_{0_1}, A_{0_2}, and A_{0_3} as a function of dimensionless time at $T_{se} = 3\ K$ for (a) He^4 and (b) He^3.

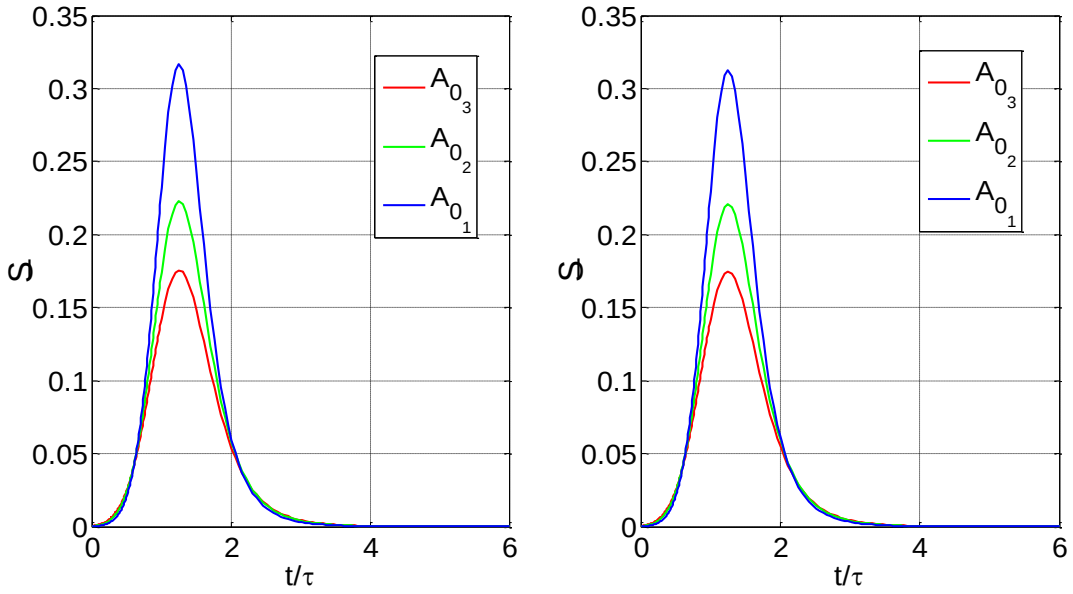

Figure 5.10. Entropy generation rate at different initial states, i.e., A_{0_1}, A_{0_2}, and A_{0_3} as a function of dimensionless time at $T_{se} = 3\ K$ for (a) He^4 and (b) He^3.

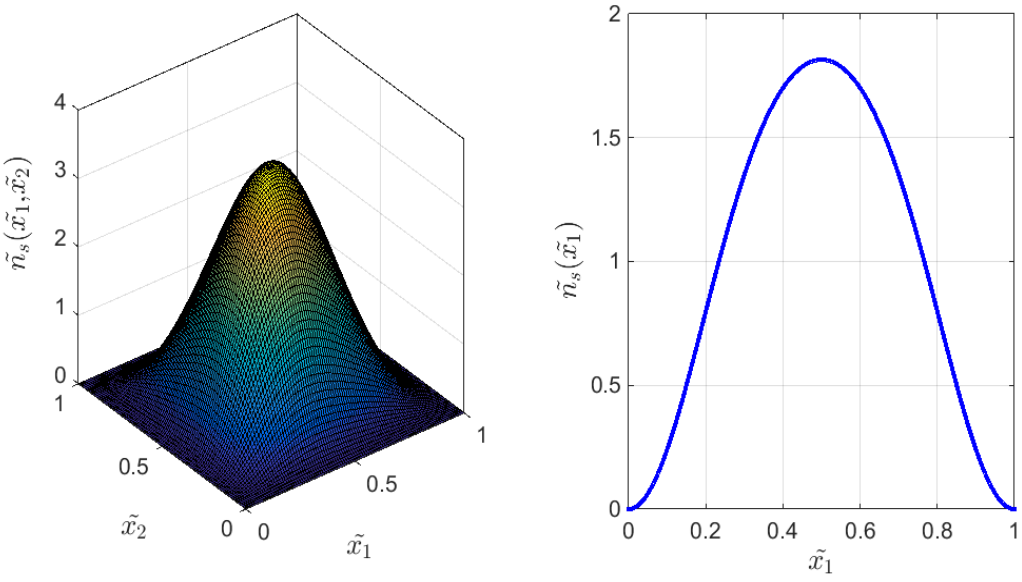

Figure 5.11. Dimensionless SEAQT two-particle density distribution at stable equilibrium and $T_{se} = 1\ K$ for the Bosons gas (He^4) in (a) two dimensions and (b) one dimension.

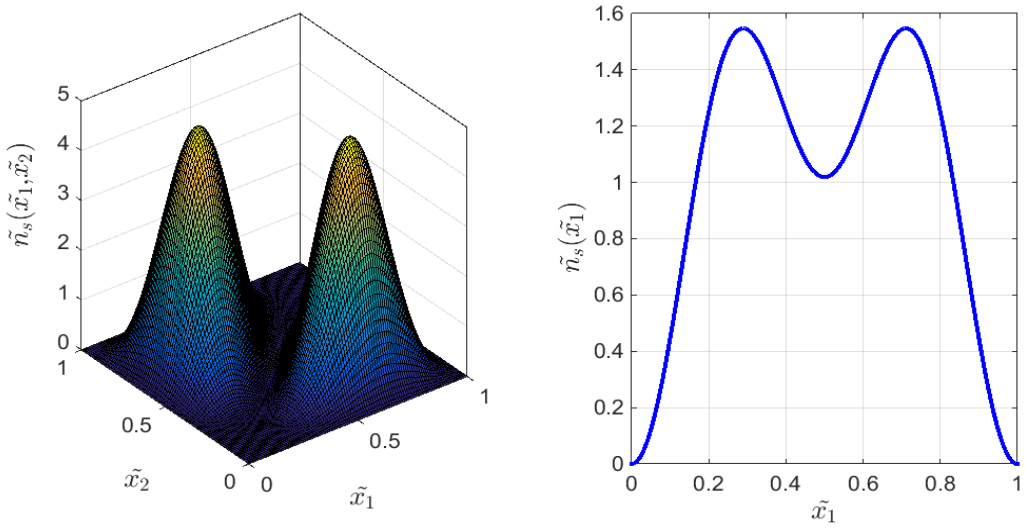

Figure 5.12. Dimensionless SEAQT two-particle density distribution at stable equilibrium and $T_{se} = 1\ K$ for the Fermions gas (He^3) in (a) two dimensions and (b) one dimension.

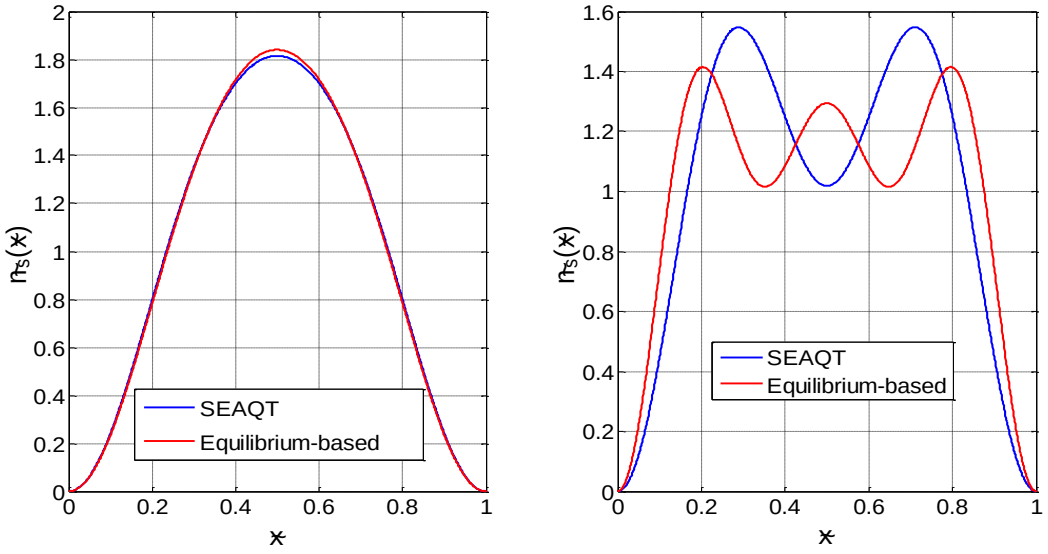

(a) (b)

Figure 5.13. Comparison of the dimensionless SEAQT two-particle density distribution at stable equilibrium with that of the dimensionless equilibrium-based infinite-particle model found in literature [51, 56] at $T_{se} = 1\ K$ for (a) He^4 and (b) He^3.

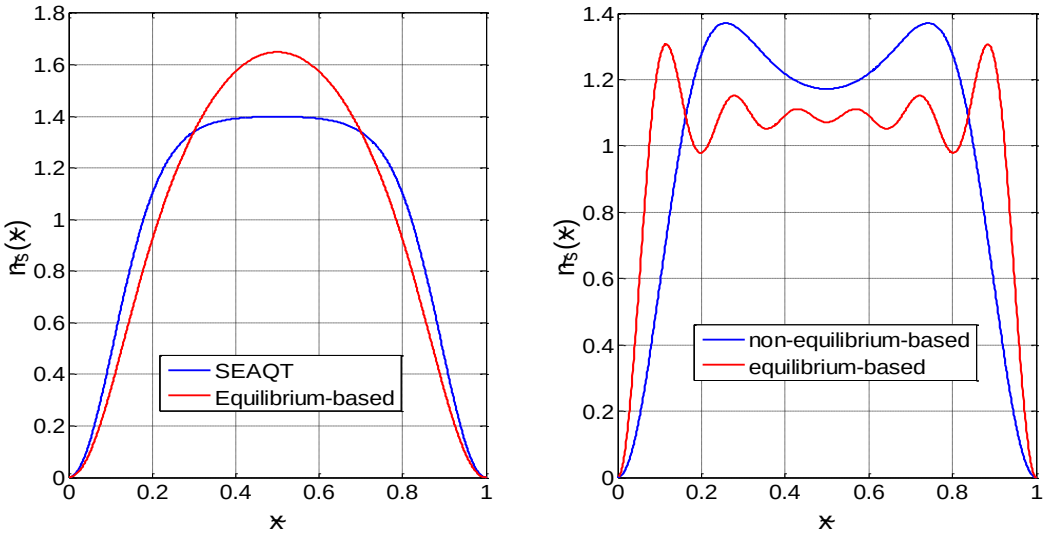

(a) (b)

Figure 5.14. Comparison of the dimensionless SEAQT two-particle density distribution at stable equilibrium with that of the dimensionless equilibrium-based infinite-particle model found in literature [51, 56] at $T_{se} = 3\ K$ for (a) He^4 and (b) He^3.

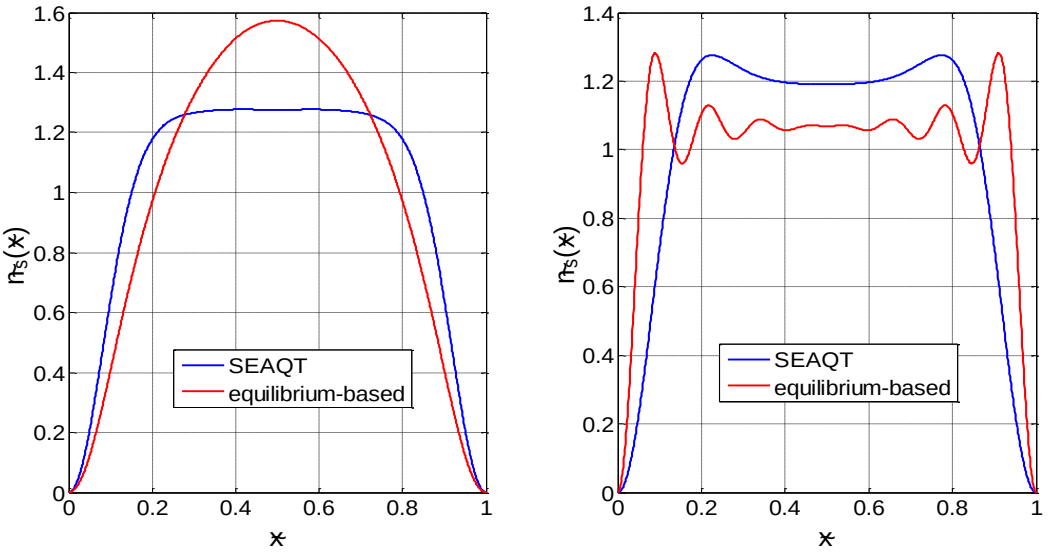

(a) (b)

Figure 5.15. Comparison of the dimensionless SEAQT two-particle density distribution at stable equilibrium with that of the dimensionless equilibrium-based infinite-particle model found in literature [51, 56] at $T_{se} = 5\ K$ for (a) He^4 and (b) He^3.

These trends are given for different temperatures, i.e., $1\ K,\ 3\ K,$ and $5\ K,$ in Figures 5.13 to 5.15 where they are also compare with the density distribution for a many-particle and infinite-eigenlevels system developed with the equilibrium-based model found in [51-54, 56, 68]. Note that the main goal of this study here of the He^3-He^4 system is to demonstrate the ability of the SEAQT framework to capture the non-equilibrium behavior of Bosons and Fermions in closed systems. The comparisons with the equilibrium-based model are simply for the purpose of validation. As can be seen, the comparisons in Figures 5.13 to 5.15 show the same trends. The exact same distributions are not expected due to the differences in the number of particles and eigenlevels considered by the two different models. Matching these is beyond to scope of this doctoral research but is being addressed in the doctoral work of Li [70, 117, 118].

Figures 5.16 and 5.17 spatially and temporally show the non-equilibrium-based and equilibrium density distributions predicted the SEAQT framework for various times from the initially non-equilibrium states to that of stable equilibrium at $3\ K$. In contrast, the equilibrium-based [51, 56] is unable to capture the non-equilibrium behavior exhibited here because it is based on the grand canonical distribution and partition functions found at stable equilibrium [33, 51, 55]. Note that this evolution is for a system of two bosons or two fermions obtained from equation (3.41) and the SEAQT equation of motion. As can be seen in both figures significant spatial and temporal variations from one distribution to the next exist. These variations as is seen later have a major impact on the predication made for the diffusivities. Of course, this is not at all unexpected but to date had not been quantified as has been done here.

Figures 5.18 and 5.19 show the same time evolution as that in Figures 5.16 and 5.17 but now in two instead of one dimension. Clearly, in Figure 5.18 the initial state which is a perturbed partial canonical state shows some degree of uniformity as would be expected but is quickly lost as one proceeds through the nest set of non-equilibrium states at time steps t_1 to t_4. Not until time step t_s at stable equilibrium is complete uniformly reached with the center ellipse representing the maximum values of the density distribution within the system containing the Boson gas (He4). Figure 5.19 shows similar non-equilibrium evolution for the density distribution of the Fermion gas (He3) system with the difference being that the entire evolution maintains the anti-symmetric behavior expected from Fermions.

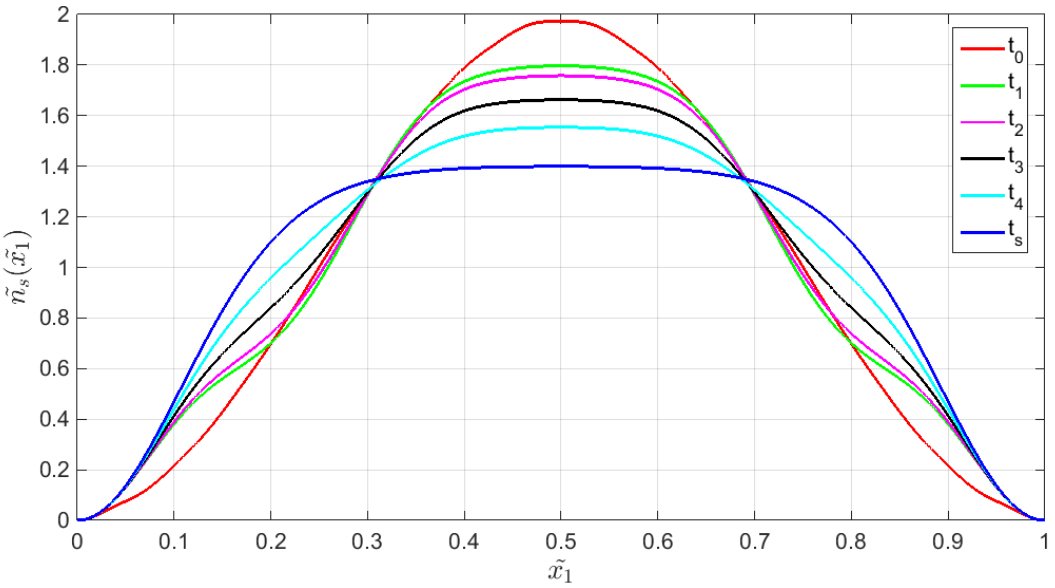

Figure 5.16. Temporal and one-dimensional spatial evolution of the dimensionless SEAQT density distribution for He^4 as the system evolves in time from an initial non-equilibrium state to stable equilibrium state at 3 K.

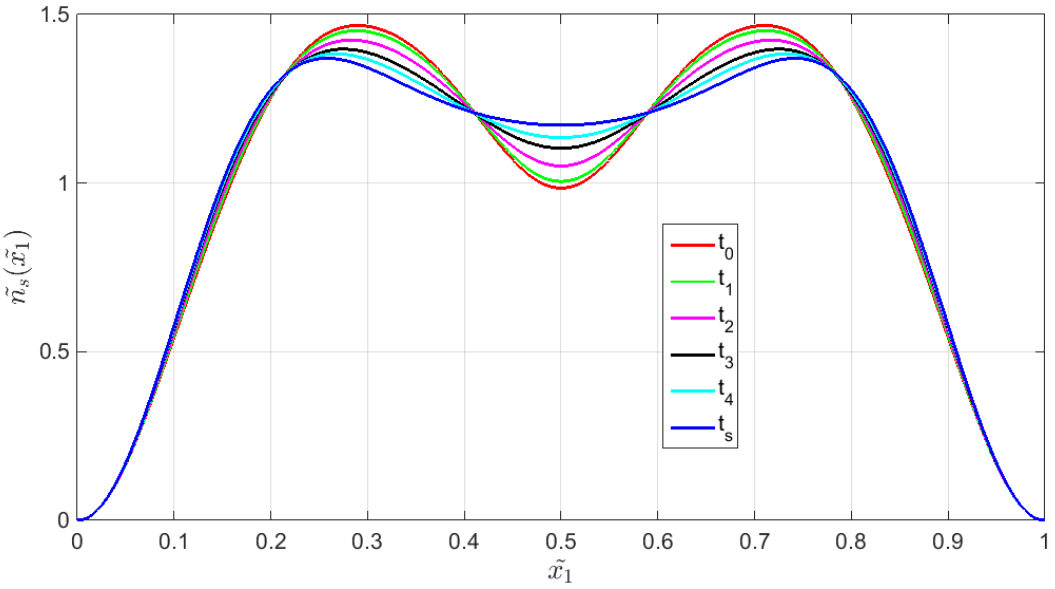

Figure 5.17. Temporal and one-dimensional spatial evolution of the dimensionless SEAQT density distribution for He^3 as the system evolves in time from an initial non-equilibrium state to stable equilibrium state at 3 K.

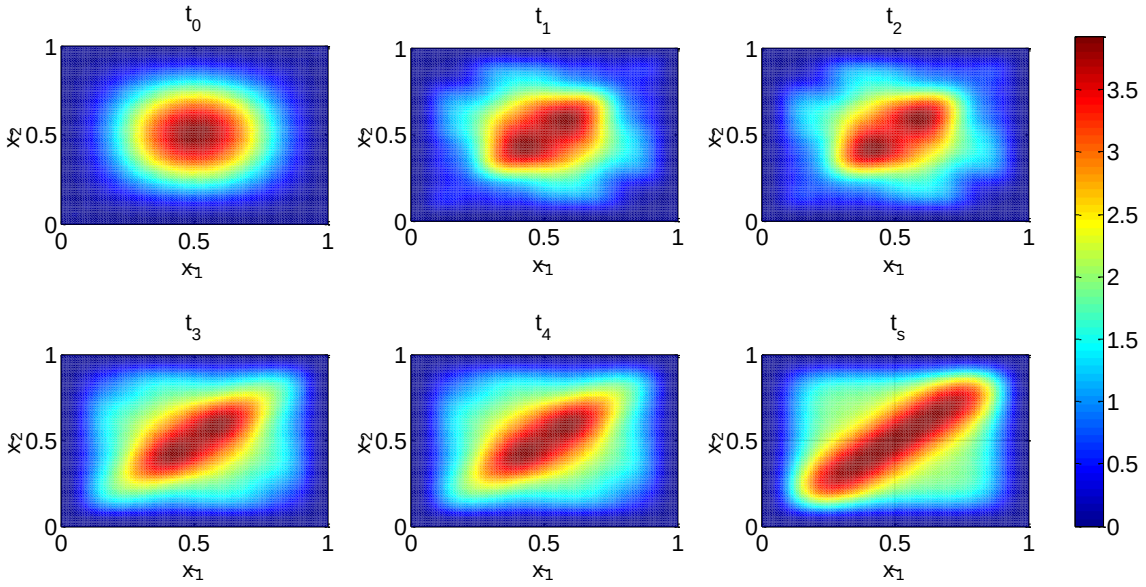

Figure 5.18. Temporal and two-dimensional spatial evolution of the dimensionless SEAQT density distribution for He^4 as the system evolves in time from an initial non-equilibrium state towards the stable equilibrium state at 3 K.

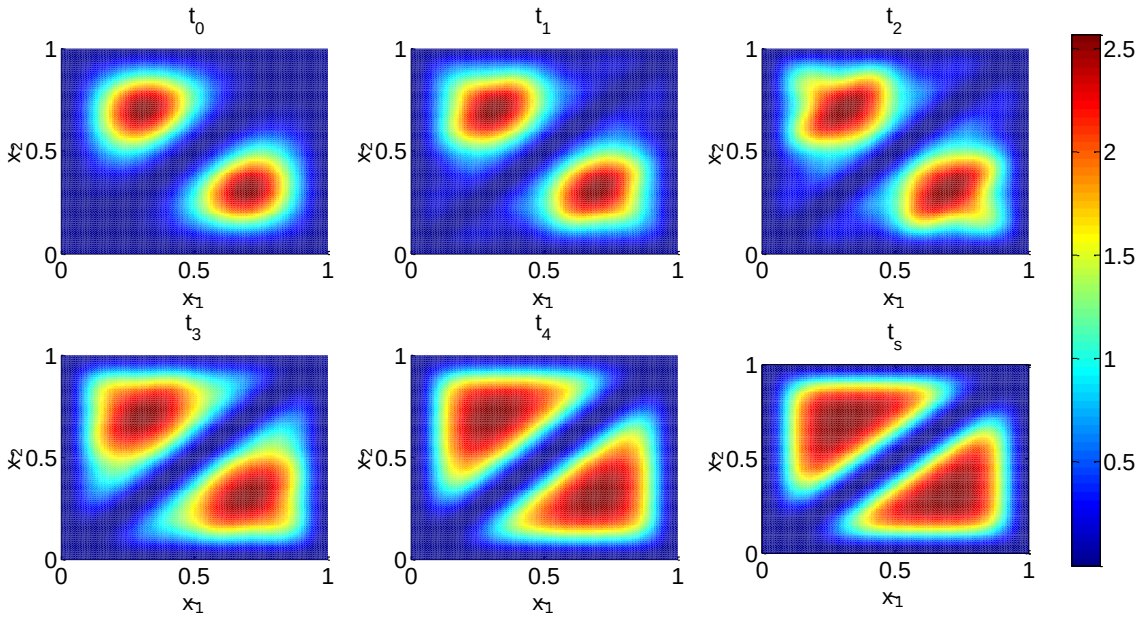

Figure 5.19. Temporal and two-dimensional spatial evolution of the dimensionless SEAQT density distribution for He^3 as the system evolves in time from an initial non-equilibrium state towards the stable equilibrium state at 5 K.

5.1.3 Treatment of Singularities and Runge's Phenomenon

As mentioned in *Section* 3.2.2, two numerical problems appear when performing the numerical integrations required obtain the request diffusivities at both non-equilibrium and equilibrium. The first is the appearance of singularities as shown in Figure 5.20 created by the dominator of equation (3.63) when it is integrated in equation (3.64). This issue is eliminated using polynomial interpolation [73]. The second problem is that of the Runge's phenomenon which appears when the polynomial interpolation is used. As shown in Figure 5.21, this phenomenon occurs at the edges of the interval when equispaced nodes are used and is eliminated by using Chebshev nodes which provide more nodes at the edges. As can be seen in the figure, the space between equispaced nodes (pictured as red dots) is the same; as a result, the line (pictured as a green line) has Runge's phenomenon at the boundary when a high order of the polynomial interpolation is used, while the space between the Chebshev nodes (pictured as black dots) is small at the boundary and large in the interior. That leads to the blue line which has no issue at the boundary.

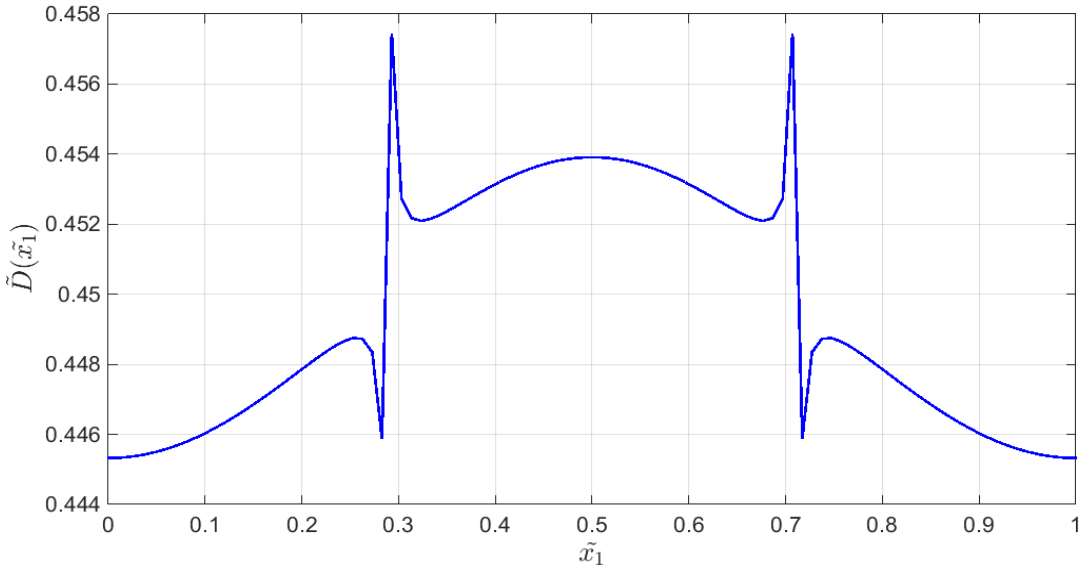

Figure 5.20. Plot of the dimensionless diffusivities for He3 at stable equilibrium with the singularities indicated at $\tilde{x}_1 = \{0.29, 0.71\}$ that occur during the numerical integration.

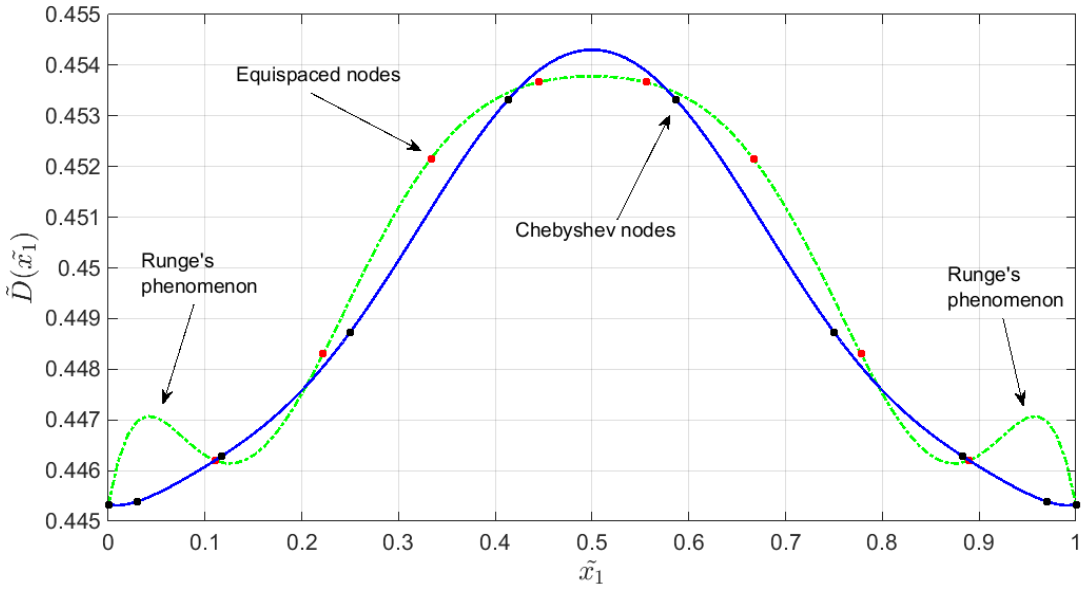

Figure 5.21. Illustration of the treatment of singularities and Runge's phenomenon using interpolation and Chebyshev nodes.

5.1.4 Non-equilibrium Behavior of the Diffusivities

Figures 5.22 and 5.23 show the temporal and spatial evolution of the dimensionless non-equilibrium and equilibrium diffusivities for Boson (He^4) and Fermion gases (He^3), respectively. In Figure 5.22, it is seen that at the initial state, the diffusivity of He^4 has its peak value at the middle of the box and has its lowest values at the boundary. As the system state evolves from this initial state to one of stable equilibrium, the values of the diffusivity of He^4 in the middle of the box decrease, while those at the boundary increase so that at stable equilibrium the peak is at the boundary and the lowest value is in the middle. In contrast, as can been seen in Figure 5.23 at the initial state for He^3 its diffusivity is highest at the boundary and lowest about a quarter of the way into the box from either end. As the system state relaxes from this initial state to stable equilibrium, the diffusivity of He^3 decrease at the boundaries as well as in the middle until at stable equilibrium the diffusivity is highest in the middle and lowest at the boundaries. Clearly, the behavior of He^3 is markedly different than that of He^4 whether in state of non-equilibrium or stable equilibrium. Now, Figure 5.24 shows the temporal and spatial evolution of the non-equilibrium-based diffusivity ratio of He^3 to He^4 when the system state relaxes from its initial state to stable equilibrium. Initially, the diffusivity ratio has its highest values at the boundary

and its lowest in the middle of the box. This gradually reverses itself so that the highest value occurs in the middle of the box and its lowest at the boundary. Clearly, the opposite behavior for He^3 and He^4 indicate that the binary diffusion coefficients (diffusivities) of He^3 into He^4 and He^4 into He^3 are not equal and that the diffusion of He^4 into He^3 is strongest since even the lowest diffusivity values for He^4 are greater than the highest for He^3.

Figures 5.25 and 5.26 show the temporal and two-dimensional spatial evolution of system state from its initial non-equilibrium state to stable equilibrium. For the Fermion, Figure 5.25 clearly shows the initial and intermediate non uniformities in the diffusivities values evolving to a uniform but anti-symmetric distribution of values at stable equilibrium. The same but symmetric behavior observed in Figure 5.26. Figure 5.27 shows the temporal and two-dimensional spatial evolution of the diffusivity ratio of He^3 into He^4. The conclusions drawn earlier in regard to the temporal and one-dimensional spatial evolutions still hold here.

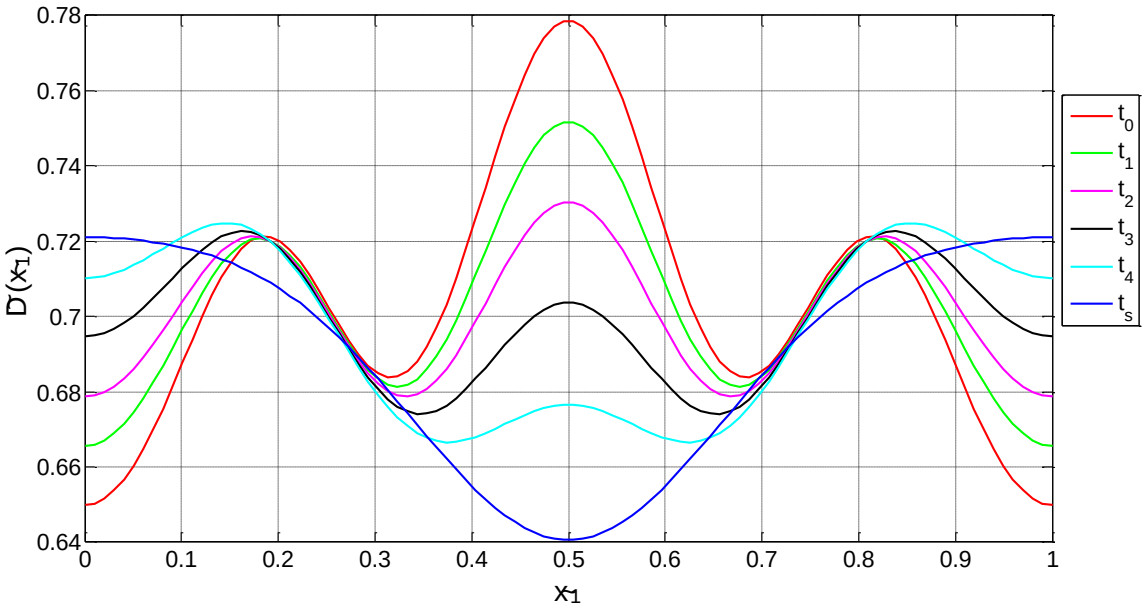

Figure 5.22. Temporal and one-dimensional spatial evolution of the dimensionless non-equilibrium and equilibrium diffusivities for the Boson gas (He^4) when system state evolves in time from a state in non-equilibrium to that at stable equilibrium.

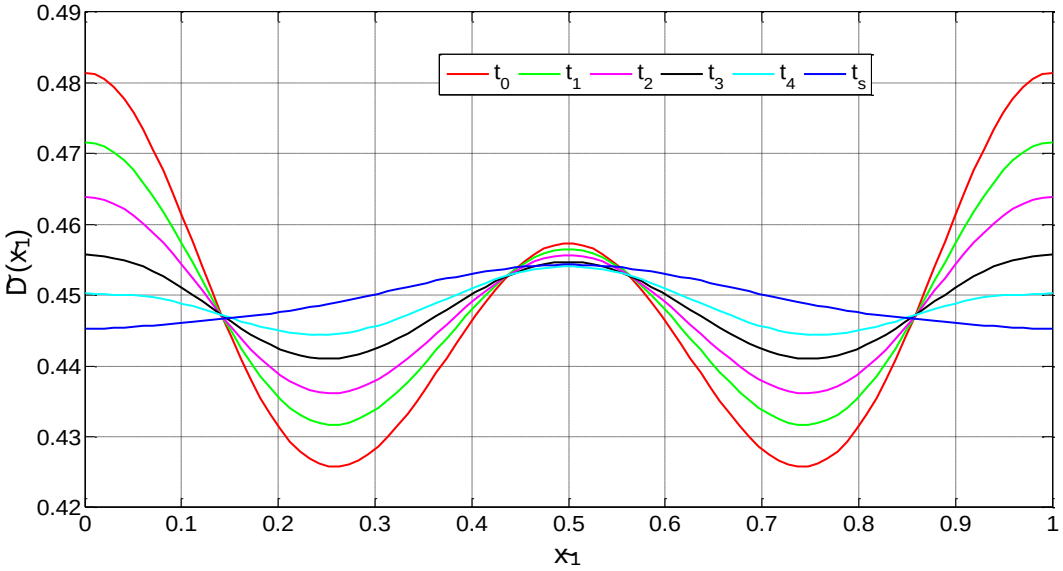

Figure 5.23. Temporal and one-dimensional spatial evolution of the dimensionless non-equilibrium and equilibrium diffusivities for the Fermion gas (He^3) when system state evolves in time from a state in non-equilibrium to that at stable equilibrium.

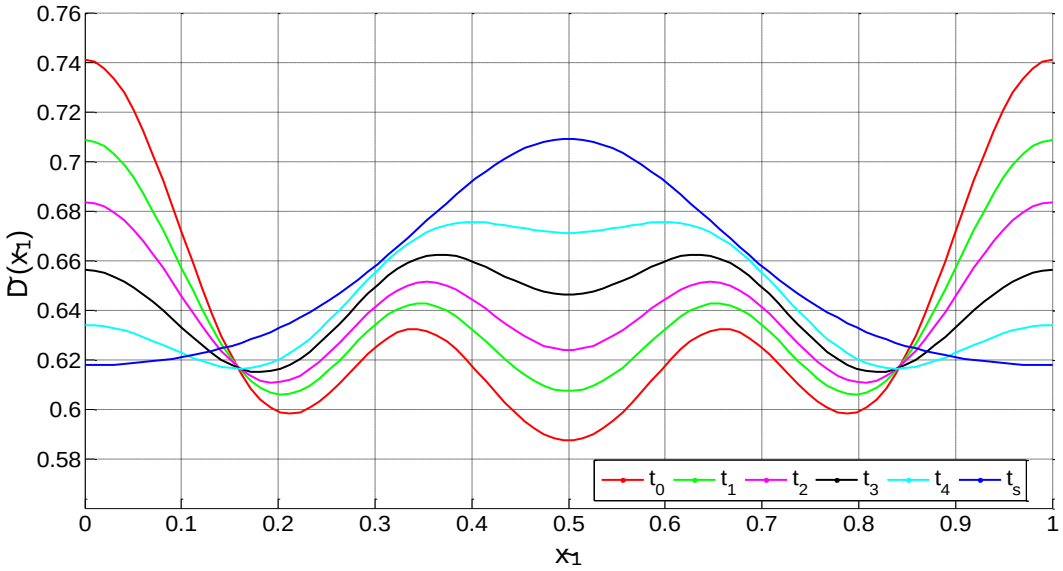

Figure 5.24. Temporal and one-dimensional spatial evolution of the dimensionless non-equilibrium and equilibrium diffusivities ratio of He^3 to He^4 when system state evolves from its initial non-equilibrium to stable equilibrium.

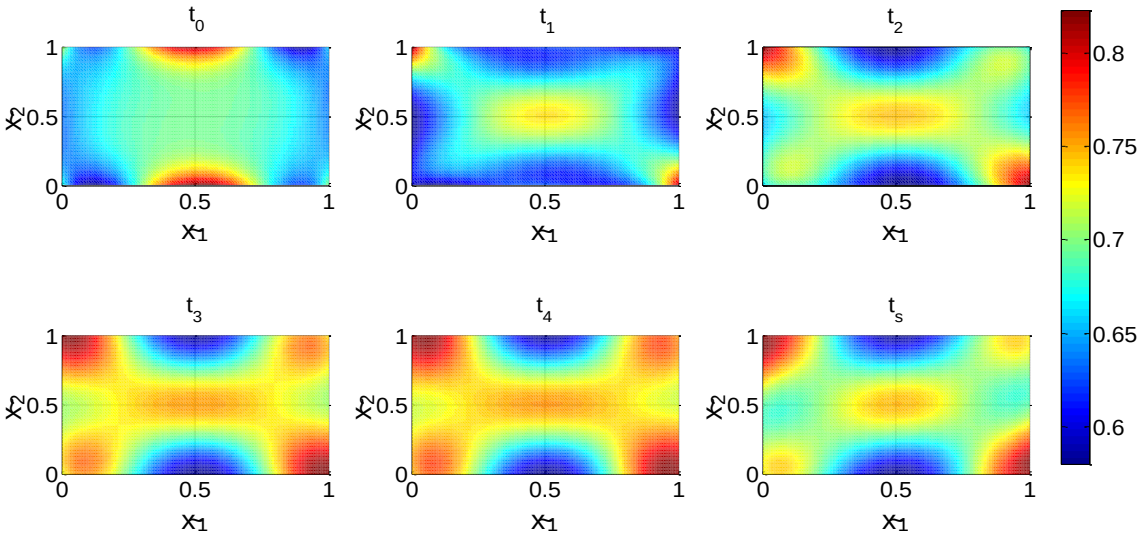

Figure 5.25. Temporal and two-dimensional spatial evolution of the dimensionless non-equilibrium and equilibrium diffusivities for the Fermion gas (He^3) when system state evolves from its initial at non-equilibrium state to stable equilibrium.

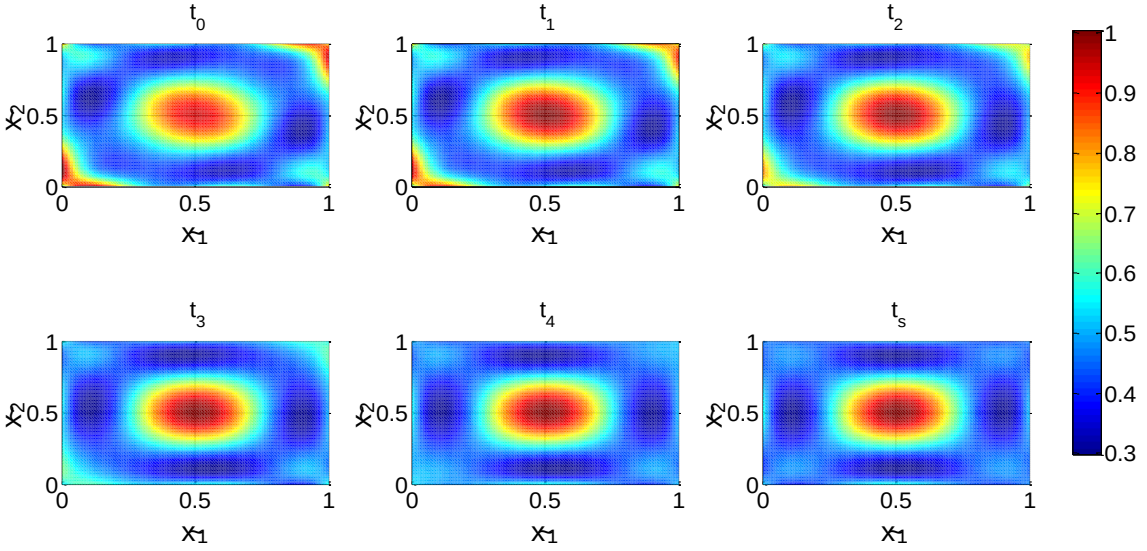

Figure 5.26. Temporal and two-dimensional spatial evolution of the dimensionless non-equilibrium and equilibrium diffusivities for the Bosons gas (He^4) when system state evolves from its initial at non-equilibrium state to stable equilibrium.

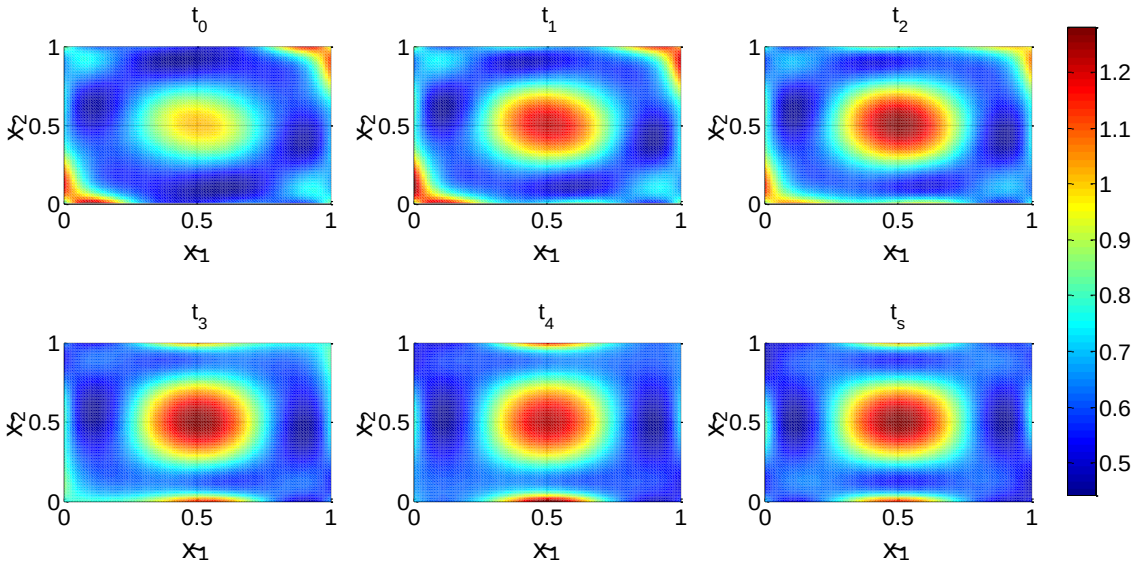

Figure 5.27. Temporal and two-dimensional spatial evolution of the dimensionless non-equilibrium and equilibrium diffusivity ratio of He^3 to He^4 when system state evolves from its initial at non-equilibrium state to stable equilibrium.

5.2 Open System Results

5.2.1 Energy Eigenstructure of an Open System

The energy eigenstructure of a diatomic gas, e.g., an oxygen molecule, is based on at least of three energy eigenmodes, i.e., translational, vibrational, and rotational, as described in equation (4.1). The translational energy eigenvalues are obtained by solving equation (4.2) numerically using a Finite Element Method, while the rotational and vibrational energy eigenvalues are computed analytically using equations (4.3) and (4.5), respectively. In order to solve the translational energy eigenvalue problem for the oxygen molecule in an open system, periodic boundary condition is applied at the mass inlet and outlet boundaries of the system as described in *Section* 4.2.2.2. The translational eigenvalue problem is solved after which the eigenvalues of ordered from smaller to larger.

To solve these two large-scale non-symmetric generalized eigenvalue problems two steps are required. The first is to compute the stiffness and mass matrices of the eigenvalue problem using Galerkin's finite element method, and the second is to use SLEPc which is a software library constructed based on PETSc and MUMPS to solve the large-scale eigenvalue problem in

parallel. PETSC is used to read the matrices in binary format, and MUMPS is used to perform the parallel mathematical operations for the linear system as described in *Section* 4.2.2.4.

Sufficiently accurate numerical solutions for the translational energy eigenvalue problems require sufficiently fine grids meshes which in turn lead to increases in computational time. For large problems, this increase can be significant. Oftentimes a balance must be struck between desired accuracy and computational loads. Of course, mesh convergence occurs when the numerical solution does not change significantly with more mesh refinement. In order to perform a test mesh for convergence, different grid mesh sizes are generated from coarser to finer as shown in Table 5.1. A set of energy eigenvalues for each mesh is computed by solving the eigenvalue problem around a fixed eigenvalue target, i.e., in this case zero, and then each set is plotted versus its mesh size as shown in Figure 5.28. The test for mesh convergence is performed by comparing the eigenvalue set. Figure 5.28 shows that the differences between sets are decreasing as the mesh is refined. In other words, the difference between the eigenvalues for mesh # 1 (30,769 nodes) and those for mesh # 2 (97,811 nodes) is much larger than the difference between the eigenvalues for mesh # 8 (750,921 nodes) and those for mesh # 9 (903,317 nodes).

Table 5.1. Different grid mesh used.

Mesh Name	Number of Elements	Mesh Nodes
Mesh # 1	20,400	30,769
Mesh # 2	67,500	97,811
Mesh # 3	97,104	139,377
Mesh # 4	160,800	228,275
Mesh # 5	266,112	374,003
Mesh # 6	315,000	441,669
Mesh # 7	428,064	597,115
Mesh # 8	540,000	750,921
Mesh # 9	651,264	903,317

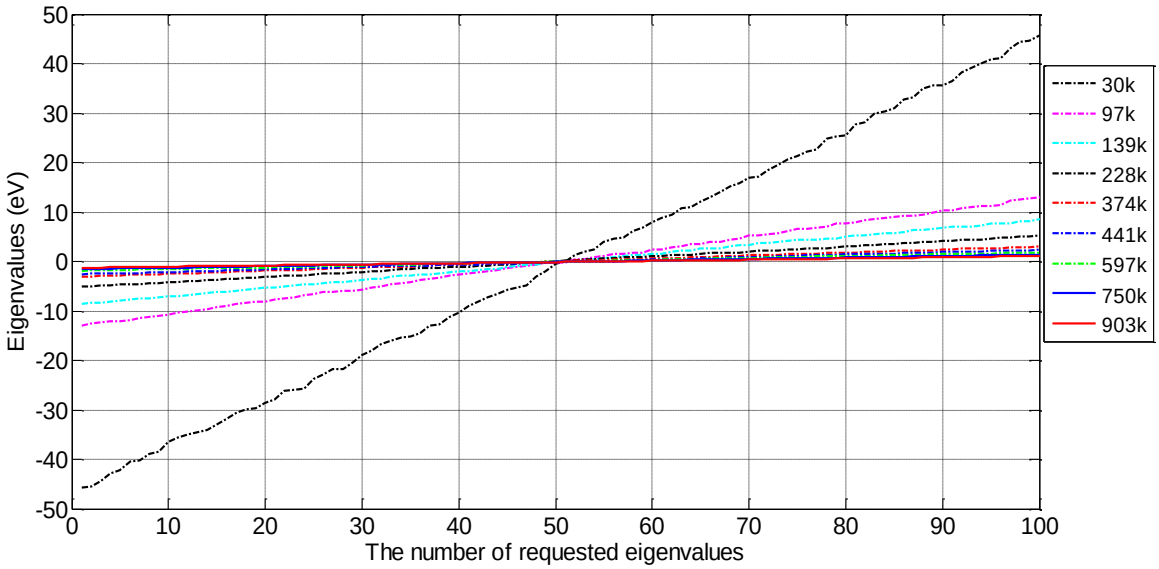

Figure 5.28. Energy eigenvalues around zero for different mesh sizes.

Mesh convergence can also be seen by only comparing the maximum and minimum eigenvalues between meshes. This is shown in Figures 5.29 and 5.30 where the maximum and minimum eigenvalues for the different meshes are plotted versus the number of nodes. As can be seen, the difference between the maximum or minimum eigenvalues of mesh # 9 (903,317 nodes) and mesh # 8 (750,921 nodes) is much smaller than that between mesh # 1 (30,769 nodes) and mesh # 2 (97,811 nodes). Moreover, these figures show that there is little difference between the maximum or minimum eigenvalues for meshes # 8 and # 9 as evidenced by the flattening of the curves. As a result, the numerical solution for the translational energy eigenvalues is assumed to be sufficiently accurate with mesh # 9. It is noteworthy that the computational time for this finer mesh is quite significant and required changing from the original MATLAB® code and PC workstation originally used in this research to the SLEPc® c-code and a supercomputer in order to be able to solve such a large, asymmetrical problem.

As a point of comparison, for example, the computational time for solving for only 10 eigenvalues using Mesh # 2 (97811 nodes) takes 51 minutes using a parallel MATLAB® code running on the Ithaca supercomputer, while it takes 4 minutes using SLEPc® running on the BlueRidge supercomputer. For the larger meshes, the computational times grow exponentially so that the change to SLEPc® and BlueRidge is absolutely necessary.

Note that with larger mesh sizes memory also becomes a very important issue. Once the mesh size is chosen based on mesh convergence, the translational energy eigenvalues computed with this mesh are combines with those for vibrational and rotational to obtain the energy eigenvalues for the system. Key physical parameter values for the oxygen molecule used to compute the rotational and vibrational energy eigenvalues are given in Table 5.2, and the number of energy eigenleves considered for each energy mode and the energy range entailed are given in Table 5.3. Note that the only ten translational energy eigenlevels, four rotational energy eigenlevels, and one vibrational energy eigenlevel are used to obtain the combined energy eigenvalues of the system. That means that the total energy eigenstructure of the system is described by forty eigenlevels which reflect a combination of the three energy modes.

Table 5.2. Key physical parameter values for the oxygen molecule.

Vibrational Wave Number ω_e **(cm^{-1})**	**Bond Length** d **(10^{-8} cm)**	**Dissociation Energy** D_o **(eV)**
1580.19	1.208	5.116

Table 5.3. Number of energy eigenlevels considered and the energy ranges these entail for each energy mode.

Energy Modes	**Energy Eigenvalues Range**	**Energy Eigenlevels**
Rotation	$0 \longrightarrow 0.0021$ (eV)	first 4 eigenlevels
Vibration	$0 \longrightarrow -5.018$ (eV)	first eigenlevel
Translation	$-3.16 \times 10^3 \longrightarrow -188.84$ (eV)	first 10 eigenlevels

5.2.2 Non-equilibrium Evolution in State of an Open System

In modeling the non-equilibrium behavior of oxygen diffusion through a tin anode as an open system, the SEAQT framework developed by Smith and von Spakovsky [57] is used. Within this framework, the transient and steady state diffusivities are predicted as the state of the system relaxes from a state of non-equilibrium to that of steady state. Equation (4.6) of this framework is able to capture the non-equilibrium behavior of diffusions due to the dispassion process going on inside the system and to the mass interactions of the system with two mass

reservoirs. In other words, two governing equations must be solved. One is used to obtain the eigenstructure of the system as mentioned in *Section* 5.2.1 and another is for determining the unique non-equilibrium thermodynamic path which the system state takes. Note that a number particle operator for oxygen is needed by the equation of motion. This is in addition to the Hamiltonian operator which is required. The number particle operator is represented by a diagonal matrix with particle eigennumbers along the diagonal, while the Hamiltonian operator is represented by a diagonal matrix with energy eigenvalues along the diagonal.

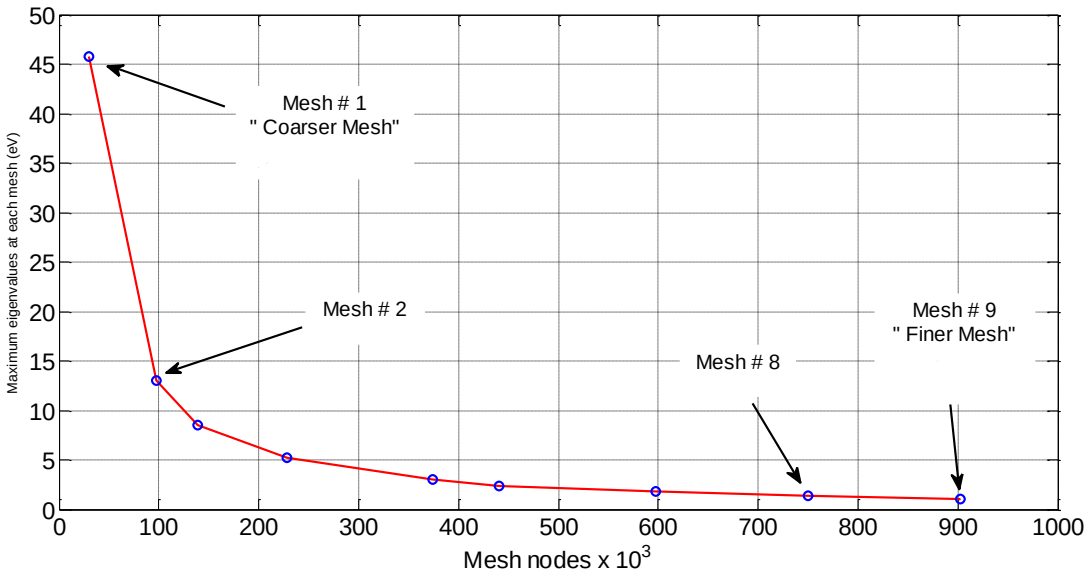

Figure 5.29. Plot of the maximum eigenvalues versus number of mesh nodes.

To solve the SEAQT equation of motion with two mass interactions, a number of steps must be followed. The first involves generating the stable-equilibrium hypersurface for the three-dimensional $< E > - < S > - < N >$ space as shown in Figure 5.31 and then choosing two points on the surface that represents states of mutual stable equilibrium between the system and each mass reservoir. Table 5.4 shows these two states represented by $\langle S_{eq} \rangle, \langle H_{eq} \rangle$, and $\langle N_{eq} \rangle$ in equations (4.41) to (4.44) for each reservoir.

The second step in the procedure to solve the SEAQT equation of motion is to choose another state which is far from the stable equilibrium surface which can be used as the initial

non-equilibrium state of the system as mentioned in *Section* 4.2.1. Table 5.4 shows pertinent property expectation values for the initial non-equilibrium state of the system chosen.

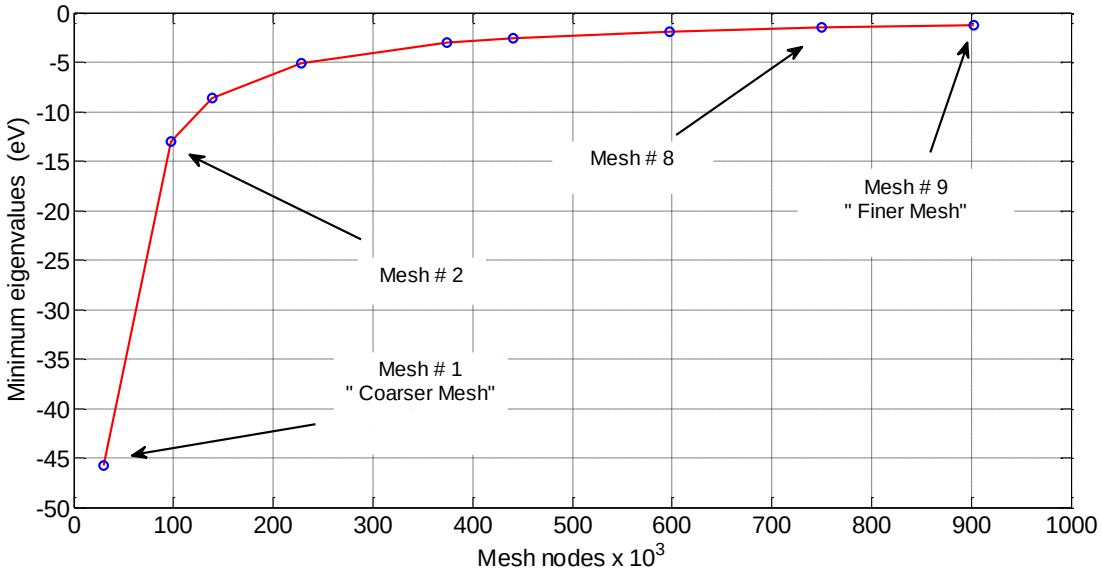

Figure 5.30. Plot of the minimum eigenvalues versus the number of mesh nodes.

Table 5.4. Expectation values of the energy, particle number and entropy for the initial state of the system and for the system in mutual stable equilibrium with the mass reservoirs.

	$< E >$ (keV)	$< N >$	$< S >$ (eV/K)
Mass Reservoir #1, G_1	-2.505	0.4242	2.345
Initial Non-equilibrium State	-2.45	0.7	1.9
Mass Reservoir #2, G_2	-2.415	0.9798	3.034

The final step in the procedure to solve the SEAQT equation of motion with two mass interactions is to actually solve it based on the states chosen, i.e., the initial non-equilibrium state far from the surface and the two stable-equilibrium states on the surface. Note that the non-equilibrium thermodynamic path (blue curve) shown in Figures 5.31 to 5.33 is dependent on the values of the relaxation times, i.e., τ_D, τ_{G_1} and τ_{G_2}, that impact the dynamics (but not the

kinetics) and, thus, the relative strengths of the dissipation and mass-interaction operators in equation (4.6). Table 5.5 shows the values of relaxation times that are used in this work in order to obtain the non-equilibrium thermodynamic path as shown in Figures 5.31 to 5.33.

Table 5.5. The relaxation times that is used in this research.

τ_D	τ_{G_1}	τ_{G_2}
0.6	1.1	1.4

As seen in Figures 5.31 to 5.33 the state of the system relaxes from its initial non-equilibrium state (green circle) to that of steady state (red circle). At the initial non-equilibrium state, the energy, entropy and number of particles of the system are low, after which they increase the steepest entropy ascent path to steady state.

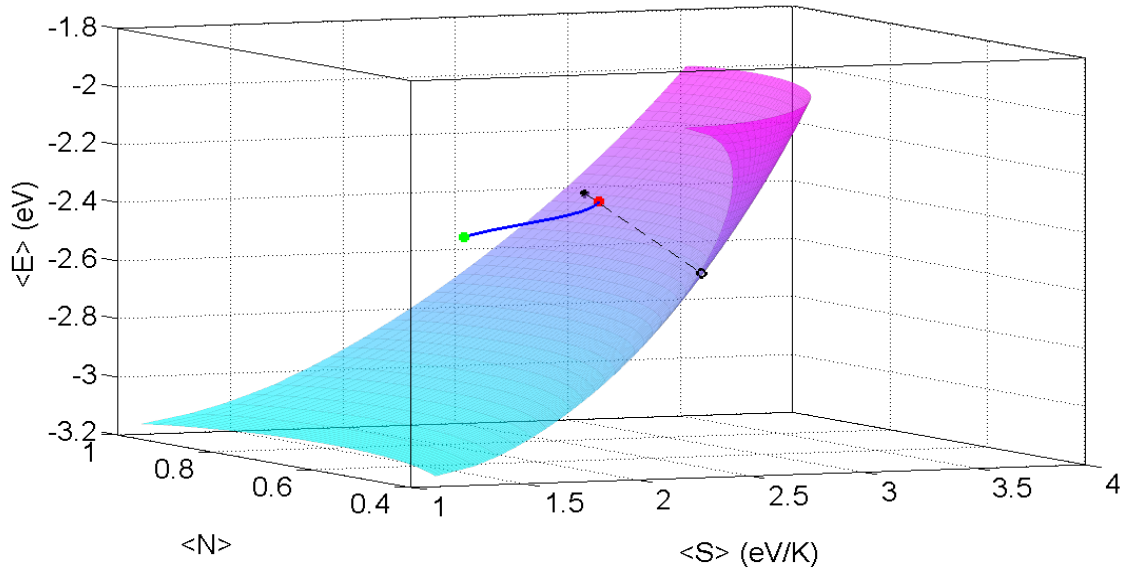

Figure 5.31. Non-equilibrium thermodynamic path (blue curve) that describes the transient relaxation of state of the system towards steady state. The green and red dots represent the initial and steady states of the system, respectively. The black dot on the surface represents the state of mutual stable equilibrium with the first reservoir, while the black circle on the surface represents that with the second reservoir.

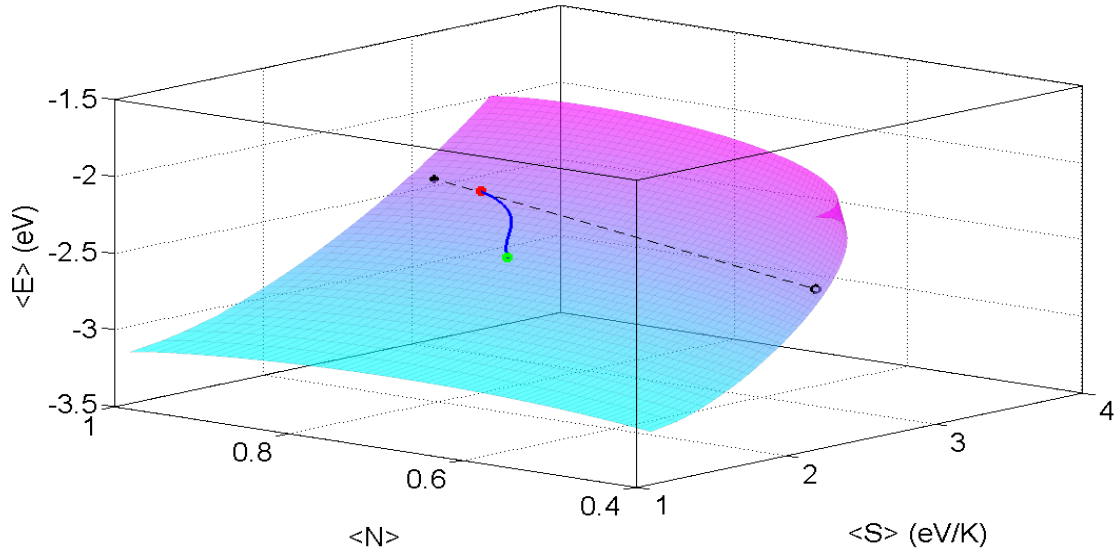

Figure 5.32. Another view of the non-equilibrium thermodynamic path (blue curve). T green and red dots represent the initial and steady states of the system, respectively. The black dot on the surface represents the state of mutual stable equilibrium with the first reservoir while, the black circle on the surface represents that with the second reservoir.

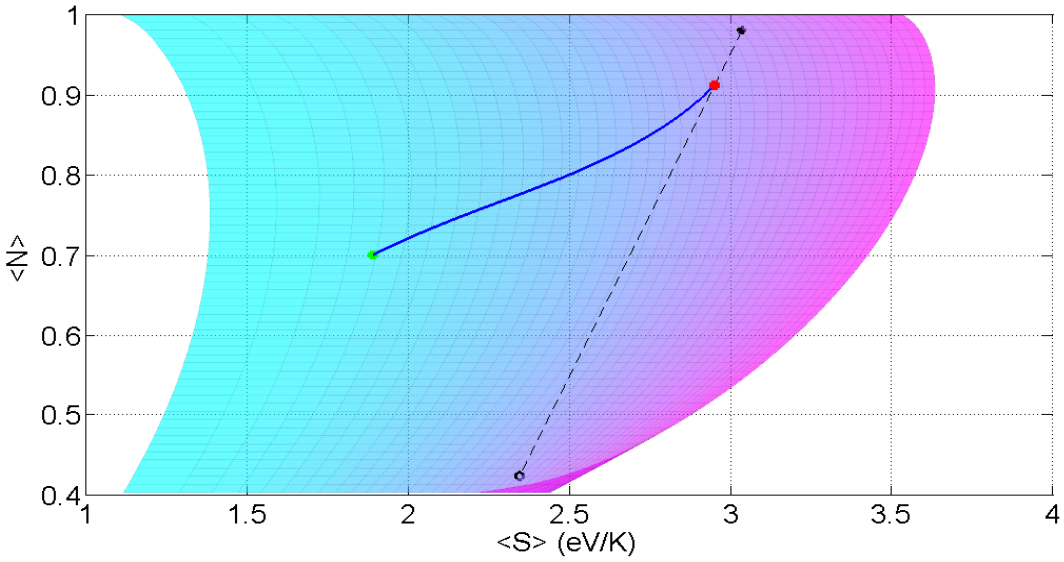

Figure 5.33. A plot in the $< N > - < S >$ plane of the non-equilibrium thermodynamic path (blue curve). The green and red dots represent the initial and steady states of the system, respectively. The black dot on the surface represents the state of mutual stable equilibrium with the first reservoir, while the black circle on the surface represents that with the second reservoir.

Figure 5.34 shows the time evolution of the occupation probabilities of the density operator for the system when it relaxes from the initial state at zero dimensionless time to that of steady state at a dimensionless time of 0.73. As can be seen, the rate of change for the probabilities goes to zero at 0.73. Figures 5.35, 5.36, and 5.37 show the time evolution of the energy, entropy, and number of particles of the system. As seen, the energy, entropy, and number of particles of the system increase their steady state values at a dimensionless time of 0.73. This is consistent with results shown in Figure 5.34.

Note that the maximum values of the energy, entropy, and number of particles occur at steady state as they should since this is an example of a transient processing which the system is charged with mass, i.e., the mass increases with time since more mass enters than leaves. Clearly, all the states that the system passes through from the initial state to that prior to steady state are transient, all of which are more generally characterized as the not stable equilibrium states as shown in Figure 1.2.

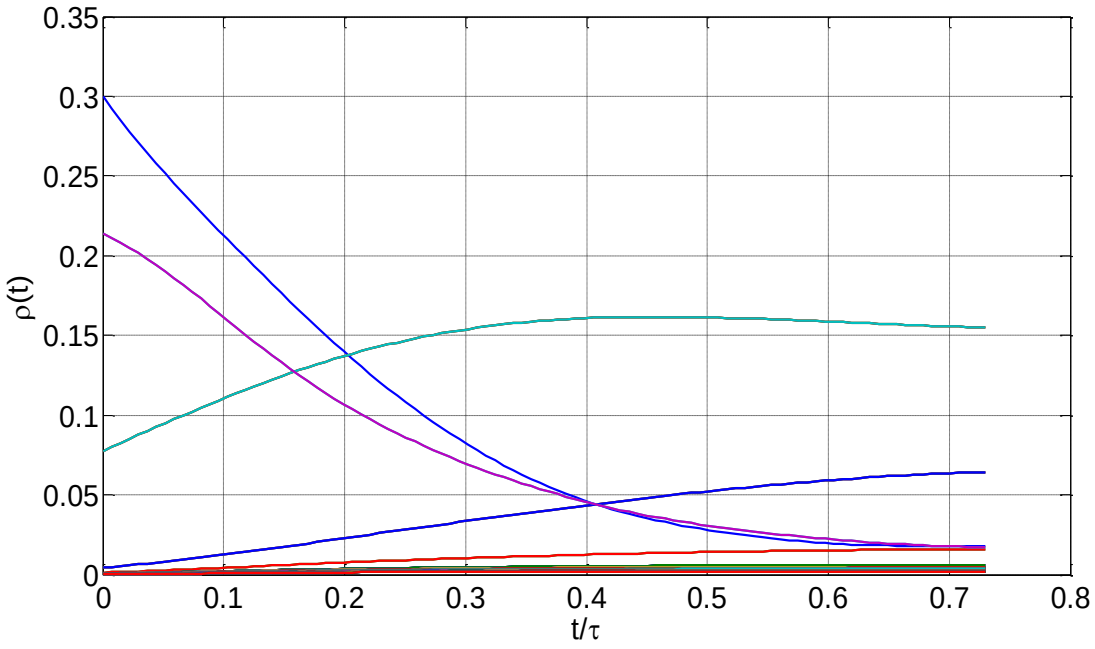

Figure 5.34. Energy eigenlevel occupation probabilities as a function of time for the open system undergoing a dissipation process and two mass interactions.

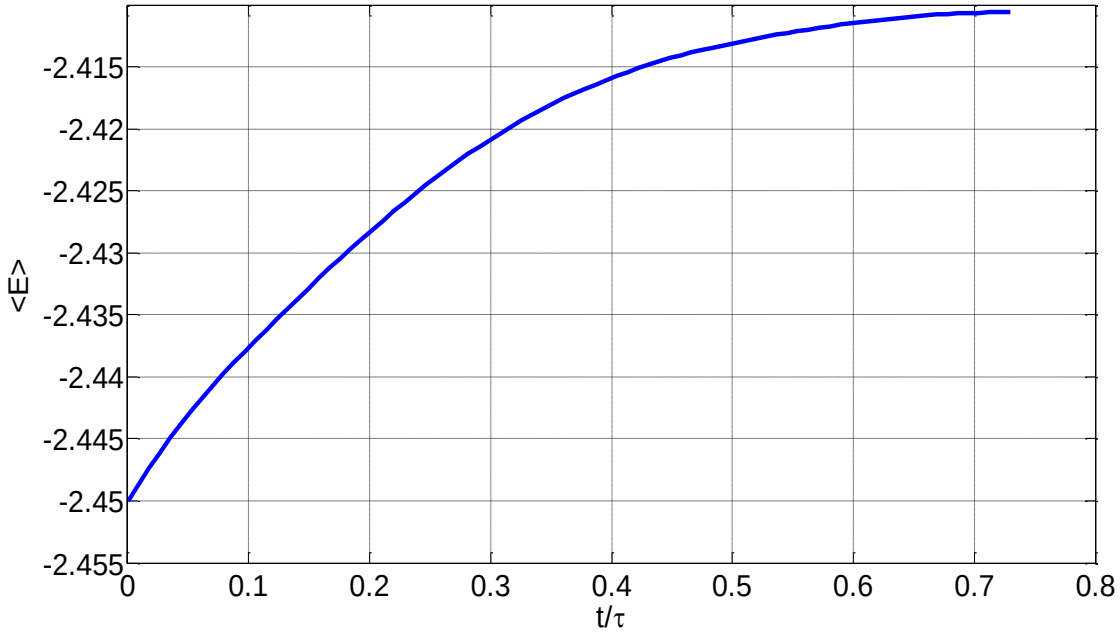

Figure 5.35. Plot of the expectation value of the system energy as a function time for the system.

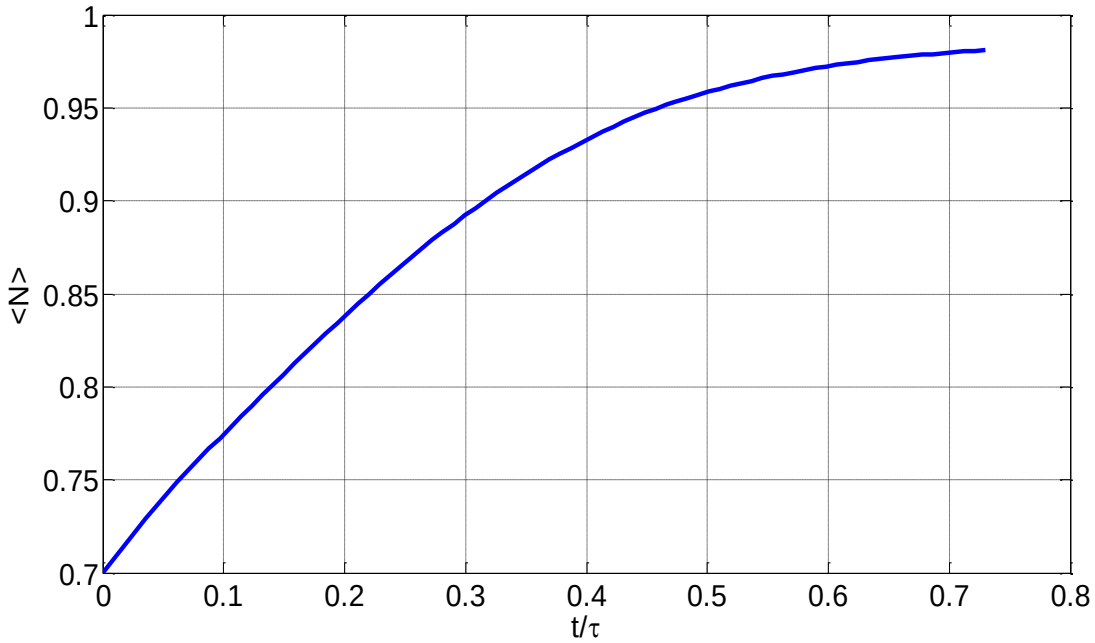

Figure 5.36. Plot of the expectation value of the system particle number as a function time.

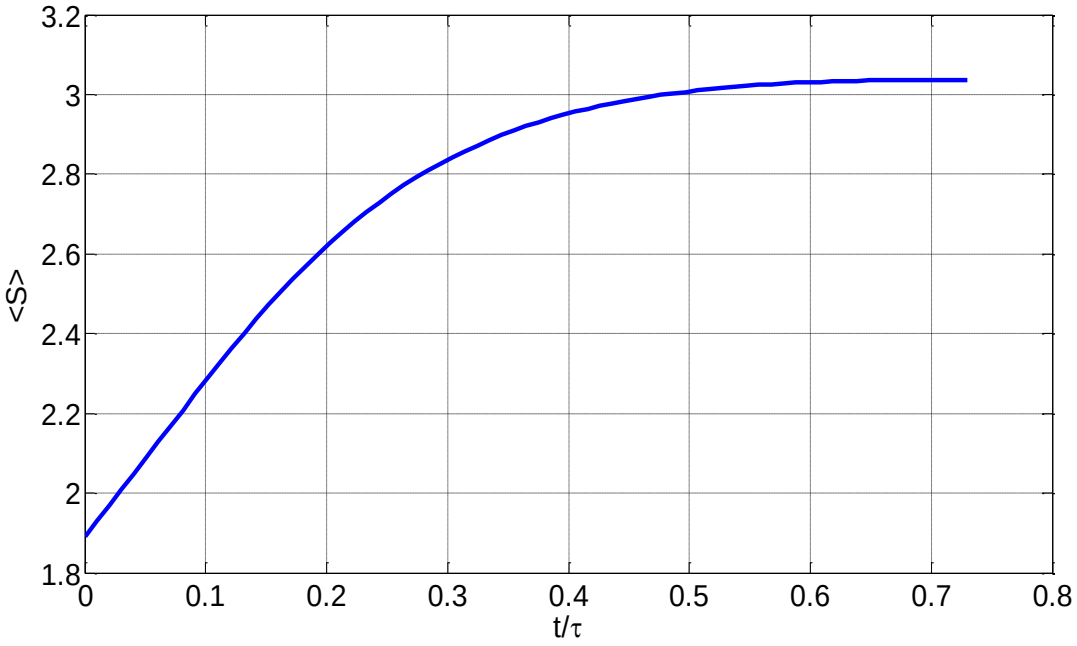

Figure 5.37. Plot of the expectation value of the systementropy as a function time.

5.2.3 Transient and Steady State Density Distributions and Diffusivities

Once the density operators of the system that describe the transient and steady states at every instant of time are obtained, the density distributions and diffusivities for each transient and steady state are determined. The non-equilibrium-based density distributions of the system are determined from equation (4.45) at different dimensionless times in order to demonstrate the evolution of these distributions from the initial non-equilibrium state (transient state) to steady state. Figure 5.38 shows that the mean value of the particle number density distributions in the x direction increases as the system relaxes from its initial state to steady state. As seen the highest value occurs at steady state and the lowest at the initial state. In addition, at each state, the highest value of the density distribution occurs at the inlet of the system, i.e., $x = 0$ and the lowest at the outlet, i.e., at $x = 10$ nm.

Now, in two-dimensional, .i.e., x and y, the time evolution of the density distribution follows the contour seen in Figure 5.39. At the initial state (at t_0), the highest value for the density distribution occurs at the edges ($y = 0$ and $y = 3$) at the inlet surface and the lowest at the outlet surface. As the density distribution evolves in time, the contours change from pointing

towards the inlet to pointing towards the outlet even though. States, the highest values occurs at towards the inlet surface and the lowest towards the outlet surface.

Also, seen in this figure is that the mean values of the density distributions increase in time consistent with the one-dimensional view given in Figure 5.38. Figure 5.40 shows the one-dimensional spatial distribution of values for the transient and steady state diffusivities as the state of system relaxes from its initial transient state to steady state. As seen the transient diffusivity is highest at the initial state and decreases as the system approaches steady state.

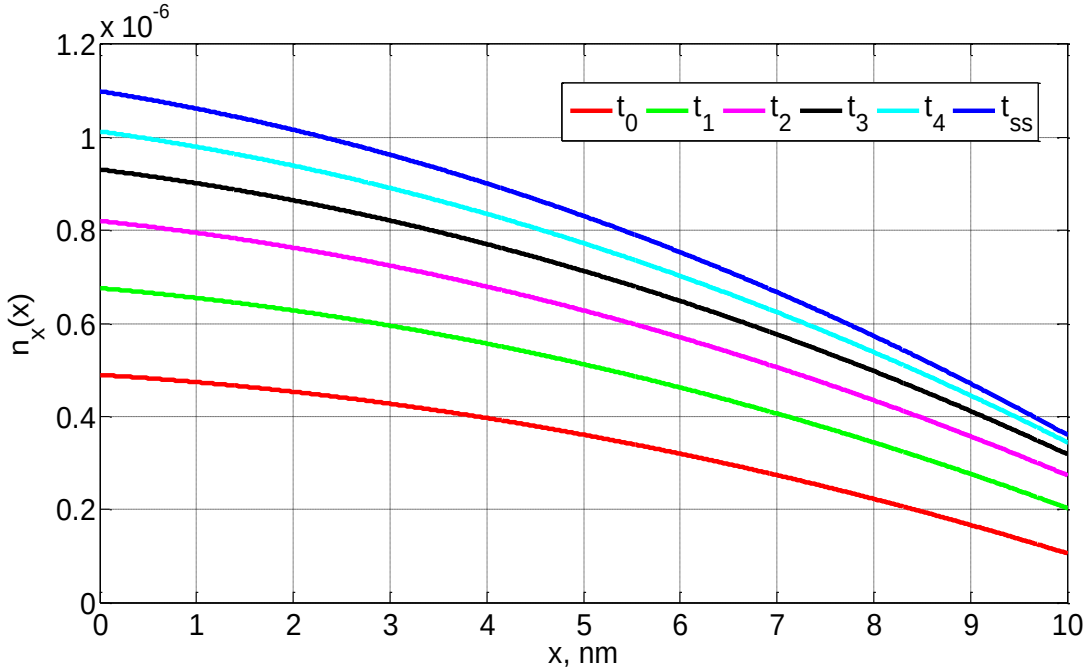

Figure 5.38. Temporal and one-dimensional spatial evolution of the density distribution for the one-particle open system of oxygen diffusion through the tin anode as the system relaxes from an initial transient state to steady state. Here, $y = z = 1.5$ nm.

Each transient spatial distribution of value has its highest value at the inlet surface, its lowest value somewhere in the interior between $x = 5$ nm and $x = 7$ nm, and an intermediate value at the outlet surface. The reason is that the repeated cell tin lattice structure is not symmetric as shown in Figure 4.5. As a result, the number of tin lattice cells in x direction is not even. This means that the highest concentration of tin atoms is off center towards the inlet and, thus, the

lowest transient diffusivities occurs in a range from about $x = 5$ nm and $x = 7$ nm. The result is that the oxygen molecule diffuses more slowly through this region. In contrast, the oxygen molecule diffuses faster at both the inlet and outlet surfaces because the concentration of tin atoms is lowest there. When the system reaches the steady state, the diffusivity values of oxygen are lower than those for the transient states as shown in Figure 5.40. Also, the lowest value occurs at the center of the box, i.e., at $x = 5$ nm, and has the values at the inlet and outlet surfaces are approximate the same. In other words, the steady state spatial distribution of the diffusivity of oxygen is symmetric in the x direction, while those in the transient region are non-symmetric.

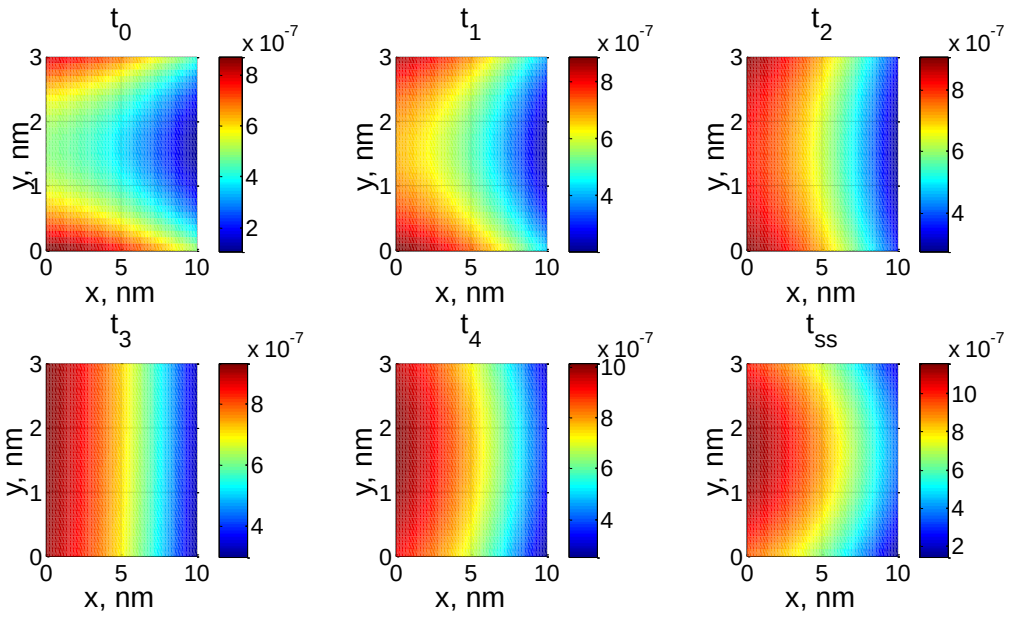

Figure 5.39. Temporal and two-dimensional spatial evolution of the density distributions for the one-particle open system of oxygen diffusion through the tin anode as the system relaxes from an initial transient state to steady state. Here, $z = 1.5$ nm.

Each transient spatial distribution of value has its highest value at the inlet surface, its lowest value somewhere in the interior between $x = 5$ nm and $x = 7$ nm, and an intermediate value at the outlet surface. The reason is that the repeated cell tin lattice structure is not symmetric as shown in Figure 4.5. As a result, the number of tin lattice cells in x direction is not even. This

means that the highest concentration of tin atoms is off center towards the inlet and, thus, the lowest transient diffusivities occurs in a range from about $x = 5$ nm and $x = 7$ nm. The result is that the oxygen molecule diffuses more slowly through this region. In contrast, the oxygen molecule diffuses faster at both the inlet and outlet surfaces because the concentration of tin atoms is lowest there. When the system reaches the steady state, the diffusivity values of oxygen are lower than those for the transient states as shown in Figure 5.40. Also, the lowest value occurs at the center of the box, i.e., at $x = 5$ nm, and has the values at the inlet and outlet surfaces are approximate the same. In other words, the steady state spatial distribution of the diffusivity of oxygen is symmetric in the x direction, while those in the transient region are non-symmetric.

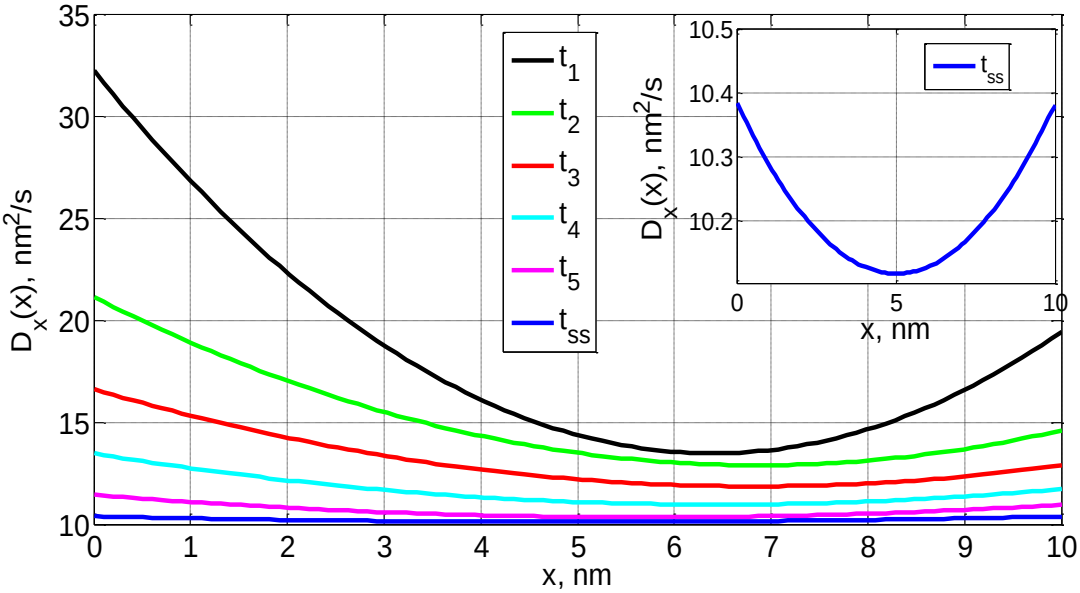

Figure 5.40. Temporal and one-dimensional spatial evolution of diffusivities for the one-particle open system of oxygen diffusion through the tin anode as the system relaxes from an initial transient state to steady state. Here, $y = z = 1.5$ nm.

Figure 5.41 shows three-dimensional plots of the transient diffusivities at the initial state, i.e., at t_1 and at an intermediate state, i.e., at t_2. As seen, the highest values occur at the inlet surface, while the lowest occurs at the center and the bottom of the box. This is confirmed by the

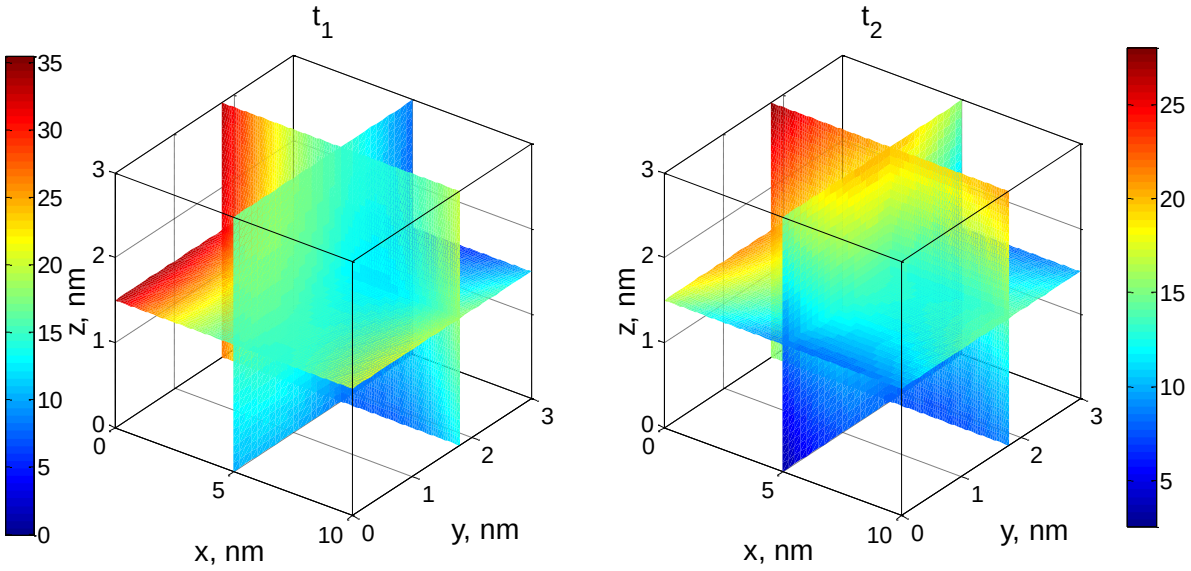

Figure 5.41. Three-dimensional plot of diffusivities for oxygen diffusion through the tin anode at the initial transient state, i.e., at t_1 and an intermediate transient state, i.e., at t_2.

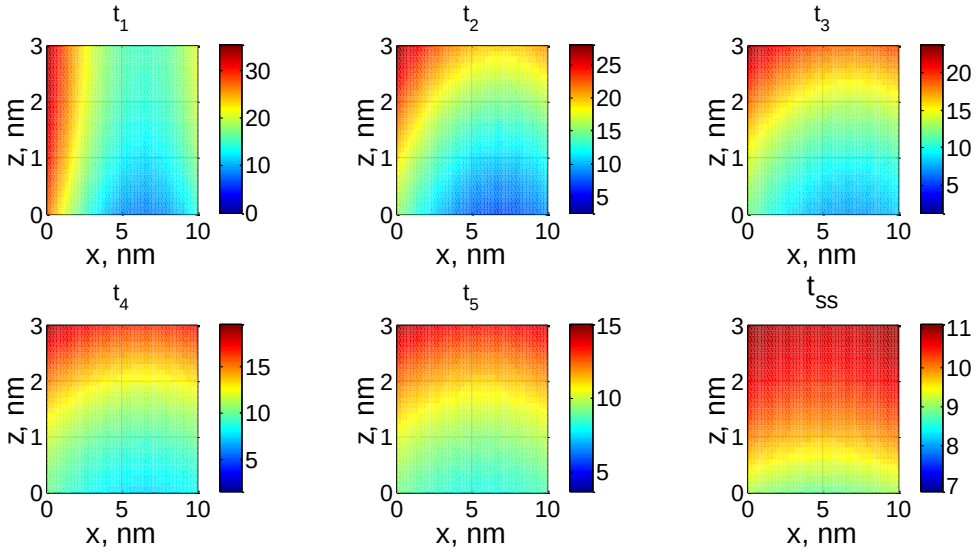

Figure 5.42. Temporal and two-dimensional spatial evolution of diffusivities for oxygen diffusion through the tin anode as the state of the open system evolves in time from its initial transient state at t_1 to steady state at t_{ss}. Here, $y = 1.5$ nm.

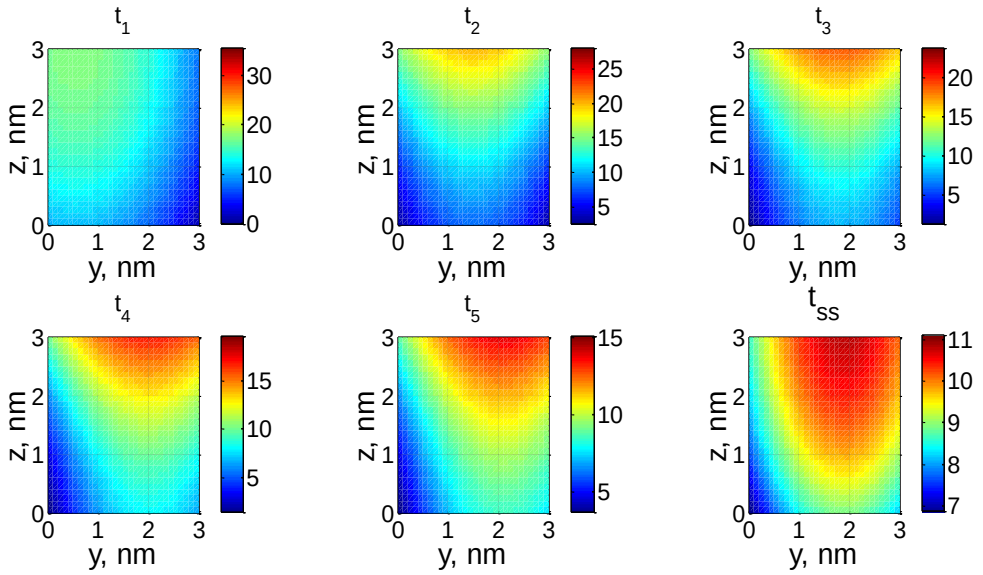

Figure 5.43. Temporal and two-dimensional spatial evolution of diffusivities for oxygen diffusion through the tin anode as the state of the open system evolves in time from its initial transient state at t_1 to steady state at t_{ss}. Here, $x = 5$ nm.

two-dimensional contour given in Figure 5.42 and 5.43 for the x-z and y-z planes at t_1. When the system relaxes to another intermediate transient state, i.e., at t_2, the transient diffusivity shows different behavior (see Figure 5.41). The highest values occur at the top of the inlet surface and at the top of the box, while the lowest values occur at the center and bottom of the box as shown in Figure 5.42 and 5.43 and for the x-z and y-z planes at t_2. Also, intermediate values are seen in these figures at the outlet surface of the box.

Figure 5.44 shows that the behavior of the diffusivity changes again when the system relaxes to other intermediate transient states, i.e., those at t_3 and t_4. As seen in this figure, the diffusivity has its highest values at the top of the box and intermediate values in the center of the box in the x direction. This is confirmed in Figure 5.42 for the x-z plane. The lowest values occur at the bottom of the box and close to the surface where $y = 0$. Again, this is confirmed in Figure 5.43 for the y-z plane as well in the two-dimensional contours of Figure 5.45 for the x-y plane. Figure 5.46 shows the behavior of the diffusivity for the intermediate transient state at t_5 as well as for the steady state at t_{ss}. As seen, both the transient and steady state diffusivities have their highest values at the top of the box and intermediate values at the bottom of the box in the x direction.

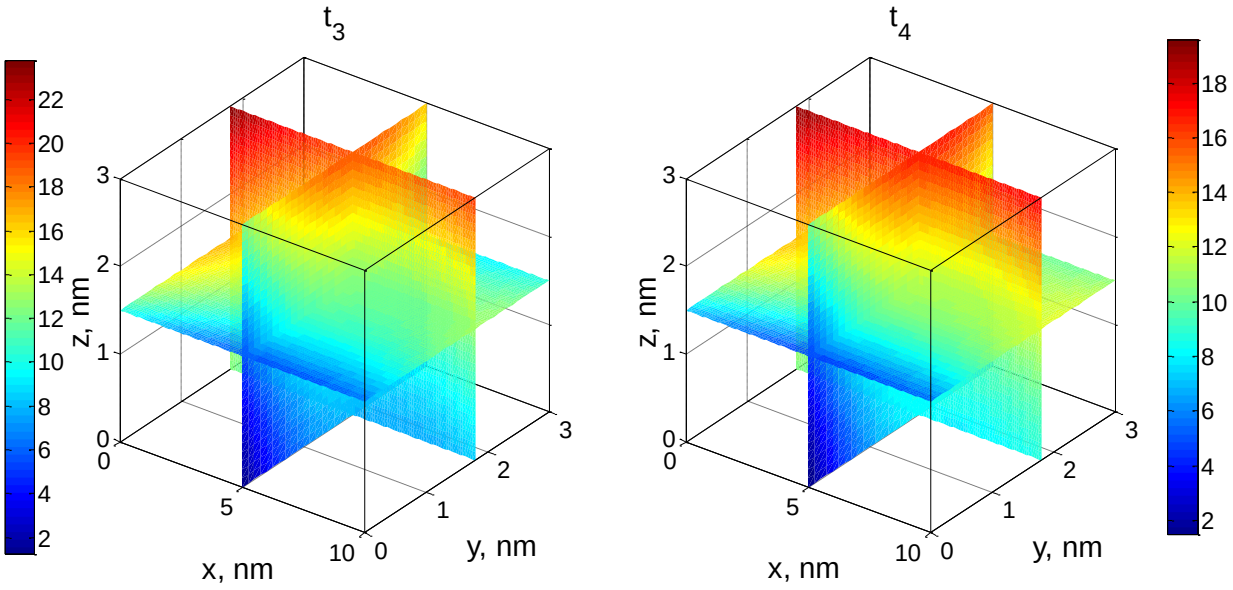

Figure 5.44. Three-dimensional plot of diffusivities for oxygen diffusion through the tin anode at the intermediate transient states, i.e., t_3 and t_4.

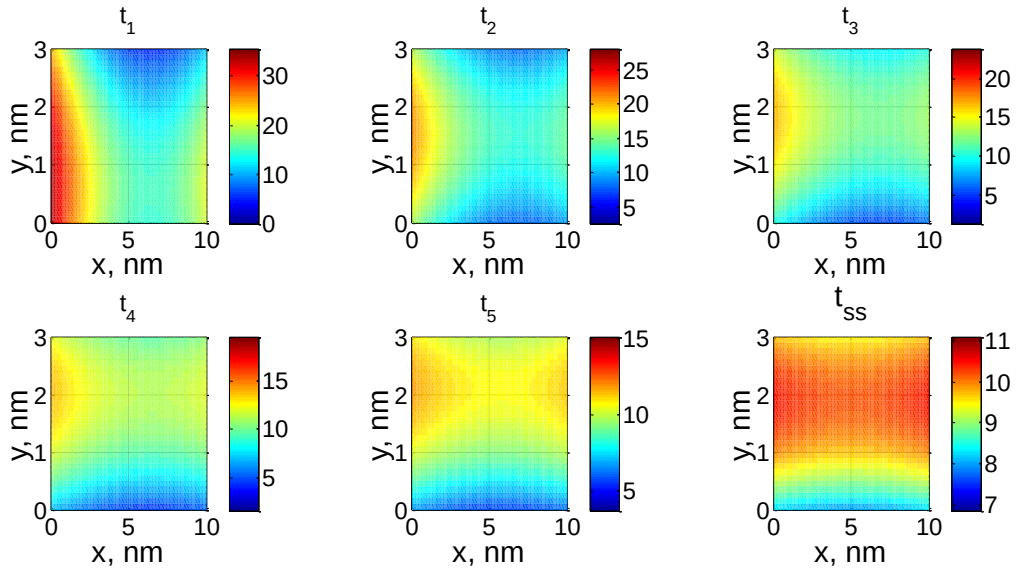

Figure 5.45. Temporal and two-dimensional spatial evolution of diffusivities for oxygen diffusion through the tin anode as the state of the open system evolves in time from its initial transient state at t_0 to steady state at t_{ss}. Here, $z = 1.5$ nm.

This is confirmed in Figure 5.42 for the x-z plane at t_5 and t_{ss}. Note that the steady state diffusivity has a symmetric distribution in the x direction as seen in this figure. Also, as shown in Figure **5.43**, both the transient and steady state diffusivities have their lowest values at the bottom of the surface at $y = 0$ and their highest values at the top and center of the box.

Finally, whether in 1D, 2D, or 3D, it is clear as shown by the results above that predicted diffusivity values are very different throughout the transient and steady state regimes. Thus, predicting them on the basis of the equilibrium distributions typically used in the literature for what is inherently a non-equilibrium process is problematic to say the least. As has been demonstrated here with this research these limitations can indeed be overcome.

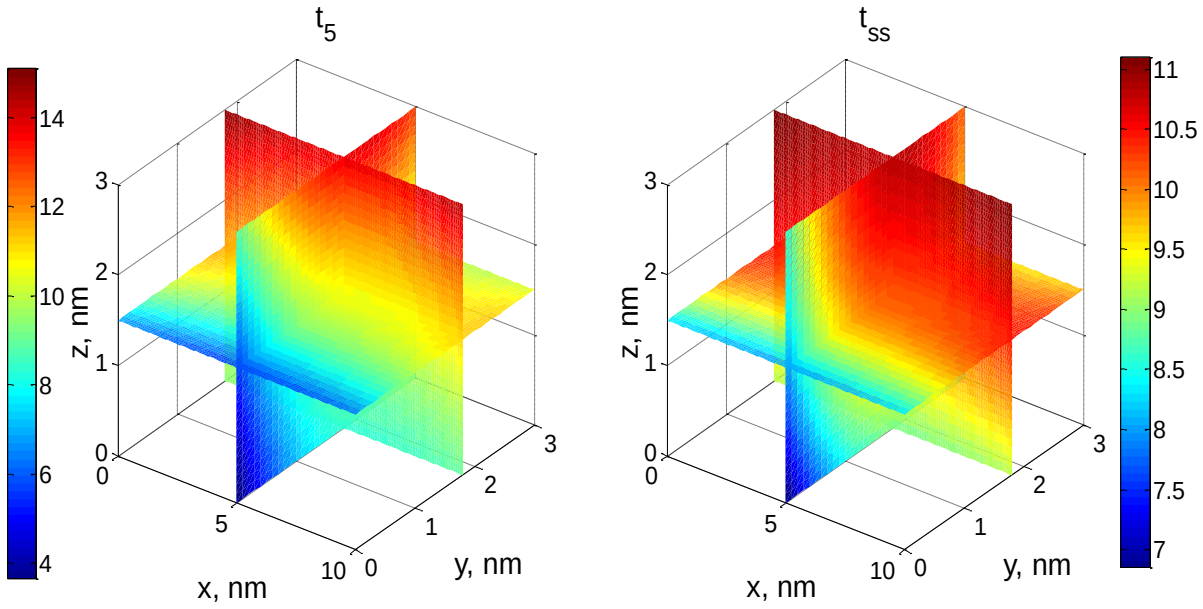

Figure 5.46. Three-dimensional plot of diffusivities for oxygen diffusion through the tin anode at the intermediate transient state at t_5 and at steady state, i.e., at t_{ss}.

Chapter 6 - Conclusions and Recommendations

In this doctoral research, the SEAQT framework is applied to atomistic-level systems in the region of not stable equilibrium states to demonstrate the effectiveness of this non-equilibrium approach for modeling and describing the diffusion of both closed and open systems. The development of non-equilibrium-based models for predicting both the density distributions and diffusivities of these systems has successfully been completed and implemented for both types of systems. For the former, prediction of the non-equilibrium thermodynamic path that the state of an *isolated system*, consisting of He^3 and He^4, takes is used to determine the density distributions and diffusivities of He^3 and He^4 at and far from equilibrium. The difference in behavior of fermions (He^3) and bosons (He^4) is captured and compared successfully to that of the equilibrium-based approach found in literature. In contrast, the open system predictions for density distribution and diffusivity have no counterpart in the literature and are, thus, completely original to this research and provide, absent any equilibrium assumptions, an original model for the transient thermodynamic path that such a small-scale system would undergo. The effects, thus, of both the transient and steady-state behavior of the open system on the density distributions and diffusivities for oxygen diffusion through a tin anode are captured.

Finally, all of the original contributions outlined in *Chapter* 1 have been achieved in this research as have all the tasks needed to realize these contributions. However, much additional work is needed. With this in mind recommendations for future work include the following:

- Extend the work presented in *Chapter* 3 for modeling quantum ideal gases to modeling the condensed behavior of boson and fermion superfluids.
- Extend the non-equilibrium model for diffusion for both closed and open systems to many particles using the density of state method developed by Li and von Spakovsky [117, 118] and Al-Abbasi, Beretta and von Spakovsky [66, 67].
- Develop a c-code based on the PETSc® software instead of MATLAB® to determine the stiffness and mass matrices for the finite element analysis used in solving the large-scale eigenvalue problem.

- Extract thermodynamic property information for non-equilibrium states for both closed and open systems using either a surrogate system approach [119, 120] or the hypo-equilibrium state approach proposed by Li and von Spakovsky [117, 118].
- Suggest possible experiments whose results could be used to validate the diffusivities developed in the SEAQT framework.

References

1. Combs, R.J., *Gaseous diffusion in liquids*. 1986, Virginia Tech.
2. Jacobs, M.H., *Diffusion processes*. 1967: Springer.
3. Jost, W., *Diffusion in solids, liquids, gases*. 1960, New York: Academic Press.
4. Glicksman, M.E., *Diffusion in solids*. 2000: Wiley.
5. Tosun, I., *Modelling in transport phenomena : a conceptual approach*. 2002, Amsterdam; Boston: Elsevier.
6. Thomson, W.J., *Introduction to transport phenomena*. 2000, Upper Saddle River, NJ: Prentice Hall.
7. Tien, C.L.M.A.G.F.M., *Microscale energy transport*. 1998, Washington, D.C.: Taylor & Francis.
8. Brenig, W., *Statistical theory of heat : nonequilibrium phenomena*. 1989, Berlin; New York: Springer-Verlag.
9. Tien, C.L.L.J.H., *Statistical thermodynamics*. 1971, New York: Holt, Rinehart, and Winston.
10. Heer, C.V., *Statistical mechanics, kinetic theory, and stochastic processes*. 1972, New York: Academic Press.
11. Stowe, K.S., *An introduction to thermodynamics and statistical mechanics*. 2007, Cambridge, UK; New York: Cambridge University Press.
12. Pathria, R.K.B.P.D., *Statistical mechanics*. 2011, Amsterdam; Boston: Elsevier/Academic Press.
13. Chen, G., *Nanoscale energy transport and conversion : a parallel treatment of electrons, molecules, phonons, and photons*. 2005, Oxford; New York: Oxford University Press.
14. Ozturk, Z.F., A. Sisman, and C. Firat, *Quantum Effects on Gas Diffusion at the Nano Scale*. International Journal of Thermodynamics, 2011. **14**(4).
15. Hatsopoulos, G.N. and J.H. Keenan, *Principles of general thermodynamics*. Vol. 398. 1965: Wiley New York.
16. Hatsopoulos, G. and E. Gyftopoulos, *A unified quantum theory of mechanics and thermodynamics. Part I. Postulates.* Foundations of Physics, 1976. **6**(1): p. 15-31.
17. Hatsopoulos, G. and E. Gyftopoulos, *A unified quantum theory of mechanics and thermodynamics. Part IIa. Available energy.* Foundations of Physics, 1976. **6**(2): p. 127-141.
18. Hatsopoulos, G. and E. Gyftopoulos, *A unified quantum theory of mechanics and thermodynamics. Part IIb. Stable equilibrium states.* Foundations of Physics, 1976. **6**(4): p. 439-455.
19. Hatsopoulos, G. and E. Gyftopoulos, *A unified quantum theory of mechanics and thermodynamics. Part III. Irreducible quantal dispersions.* Foundations of Physics, 1976. **6**(5): p. 561-570.
20. Beretta, G.P., *On the general equation of motion of quantum thermodynamics and the distinction between quantal and nonquantal uncertainties*. 1981: MIT.
21. Beretta, G.-P., *Maximal-entropy-production-rate nonlinear quantum dynamics compatible with second law, reciprocity, fluctuation-dissipation, and time-energy uncertainty relations.* arXiv preprint quant-ph/0112046, 2001.

22. Smith, C.E. and M.R. von Spakovsky. *Comparison of the non-equilibrium predictions of Intrinsic Quantum Thermodynamics at the atomistic level with experimental evidence*. in *Journal of Physics: Conference Series*. 2012. IOP Publishing.
23. Shankar, R., *Principles of quantum mechanics*. 1994, New York: Plenum Press.
24. Messiah, A., *Quantum mechanics*. 1961, Amsterdam; New York: North-Holland Pub. Co. ; Interscience Publishers.
25. Hagelstein, P.L.S.S.D.O.T.P., *Introductory applied quantum and statistical mechanics*. 2004, Hoboken, N.J.: Wiley-Interscience.
26. Phillips, A.C., *Introduction to quantum mechanics*. 2003, Chichester; New York: Wiley.
27. Bethe, H.A.J.R.W., *Intermediate quantum mechanics*. 1986, Menlo Park, Calif.: Benjamin/Cummings Pub. Co.
28. Griffiths, D.J., *Introduction To Quantum Mechanics, 2/E*. 2005: Pearson Education India.
29. McMahon, D., *Quantum Mechanics Demystified 2/E*. 2013: McGraw-Hill Professional Pub.
30. Dirac, P.A.M., *The principles of quantum mechanics*. 1930.
31. McMahon, D., *Quantum computing explained*. 2007: John Wiley & Sons.
32. Schwabl, F., *Statistical mechanics*. 2002, Berlin; New York: Springer.
33. Le Bellac, M.M.F.B.G.G., *Equilibrium and non-equilibrium statistical thermodynamics*. 2004, Cambridge, UK; New York: Cambridge University Press.
34. Schieve, W.C.H.L.P., *Quantum statistical mechanics*. 2009, Cambridge, UK; New York: Cambridge University Press.
35. Hatsopoulos, G.N. and E.P. Gyftopoulos, *Thermionic energy conversion. Volume II. Theory, technology, and application*. 1979.
36. Von Neumann, J., *Mathematical foundations of quantum mechanics*. 1996, Princeton, N.J.: Princeton University Press.
37. von Spakovsky, M.R., *The Second Law: A Unified Approach to Thermodynamics Applicable to All Systems and All States.* AIP Conference Proceedings, 2008. **1033**(1): p. 302-308.
38. Beretta, G.P., *Steepest-Entropy-Ascent Irreversible Relaxation Towards Thermodynamic Equilibrium: The Dynamical Ansatz that Completes the Gyftopoulos-Hatsopoulos Unified Theory with a General Quantal Law of Causal Evolution.* International Journal of Thermodynamics, 2006. **9**(3): p. 117-128.
39. Beretta, G.P., *Nonlinear model dynamics for closed-system, constrained, maximal-entropy-generation relaxation by energy redistribution.* Physical Review E, 2006. **73**(2): p. 026113.
40. Beretta, G.P., *Modeling non-equilibrium dynamics of a discrete probability distribution: General rate equation for maximal entropy generation in a maximum-entropy landscape with time-dependent constraints.* Entropy, 2008. **10**(3): p. 160-182.
41. Beretta, G.P. *Maximum entropy production rate in quantum thermodynamics*. in *Journal of Physics: Conference Series*. 2010. IOP Publishing.
42. Carey, V.P., *Statistical thermodynamics and microscale thermophysics*. 1999, Cambridge, UK; New York: Cambridge University Press.
43. von Spakovsky, M.R. and J. Gemmer, *Some Trends in Quantum Thermodynamics.* Entropy, 2014. **16**(6): p. 3434-3470.
44. von Spakovsky, M.R. *The Second Law: A Unified Approach to Thermodynamics Applicable to All Systems and All States*. in *MEETING THE ENTROPY CHALLENGE:*

An International Thermodynamics Symposium in Honor and Memory of Professor Joseph H. Keenan. 2008. AIP Publishing.
45. Von Neumann, J. and R.T. Beyer, *Mathematical foundations of quantum mechanics*. 1996, Princeton, N.J.: Princeton University Press.
46. Gyftopoulos, E.P. *Building on the Legacy of Professor Keenan. Entropy An Intrinsic Property of Matter*. in *MEETING THE ENTROPY CHALLENGE: An International Thermodynamics Symposium in Honor and Memory of Professor Joseph H. Keenan*. 2008. AIP Publishing.
47. Park, J.L., *Nature of Quantum States.* American Journal of Physics, 1968. **36**(3): p. 211-226.
48. Beretta, G.P., E.P. Gyftopoulos, and J.L. Park, *Quantum thermodynamics. A new equation of motion for a general quantum system*. Il Nuovo Cimento B Series 11, 1985. **87**(1): p. 77-97.
49. Beretta, G.P., *Nonlinear quantum evolution equations to model irreversible adiabatic relaxation with maximal entropy production and other nonunitary processes.* Reports on Mathematical Physics, 2009. **64**(1): p. 139-168.
50. Laurendeau, N.M., *Statistical thermodynamics: fundamentals and applications*. 2005: Cambridge University Press.
51. Firat, C., A. Sisman, and Z. Ozturk, *Effects of Particle-Wall Interactions on the Thermodynamic Behavior of Gases at the Nano Scale.* International Journal of Thermodynamics, 2011. **14**(4): p. 155.
52. Sisman, A. and I. Muller, *The Casimir-like size effects in ideal gases.* Physics Letters A, 2004. **320**(5–6): p. 360-366.
53. Sisman, A., et al., *Thermodynamics Under Quantum Size Effects.* Gen, 2006. **39**: p. 2563-2571.
54. Sisman, A., Z.F. Ozturk, and C. Firat, *Quantum boundary layer: a non-uniform density distribution of an ideal gas in thermodynamic equilibrium*. Physics Letters A, 2007. **362**(1): p. 16-20.
55. Ozturk, Z.F., A. Sisman, and C. Firat, *Quantum effects on gas diffusion at the nano scale.* International Journal of Thermodynamics, 2011. **14**(4): p. 163.
56. Ozturk, Z. and A. Sisman, *Quantum size effects on the thermal and potential conductivities of ideal gases.* Physica Scripta, 2009. **80**(6): p. 065402.
57. Smith, C.E., *Intrinsic Quantum Thermodynamics: Application to hydrogen storage on a carbon nanotube and theoretical consideration of non-work interactions*. 2012, Virginia Tech.
58. von Spakovsky, M.R., C.E. Smith, and V. Verda. *Quantum Thermodynamics for the Modeling of Hydrogen Storage on a Carbon Nanotube*. in *ASME 2008 International Mechanical Engineering Congress and Exposition*. 2008. American Society of Mechanical Engineers.
59. Sciacovelli, A., et al., *Quantum Thermodynamics: Non-equilibrium 3D Description of an Unbounded System at an Atomistic Level.* International Journal of Thermodynamics, 2010. **13**(1): p. 23-33.
60. Cano-Andrade, S., G.P. Beretta, and M.R. von Spakovsky. *Non-Equilibrium Thermodynamic Modeling of an Atom-Field State Evolution with Comparisons to Published Experimental Data*. in *Proceedings of the 12th Joint European Thermodynamics Conference, Brescia, Italy*. 2013.

61. Cano-Andrade, S., *Thermodynamic Based Framework for Determining Sustainable Electric Infrastructures as well as Modeling of Decoherence in Quantum Composite Systems*. 2014.
62. Cano-Andrade, S., G.P. Beretta, and M.R. von Spakovsky, *Steepest-entropy-ascent quantum thermodynamic modeling of decoherence in two different microscopic composite systems*. Physical Review A, 2015. **91**(1): p. 013848.
63. Brune, M., et al., *Observing the progressive decoherence of the "meter" in a quantum measurement*. Physical Review Letters, 1996. **77**(24): p. 4887.
64. Cano-Andrade, S., M.R. von Spakovsky, and G.P. Beretta. *Steepest-Entropy-Ascent Quantum Thermodynamic Non-equilibrium Modeling of Decoherence of a Composite System of Two Interacting Spin-½ Systems*. in *ASME 2013 International Mechanical Engineering Congress and Exposition*. 2013. American Society of Mechanical Engineers.
65. Beretta, G.P. and M. von Spakovsky, *Steepest-entropy-ascent quantum thermodynamic framework for describing the non-equilibrium behavior of a chemically reactive system at an atomistic level*. arXiv preprint arXiv:1504.03994, 2015.
66. Al-Abbasi, O.A., *Modeling the Non-Equilibrium Behavior of Chemically Reactive Atomistic Level Systems Using Steepest-Entropy-Ascent Quantum Thermodynamics*. 2013.
67. Al-Abbasi, O., G.P. Beretta, and M.R. von Spakovsky. *Intrinsic Quantum Thermodynamic Prediction of the Non-equilibrium Atomistic-Level Behavior of Chemically Reactive Systems*. in *Proceedings of the 12th Joint European Thermodynamics Conference, Brescia, Italy*. 2013.
68. Babac, G., A. Sisman, and Z.F. Ozturk. *QUANTUM SIZE AND DEGENERACY EFFECTS ON THERMAL SELF-DIFFUSION UNDER FREE MOLECULAR TRANSPORT REGIME*. in *Proceedings of the 12th Joint European Thermodynamics Conference, Brescia, Italy*. 2013.
69. Swendsen, R.H., *An introduction to statistical mechanics and thermodynamics*. 2012, Oxford: Oxford University Press.
70. Li, G., O. Al-Abbasi, and M.R. von Spakovsky. *Atomistic-level non-equilibrium model for chemically reactive systems based on steepest-entropy-ascent quantum thermodynamics*. in *Journal of Physics: Conference Series*. 2014. IOP Publishing.
71. Beretta, G.P., *Quantum thermodynamics of nonequilibrium. Onsager reciprocity and dispersion-dissipation relations*. Foundations of physics, 1987. **17**(4): p. 365-381.
72. Stowe, K.S., *Introduction to statistical mechanics and thermodynamics*. 1984, New York: Wiley.
73. Gander, W. and W. Gautschi, *Adaptive quadrature—revisited*. BIT Numerical Mathematics, 2000. **40**(1): p. 84-101.
74. Fornberg, B. and J. Zuev, *The Runge phenomenon and spatially variable shape parameters in RBF interpolation*. Computers & Mathematics with Applications, 2007. **54**(3): p. 379-398.
75. Boyd, J.P., *Six strategies for defeating the Runge Phenomenon in Gaussian radial basis functions on a finite interval*. Computers & Mathematics with Applications, 2010. **60**(12): p. 3108-3122.
76. Quarteroni, A. and F. Saleri, *Approximation of functions and data*. 2006: Springer.
77. Epperson, J.F., *On the Runge example*. Amer. Math. Monthly, 1987. **94**(4): p. 329-341.
78. Balay, S., et al., *PETSc Users Manual Revision 3.5*. 2014.

79. Campos, C., et al., *SLEPc users manual.* D. Sistemes Informatics i Computació, Universitat Politecnica de Valencia, Tech. Rep. DSIC-II/24/02-Revision, 2012. **3**.
80. Hernandez, V., J.E. Roman, and V. Vidal, *SLEPc: A scalable and flexible toolkit for the solution of eigenvalue problems.* ACM Transactions on Mathematical Software (TOMS), 2005. **31**(3): p. 351-362.
81. Hernández, V., J.E. Román, and V. Vidal, *SLEPc: Scalable library for eigenvalue problem computations*, in *High Performance Computing for Computational Science—VECPAR 2002*. 2003, Springer. p. 377-391.
82. Lennard-Jones, J. and A. Devonshire, *Critical phenomena in gases. I.* Proceedings of the Royal Society of London. Series A, Mathematical and Physical Sciences, 1937: p. 53-70.
83. Prigogine, I., *The molecular theory of solutions*. 1957, Amsterdam; New York: North-Holland Pub. Co.; Interscience Publishers.
84. Hill, T.L., *An introduction to statistical thermodynamics*. 2012: Courier Corporation.
85. McQuarrie, D.A., *Statistical thermodynamics*. 1973, New York: Harper & Row.
86. Sonntag, R.E. and G.J. Van Wylen, *Introduction to thermodynamics : classical and statistical*. 1991, New York: J. Wiley.
87. Wasserman, A.L., *Thermal physics : concepts and practice*. 2012, Cambridge, UK; New York: Cambridge University Press.
88. Reddy, J.N., *An introduction to the finite element method*. Vol. 2. 1993: McGraw-Hill New York.
89. Ottosen, N.S., H. Petersson, and N. Saabye, *Introduction to the finite element method*. 1992: Prentice Hall Internationa.
90. Kwon, Y.W. and H. Bang, *The finite element method using MATLAB*. 2000: CRC press.
91. Liu, G.R. and S.S. Quek, *Finite element method : a practical course*. 2003, Oxford: Butterworth-Heinemann.
92. Thompson, E.G., *Introduction to the Finite Element Method: Theory, Programming and Applications*. 2004: Wiley Text Books.
93. Munejiri, S., et al. *Structure of Liquid Tin under High Pressure by ab initio molecular-dynamics simulation*. in *Journal of Physics: Conference Series*. 2008. IOP Publishing.
94. Calderín, L., et al., *Structural, dynamic, and electronic properties of liquid tin: An ab initio molecular dynamics study.* The Journal of Chemical Physics, 2008. **129**(19): p. 194506.
95. Tsuji, K., et al., *Pressure dependence of the structure of liquid group 14 elements.* Journal of Physics: Condensed Matter, 2004. **16**(14): p. S989.
96. Ravelo, R. and M. Baskes, *Equilibrium and Thermodynamic Properties of Grey, White, and Liquid Tin.* Physical Review Letters, 1997. **79**(13): p. 2482-2485.
97. Furukawa, K., et al., *The structure of liquid tin.* Philosophical Magazine, 1963. **8**(85): p. 141-155.
98. El-Ashram, T., *Structure and properties of rapidly solidified pure tin.* Radiation Effects & Defects in Solids, 2006. **161**(3): p. 193-197.
99. Kariya, Y., et al., *Tin pest in Sn-0.5 wt.% Cu lead-free solder.* JOM, 2001. **53**(6): p. 39-41.
100. Latini, G., R. Cocci Grifoni, and G. Passerini, *Transport properties of organic liquids*. 2006, Southampton; Boston: WIT Press.
101. Barker, J.A., *Lattice theories of the liquid state*. Vol. 1. 1963: Pergamon Press.

102. Nagata, I., *KIHARA POTENTIAL AND LENNARD-JONES AND DEVONSHIRE EQUATION OF STATE OF LIQUIDS AND DENSE GASES.* Canadian Journal of Chemistry, 1966. **44**(22): p. 2651-2656.
103. Magee, J.E. and N.B. Wilding, *The Lennard-Jones-Devonshire cell model revisited.* Molecular Physics, 2002. **100**(10): p. 1641-1644.
104. Hill, T.L., *Statistical mechanics: principles and selected applications*. 2013: Courier Corporation.
105. Terrell, L., *Hill, An introduction to statistical thermodynamics*. 1960, Addison-Wesley.
106. Reed, T.M. and K.E. Gubbins, *Applied statistical mechanics.* 1973.
107. Dyson, P., et al., *Fluid properties at nano/meso scale: a numerical treatment*. Vol. 1. 2008: John Wiley & Sons.
108. Hirschfelder, J.O., et al., *Molecular theory of gases and liquids*. 1965, [New York]: Wiley.
109. Bird, R.B., W.E. Stewart, and E.N. Lightfoot, *Transport phenomena*. 2007: John Wiley & Sons.
110. Berghe, G.V. and H. De Meyer, *A finite-element estimate with trigonometric hat functions for Sturm–Liouville eigenvalues.* Journal of computational and applied mathematics, 1994. **53**(3): p. 389-396.
111. Andrew, A.L., *Correction of finite element eigenvalues for problems with natural or periodic boundary conditions.* BIT Numerical Mathematics, 1988. **28**(2): p. 254-269.
112. Evans, D. *Numerical solution of the Sturm Liouville problem with periodic boundary conditions*. in *Conference on Applications of Numerical Analysis*. 1971. Springer.
113. De Schepper, H., *A finite element method for differential eigenvalue problems with mixed classical and (semi-) periodic boundary conditions.* Applied mathematics and computation, 2001. **121**(1): p. 1-15.
114. Geuzaine, C. and J.F. Remacle, *Gmsh: A 3-D finite element mesh generator with built-in pre-and post-processing facilities.* International Journal for Numerical Methods in Engineering, 2009. **79**(11): p. 1309-1331.
115. Sharma, G. and J. Martin, *MATLAB®: a language for parallel computing.* International Journal of Parallel Programming, 2009. **37**(1): p. 3-36.
116. Anderson, J.D. and J. Wendt, *Computational fluid dynamics*. Vol. 206. 1995: Springer.
117. Li, G., *A Steepest-Entropy-Ascent Quantum Thermodynamic Framework for the Multi-scale, Multi-physics Modeling of Non-equilibrium Phenomena in Reactive and Non-reactive Systems*, in *M.E. Dept*. 2015, Virginia Tech.
118. Li, G. and M.R. von Spakovsky, *Steepest-entropy-ascent quantum thermodynamic modeling of relaxation process of isolated chemical reactive meso-/macroscopic system using density of states and hypo-equilibrium state.* 2015.
119. Gyftopoulos, E.P. and G.P. Beretta, *Thermodynamics - Foundations and Applications*. 2005, New York: Dover.
120. Beretta, G.P. and E.P. Gyftopoulos, *Thermodynamic derivations of conditions for chemical equilibrium and of Onsager reciprocal relations for chemical reactors.* The Journal of Chemical Physics, 2004. **121**(6): p. 2718-2728.